Searches with the ATLAS Detector for New Coloured Particles in the Jets + $E_{\mathrm{T}}^{\mathrm{miss}}$ Channel in Early LHC Data

Christopher J. S. Young

Magdalen College, Oxford University

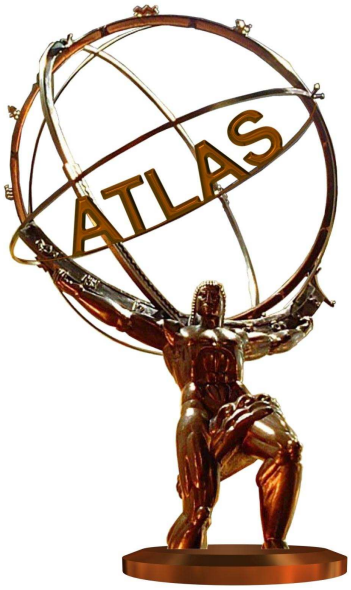

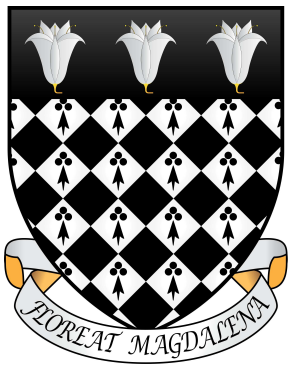

Contents

Acknowledgements

I would like to acknowledge several people for their help and advice during the course of my D.Phil. Firstly, my supervisor Alan Barr who has helped and guided me and was also a co-editor of the primary analysis presented here. I would also like to thank Anna Sfyrla, the third co-editor of the analysis, and the rest of the analysis team.

The Oxford ATLAS group has been a pleasure to work in and I would like to thank the group in general for the useful help and advice given at the weekly meetings.

I would also like to mention the many friends that I have made during the period of my D.Phil both in Oxford and at CERN. In particular I would like to mention those that lived in the Rue de L'Athenee accommodation who have also been a great help in answering many questions.

Finally, I would like to thank CERN for the successful operation of the LHC, the Worldwide LHC Computing Grid, the STFC and the rest of the ATLAS Collaboration without whom this work would not have been possible.

Working Within a Collaboration and Publications

The work presented within this thesis was completed by myself as part of the ATLAS collaboration. Other people also worked on the main analysis presented in §7 and it is made clear which parts of the analysis were done by myself and others. Additionally, obviously, I am indebted to the people who built the detector and those who provide the centralised calibrations and recommendations of the different physics objects.

The analysis detailed in §7 has been published as an ATLAS conference note [1] and previous versions of the analysis where the techniques I pioneered were first introduced have been published as papers; the first implementation using $1.34\,\text{fb}^{-1}$ of 7 TeV data in [2] and using $4.7\,\text{fb}^{-1}$ of 7 TeV data in [3].

Furthermore, early on in my D.Phil I contributed to the lower jet multiplicity searches without leptons, providing the multi-jet background estimation for the 2010 analysis [4] and the systematic uncertainty due to the increased number of interactions per bunch crossing and frequency of bunch crossings for the initial 2011 analyses [5, 6]. These analyses are not presented in full within this thesis as they have been superseeded by new results and I contributed significantly more to the analyses on high jet multiplicities and $E_{\text{T}}^{\text{miss}}$ which I went on to work on.

I have taken shifts operating the detector during the period of my D.Phil both as a "Run Control" shifter in the control room and as a Jet/$E_{\text{T}}^{\text{miss}}$ trigger expert on-call. My work in the $E_{\text{T}}^{\text{miss}}$ trigger detailed in §4.6.1 along with these shifts qualified me as a member of the ATLAS collaboration author list.

Within the collaboration I have been a member of two "Editorial Boards", a group of people responsible for reviewing an analysis and taking it though the collaboration approval procedure.

Additionally in the first year of my D.Phil as an introduction to searches for supersymmetry I looked into various kinematic variables that can be used in such searches. These studies resulted in a paper commenting on one such variable upon which I am a co-author [7].

Chapter 1

Introduction

The switching on of the Large Hadron Collider (LHC) in March 2010 and its successful operation thereafter has opened doors in the search for new physics beyond the Standard Model. The primary aims of the two general purpose experiments, ATLAS [8] and CMS [9], are two fold; firstly to investigate the mechanism of electroweak symmetry breaking in the Standard Model by determining the validity of the Higgs mechanism, and secondly to discover any new physics and/or particles that exist near the electro-weak scale as is predicted by many beyond the Standard Model (BSM) theories. This thesis documents my contributions to the second of these objectives in the context of searching for a particular BSM theory: R-parity conserving Supersymmetry (SUSY) [10] using the data of the ATLAS collaboration in channels requiring missing transverse momentum ($E_{\mathrm{T}}^{\mathrm{miss}}$), hadronic jets and no high p_{T} electrons or muons.

Supersymmetry introduces a new symmetry to the Standard Model which results in the prediction that every Standard Model particle should have a supersymmetric partner with the same quantum numbers but differing in spin by a half. The introduction of this symmetry solves one of the major problems with the Standard Model, the Hierarchy Problem, detailed in §2.1. As we do not observe superpartners degenerate with their Standard Model partners, the symmetry is necessarily broken such that the Standard Model and supersymmetric partners differ in mass. The minimal supersymmetric partners are listed along with their Standard Model counterparts in Table 1.1.

In the general supersymmetric Lagrangian there exist terms which allow protons to decay. Experimental limits on proton decay are very strict both from experiment [11, 12] and the age

of the universe. The solution to this problem used in the models contained within this thesis is to introduce R-parity which removes these terms and renders the lightest supersymmetric particle stable. If the supersymmetric partners of the coloured Standard Model particles have masses $\lesssim$1 TeV then they will be copiously produced at the LHC. In R-parity conserving theories they will be produced in pairs and then each decay to some number of Standard Model particles and one (or very rarely some other odd number) lightest supersymmetric particle (LSP) which is stable. Experimental constraints put very strong limits on the LSP both being electromagnetically neutral [13, 14, 15, 16] and un-coloured [15, 17]. The LSPs produced will therefore pass through the detector undetected and will contribute to the $E_{\mathrm{T}}^{\mathrm{miss}}$.

In 1933 Fritz Zwicky first suggested that a large proportion of the matter in the universe may be *"dunkle Materie"* (Dark Matter) [18] – matter that does not emit light – due to his observations of the velocity dispersion of galaxies in the Coma cluster. Since then a large amount of astrophysical data has accumulated to support this theory starting in the 1970s when rotation curves of individual galaxies showed evidence for additional matter [19, 20, 21]. More recently other sources of evidence have appeared: weak [22] and strong [23] gravitational lensing, X-ray measurements of hot gas in clusters [24], the famous "Bullet Cluster" [25], big bang neucleosynthesis [26], constraints from observations of large scale structure [27], velocity measurements of distant supernova [28, 29] and the precise measurement of the cosmic microwave background (CMB) by the WMAP Collaboration [30]. Therefore it is now widely accepted that some form of non-luminous material inhabits our universe on all scales and it interacts gravitationally but not strongly or electromagnetically. From measurements the energy densities of the three primary types of matter in the modern universe (baryonic (B), dark matter (DM) and dark energy (Λ)[1]) are found to be [30]:

$$\begin{aligned} \Omega_B &\simeq 0.0456 \pm 0.0016 \\ \Omega_{DM} &\simeq 0.227 \pm 0.014 \\ \Omega_\Lambda &\simeq 0.728 \pm 0.015\,. \end{aligned}$$

[1]The nature of dark energy is also not understood at the time of writing and is another of the major mysteries in astrophysics, however, supersymmetry does not attempt to provide a candidate for dark energy so it is not discussed further.

R-parity conserving Supersymmetry models provide a candidate for this dark matter as the lightest Supersymmetric particle is stable and is usually the lightest neutralino[2].

The discovery of R-parity conserving Supersymmetry at the LHC with a LSP consistent with dark matter would be a major discovery and would link fundamental physics at very short scales to that observed on the largest scales possible. This motivates searching for R-parity conserving supersymmetry in channels involving $E_{\mathrm{T}}^{\mathrm{miss}}$.

The structure of the thesis is as follows. Firstly, the theoretical motivation for low energy (TeV-scale) Supersymmetry is given in §2. There exist constraints on the models that could be realised in nature from both previous colliders, low energy observables and astrophysics. These are briefly discussed in §3. The ATLAS detector is described in §4 with particular reference to the $E_{\mathrm{T}}^{\mathrm{miss}}$ trigger with which I was closely involved during the period of my D.Phil. (§4.6.1). The simulation of both signal models and Standard Model backgrounds is described in §5. Fully hadronic searches for Supersymmetry with the ATLAS detector other than the one described in detail, the 8 TeV search requiring high multiplicity, are overviewed in §6 before the main analysis is presented in §7. Finally, the conclusions of the search are presented along with an outlook to the future in §8.

[2]In this thesis other dark matter candidates are not considered. The only other SUSY particles in minimal theories that can be considered are gravitinos, which are reasonable candidates in some theories, and sneutrinos which are disfavoured due to their large direct detection cross-section although in models where there are both right and left handed neutrinos sneutrinos can be viable LSPs [31, 32]

Family	**Standard Model Particle**			**Supersymmetric Partner**		
	Name	**Symbol**	**Spin**	**Name**	**Symbol**	**Spin**
Leptons, Sleptons	electron	e^-	$\frac{1}{2}$	selectron	$\tilde{e}^-$	0
	muon	μ^-	$\frac{1}{2}$	smuon	$\tilde{\mu}^-$	0
	tau	τ^-	$\frac{1}{2}$	stau	$\tilde{\tau}^-$	0
	electron-neutrino	ν_e	$\frac{1}{2}$	electron-sneutrino	$\tilde{\nu}_e$	0
	muon-neutrino	ν_μ	$\frac{1}{2}$	muon-sneutrino	$\tilde{\nu}_\mu$	0
	tau-neutrino	ν_τ	$\frac{1}{2}$	tau-sneutrino	$\tilde{\nu}_\tau$	0
Quarks, Squarks	up	u	$\frac{1}{2}$	sup	$\tilde{u}$	0
	down	d	$\frac{1}{2}$	sdown	$\tilde{d}$	0
	charm	c	$\frac{1}{2}$	scharm	$\tilde{c}$	0
	strange	s	$\frac{1}{2}$	sstrange	$\tilde{s}$	0
	top	t	$\frac{1}{2}$	stop	$\tilde{t}$	0
	bottom	b	$\frac{1}{2}$	sbottom	$\tilde{b}$	0
Gluon, Gluinos	gluon	g	1	gluino	$\tilde{g}$	$\frac{1}{2}$
Gauge Bosons,	W-boson	W^+, W^0, W^-	1	winos	$\tilde{W}^+, \tilde{W}^0, \tilde{W}^-$	$\frac{1}{2}$
Gauginos	B-boson	B^0	1	bino	$\tilde{B}^0$	$\frac{1}{2}$
Higgs, Higgsino sector	Higgs	H_u^+, H_u^0 H_d^0, H_d^-	0	higgsinos	$\tilde{H}_u^+, \tilde{H}_u^0$ $\tilde{H}_d^0, \tilde{H}_d^-$	$\frac{1}{2}$

Table 1.1: The MSSM particle spectrum. It should be noted that this is the spectrum before mixing of the different states. For example in the Standard Model there is mixing between the different neutrino eigenstates and after electroweak symmetry breaking the W^0 and B^0 states mix to form the photon (γ) and Z-boson (Z^0). Similar effects occur in the Supersymmetric sector depending on the nature of the breaking of the Supersymmetry, for example the winos, bino and higgsinos will mix to form four neutral fermions named the neutralinos ($\tilde{\chi}_1^0, \tilde{\chi}_2^0, \tilde{\chi}_3^0, \tilde{\chi}_4^0$) and two charged fermions denoted charginos ($\tilde{\chi}_1^\pm, \tilde{\chi}_2^\pm$). More details on the mixing between the different Supersymmetric states is given in §2.2.2

Chapter 2

The Theoretical Motivation

To motivate the analyses that are presented later on, first a digression is taken into the underlying theory behind both the Standard Model (SM) of particle physics and the theory of Supersymmetry (SUSY) that is probed by these searches.

The SM of particle physics is the primary basis of our current knowledge of the microscopic universe[1]. An overview of the basic mathematical formulation is given in §2.1. In particular, in §2.1 the Higgs mechanism of electroweak Symmetry Breaking is detailed as an example of how elegant theories of broken symmetries are. Also, in §2.1, one of the main theoretical problems of the SM is detailed: the "Hierarchy problem", which is alleviated by the addition of the extra symmetry to form a supersymmetric theory.

Having demonstrated the problem associated with the loop corrections to the Higgs mass in the SM we turn to the theory of supersymmetry in §2.2. By introducing a symmetry between fermionic and bosonic states this problem is removed however, the lack of observation of partner particles predicted by this additional symmetry at the same masses as their SM counterparts means that this must be a broken symmetry. Details of the breaking mechanism are unknown (although several possibilities have been put forward). In the theories studied in this thesis R-Parity is assumed to be a conserved quantity at low scales and is described and experimentally motivated in §2.2.3. The conditions under which the supersymmetric theory continues to solve the Hierarchy problem, which was the original motivation given here, are then shown in §2.2.4.

[1]Although gravity and general relativity are not incorporated into the Standard Model it is still the most successful single theory in describing experimental results.

An example of a SUSY breaking mechanism is described in §2.2.5 and an alternative approach of simplified models or the use of low scale parameters is detailed in §2.2.6.

The arguments presented are then briefly summarised in §2.3.

2.1 Introducing the Standard Model

The Standard Model Lagrangian

The Standard Model of particles physics is a Quantum Field Theory. The Lagrangian of the Standard Model ($\mathcal{L}_{\mathrm{SM}}$) describes the particle content and interactions of the model and is an embodiment of the symmetry group $SU(3)$ x $SU(2)$ x $U(1)$. It consists of three components; the $SU(3)$ coloured sector ($\mathcal{L}_{\mathrm{QCD}}$), the $SU(2)$ x $U(1)$ generator of the W and B gauge fields ($\mathcal{L}_{\mathrm{EW}}$) and the Higgs sector ($\mathcal{L}_{\mathrm{Higgs}}$). Equations 2.1-2.3 give the mathematical formulation of the first two components before electroweak symmetry breaking.

$$\mathcal{L}_{\mathrm{SM}} = \mathcal{L}_{\mathrm{QCD}} + \mathcal{L}_{\mathrm{EW}} + \mathcal{L}_{\mathrm{Higgs}} \tag{2.1}$$

$$\mathcal{L}_{\mathrm{QCD}} = i\bar{U}(\partial_\mu - ig_s G^a_\mu T^a)\gamma^\mu U + i\bar{D}(\partial_\mu - ig_s G^a_\mu T^a)\gamma^\mu D - \frac{1}{4}G^a_{\mu\nu}G^{\mu\nu}_a \tag{2.2}$$

$$\mathcal{L}_{\mathrm{EW}} = \sum_\psi \bar{\psi}\gamma^\mu \left(i\partial_\mu - g' Y_W B_\mu - g\tau_{L_a} W^a_\mu\right)\psi - \frac{1}{4}B_{\mu\nu}B^{\mu\nu} - \frac{1}{4}W^a_{\mu\nu}W^{\mu\nu}_a \tag{2.3}$$

- U and D are the Dirac spinors associated with the three generations of up-type and down-type quarks respectively.
- G^a_μ is the $SU(3)$ gauge field of the strong force containing the octet of gluons, $G^a_{\mu\nu}$ is the field strength tensor of this field and T^a are the generators of the group.
- g_s is the strong force coupling constant and γ^μ are the Dirac matrices.
- ψ are the Dirac spinors for both the quark and lepton fermion fields.
- Y_W is the weak hypercharge and is the generator of the $U(1)$ gauge group.[2]

[2]Note that here we define $Y_W = Q - T_3$ where Q is the electric charge and T_3 is the third component of weak isospin. In some sources this is defined differently, usually $Y_W = 2(Q - T_3)$ but here the notation of [33] is followed.

Name	Weak Interaction Spinor	Electric Charge	Weak hypercharge
Left handed quark fields	$Q_L^{(1)} = \begin{pmatrix} u \\ d \end{pmatrix}_L \; ; \; Q_L^{(2)} = \begin{pmatrix} c \\ s \end{pmatrix}_L \; ; \; Q_L^{(3)} = \begin{pmatrix} t \\ b \end{pmatrix}_L$	$\begin{pmatrix} \frac{+2}{3} \\ \frac{-1}{3} \end{pmatrix}$	$\begin{pmatrix} \frac{+1}{6} \\ \frac{+1}{6} \end{pmatrix}$
Right handed quark fields	$q_R^{(1)} = \begin{pmatrix} u \\ d \end{pmatrix}_R \; ; \; q_R^{(2)} = \begin{pmatrix} c \\ s \end{pmatrix}_R \; ; \; q_R^{(3)} = \begin{pmatrix} t \\ b \end{pmatrix}_R$	$\begin{pmatrix} \frac{+2}{3} \\ \frac{-1}{3} \end{pmatrix}$	$\begin{pmatrix} \frac{+2}{3} \\ \frac{-1}{3} \end{pmatrix}$
Left handed lepton fields	$L_L^{(1)} = \begin{pmatrix} \nu_e \\ e^- \end{pmatrix}_L \; ; \; L_L^{(2)} = \begin{pmatrix} \nu_\mu \\ \mu^- \end{pmatrix}_L \; ; \; L_L^{(3)} = \begin{pmatrix} \nu_\tau \\ \tau^- \end{pmatrix}_L$	$\begin{pmatrix} 0 \\ -1 \end{pmatrix}$	$\begin{pmatrix} \frac{-1}{2} \\ \frac{-1}{2} \end{pmatrix}$
Right handed lepton fields	$e_R^{(1)} = (e^-)_R \; ; \; e_R^{(2)} = (\mu^-)_R \; ; \; e_R^{(3)} = (\tau^-)_R$	-1	-1

Table 2.1: The fermion content of the Standard Model where there exist three generations of both right and left handed quarks and leptons. Right handed neutrinos are not present in the Standard Model so are not included.

- τ_{L_a} are the Pauli matrices divided by a factor 2 and are the generators of the $SU(2)$ group. The sub-script L denotes that the field only act on left handed fermions.[3]

- $B_\mu\,(B_{\mu\nu})$ and $W_\mu^a\,(W_{\mu\nu}^a)$ are the B and W gauge fields (field strength tensors) and their coupling constants are given by g' and g respectively.

$\mathcal{L}_{QCD} + \mathcal{L}_{EW}$ forms the Standard Model Lagrangian before the introduction of the Higgs field and electroweak symmetry breaking. Notice that there are many problems as the theory stands; there are no mass terms for any of the fermions, the vector boson fields are also all massless and the B and W^3 fields have not been mixed to form the photon and Z^0. The fermion mass terms cannot simply be included as the introduction of mass terms like $-m_f(\bar{f}_L f_R + \bar{f}_R f_L)$ is forbidden as this breaks the global gauge invariance (the left and right hand fields belong to different $SU(2)$ representations and have different charges under $U(1)$). The addition of mass terms for the vector bosons is also forbidden by gauge invariance. However, after the spontaneous breaking of the Higgs sector both the fermions and the vector bosons can acquire masses. This breaking is covered in the following section. However, the fermion particle content is all present and is summarised in Table 2.1.

[3]From experiment it is known that the W bosons only couple to left-handed fields and this choice of chiral gauge also has the effect that the divergent one-loop triangle diagrams coupling vector bosons to each other cancel as required.

Electroweak Symmetry Breaking

An important feature of the Standard Model is the Higgs mechanism of electroweak symmetry breaking. This has important physical consequences; it directly gives masses to the weak force bosons and allows the addition of fermion mass terms to the Lagrangian without breaking global gauge invariance. In the Standard Model the Higgs field, ϕ, is a spinor representation of $SU(2)$ which is charged with weak hypercharge $Y_W = +1/2$. The gauge transformation of the field ϕ then becomes

$$\phi \rightarrow e^{i\alpha^a \tau^a} e^{i\beta/2} \phi \,.$$

The covariant derivative of ϕ is therefore given by

$$D_\mu \phi = \left(\partial_\mu - igW_\mu^a \tau^a - i\frac{1}{2} g' B_\mu \right) \phi \,.$$

We add this field into the Lagrangian in the most general way by adding a kinetic term, a mass term of the new field and a self-interaction term with a coupling strength, λ. This gives the following terms in the Higgs Lagrangian:

$$\mathcal{L}_{\text{Higgs}} = (D_\mu \phi)^2 + \mu^2 \phi^\dagger \phi - \lambda (\phi^\dagger \phi)^2 \,. \tag{2.4}$$

We assume that the Higgs field picks up a vacuum expectation value v and then parametrise the field such that it has a real-valued lower component consisting of the vacuum expectation value and an additional fluctuating real-valued field $h(x)$ with $<h(x)> = 0$. This spinor is acted on by a $SU(2)$ gauge transformation $U(x)$ to retain the most general complex two-component spinor,

$$\phi(x) = U(x) \frac{1}{\sqrt{2}} \begin{pmatrix} 0 \\ \\ v + h(x) \end{pmatrix} \,.$$

Placing this into Equation 2.4 and then minimising the potential gives an expression for the Higgs vacuum expectation in terms of μ and λ:

$$v = \left(\frac{\mu^2}{\lambda} \right)^{1/2} \,.$$

The expansion of Equation 2.4 using the definition of the covariant derivative has other important implications. Firstly there appear terms that have no dependence on W^a_μ or B_μ:

$$\mathcal{L}_h = \frac{1}{2}(\partial_\mu h)^2 - \mu^2 h^2 - \lambda v h^3 - \frac{1}{4}\lambda h^4 \,.$$

These represent a kinetic term, a mass term ($m_h = \sqrt{2}\mu = \sqrt{2\lambda}v$) and 3- and 4-point interaction terms of a new physical state – the Higgs boson. The prediction of this physical state is one of the key aspects of the theory such that the search for the Higgs boson has been central to the efforts of the experimental community for many years. Recently evidence of a new bosonic resonance consistent with the Standard Model Higgs boson has been published by both the ATLAS [34] and CMS [35] collaborations and much effort will go into measuring the properties of this new particle to see if it is indeed the Standard Model Higgs boson.

Now we turn to the additional terms which arise from the expansion of Equation 2.4 which have no dependence on h. Explicitly evaluating the matrix product using the Pauli matrices yields:

$$\mathcal{L}_V = \frac{1}{2}\frac{v^2}{4}\left[g^2(W^1_\mu)^2 + g^2(W^2_\mu)^2 + (-gW^3_\mu + g'B_\mu)^2\right] \,.$$

These terms are recognised as mass terms of the vector bosons. A simple re-definition of the fields can then be used to acquire three massive vector bosons and a fourth field, orthogonal to the other neutral field, which remains massless:

$$W^\pm_\mu = \frac{1}{\sqrt{2}}(W^1_\mu \mp iW^2_\mu) \quad \text{with mass} \quad m_W = g\frac{v}{2} \tag{2.5}$$

$$Z^0_\mu = \frac{1}{\sqrt{g^2+g'^2}}(gW^3_\mu - g'B_\mu) \quad \text{with mass} \quad m_Z = \sqrt{g^2+g'^2}\frac{v}{2} \tag{2.6}$$

$$A^0_\mu = \frac{1}{\sqrt{g^2+g'^2}}(g'W^3_\mu + gB_\mu) \quad \text{with mass} \quad m_A = 0\,.$$

Finally in the expansion there are terms which couple the Higgs boson to the massive vector bosons. Using the newly defined physical massive vector boson fields these terms can be written:

$$\mathcal{L}_{VVh,VVhh} = \left[m^2_W W^{\mu+}W^-_\mu + \frac{1}{2}m^2_Z Z^\mu Z_\mu\right].\left(\frac{2h}{v} + \frac{h^2}{v^2}\right) \,.$$

There is therefore coupling between the Standard Model Higgs and the massive vector bosons as well as 4-point couplings between two Higgs bosons and the massive vector bosons.

Lastly, we turn to the problem of the fermion masses. Amazingly this can also be solved by this same field. Interaction terms between ϕ and the fermions can be introduced without breaking gauge invariance and when ϕ obtains a vacuum expectation value, mass terms for the fermions appear. For example to generate a mass for the electron we can introduce a coupling:

$$\Delta\mathcal{L}_e = -\lambda_e \bar{E}_L.\phi e_R + (\text{hermitian conjugate})\,.$$

When ϕ aquires its vacuum expectation value a term in the Lagrangian appears which gives the electron its mass:

$$\Delta\mathcal{L}_e = \frac{-1}{\sqrt{2}}\lambda_e v \bar{e}_L e_R + (\text{hermitian conjugate}) + \ldots\,.$$

Therefore the electron mass is then given by $m_e = \lambda_e v/\sqrt{2}$. Note that although the Higgs mechanism allows the fermions to acquire masses it does not explain why they are the particular values that are observed, or indeed why they are so different from each other. Similarly for the quarks coupling terms can be added to the Lagrangian which give rise to quark mass terms;

$$\begin{aligned}\Delta\mathcal{L}_q &= \lambda_d \bar{Q}_L.\phi d_R - \lambda_u \epsilon^{ab}\bar{Q}_{L_a}\phi_b^\dagger u_R + (\text{hermitian conjugate}) \\ &= \frac{-1}{\sqrt{2}}\lambda_d v \bar{d}_L d_R - \frac{1}{\sqrt{2}}\lambda_u v \bar{u}_L u_R + (\text{hermitian conjugate}) + \ldots\,,\end{aligned}$$

such that the masses of the u and d quarks ($m_u = \lambda_u v/\sqrt{2}\,;\, m_d = \lambda_d v/\sqrt{2}$) are also given in terms of arbitrary renormalizable couplings. When all three generations of quarks are considered diagonal terms between the generations can be introduced. To obtain the physical mass states, a rotation is required to diagonalise the mass matrix. A consequence of this rotation is that while the $W^\pm$ fields only couple to particles within each generation in the original basis, in the new basis there are couplings between generations. This is the origin of the flavour mixing matrix known as the Cabibbo-Kobayashi-Maskawa (CKM) matrix which gives the coupling

strengths of the different quark pairs under the $W^{\pm}$ field.[4]

The vacuum expectation value of the Higgs field can be determined by experiment. The lifetime of the muon has been very accurately measured [36] and this decay proceeds through a virtual W boson. Due to ratio m_{μ}/m_W being small an effective Lagrangian can be used with a coupling of $G_F/\sqrt{2}$, where:

$$\frac{G_F}{\sqrt{2}} = \frac{g^2}{8m_W^2} = \frac{1}{2v^2}\,.$$

G_F is known precisely from the muon lifetime measurement such that within the Standard Model the vacuum expectation value, v, is known to be 246 GeV. Furthermore, at LEP a large number of precision measurements were carried out which have weak dependence on the Higgs boson mass. By combining various measurements at the Z pole [37], the width of the W resonance [38] and the hadronic contribution to the running of the electromagnetic coupling constant [39] into a global fit it was possible to predict the Higgs mass using these data. An example of a fit by the Gfitter group [40] is shown in Figure 2.1. Furthermore the masses of the top quark [41] and W boson [42] have been measured accurately at the Tevatron and these depend strongly on the Higgs sector through virtual corrections (as is discussed in the following section). Therefore, these can also be used to indirectly constrain the Higgs boson mass (again see Figure 2.1). Finally, ATLAS and CMS observed a significant excess in their search for the Standard Model Higgs boson in the Summer of 2012 [34, 35]. Assuming this is the Standard Model Higgs boson then this can be used to over-constrain the fit and test the model. This was also carried out in [40] and good agreement between all the considered observables was observed.

The Hierarchy Problem

One of the primary concerns with the Standard Model is the "Hierarchy Problem" which arises when loop diagrams are considered. The arguments here are those concerning orders of magnitude so from now on calculations are given with this accuracy. The Standard Model is assumed to be an accurate theory up to some scale Λ. It is a fully re-normalisable theory such

[4]It should also be noted that in this formalism there are no mass terms for the neutrinos. To accomplish this it would have been necessary to add ν_R fermions that are not part of the Standard Model.

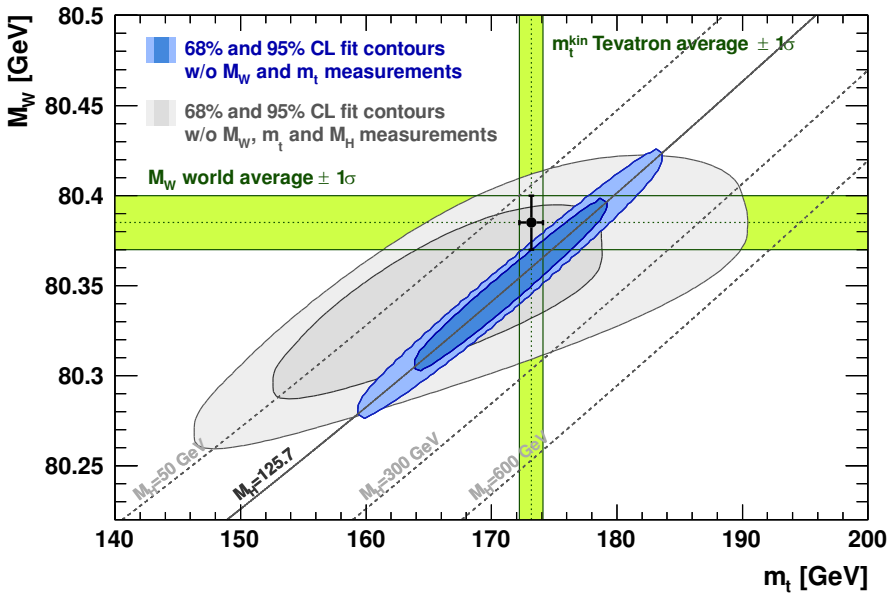

Figure 2.1: A fit to the electroweak precision data of the Standard Model excluding the direct measurement of the top quark and W boson masses is given in gray. The same fit but also assuming that the new particle observed at the LHC in Summer 2012 is the Standard Model Higgs boson is given in blue. The two fits are seen to be compatible. The observed masses of the top quark and W boson are shown as yellow bands. These intersect the fit to the other measurements showing that there is no significant tension between the electroweak precision data's prediction of the Higgs boson, W boson and top quark masses and the observed values. Furthermore given the measurement of the (assumed) Higgs boson mass there is no tension with the observed top quark and W boson masses. Figure taken from [40].

that in isolation this scale can be taken to ∞ however, we know that it should break down at least when quantum gravity becomes important at the so-called Planck scale $M_P \sim 10^{19}\,\text{GeV}$.

The first loop diagram we consider is the self-coupling loop of the Higgs boson shown in Figure 2.3(a). We integrate this loop diagram up to the cut-off scale Λ such that an additional mass term appears:

$$\Delta m_h^2 \phi^\dagger \phi \propto \lambda_{hhhh} \int^\Lambda d^4k \frac{1}{k^2 - m_h^2} \phi^\dagger \phi \sim \lambda_{hhhh} \Lambda^2 \phi^\dagger \phi \,, \tag{2.7}$$

where λ_{hhhh} is the Higgs self-coupling constant. Additional sub-leading terms which are at most dependent on $\ln \Lambda$ have been omitted. As Λ is assumed to be large (eg. $\sim M_P$) this is a huge correction to the Higgs boson mass. This is not a problem if the Standard Model is treated in isolation as Λ can be taken to ∞ and then μ^2 which determines the tree-level mass can be chosen such that as $\Lambda \to \infty$ the (renormalised) coefficient of the scalar mass term $\phi^\dagger \phi$ has the desired value.[5] However, we know that the Standard Model is not valid beyond M_P and also μ determines the tree level masses of the W and Z bosons by Equations 2.5-2.6 so μ is also expected to be $\sim 100\,\text{GeV}$ and cannot be chosen arbitrarily.

Furthermore, the Higgs boson will also recieve corrections to its mass from loops involving the other Standard Model particles that it couples to. The largest of these comes from the top quark (due to its large mass). The loop diagram for the top quark contribution is given in Figure 2.3(b). This correction has a similar form but picks up a negative sign due to the closed fermion loop:

$$\Delta m_h^2 \phi^\dagger \phi \propto -\lambda_{t\bar{t}h}^2 \left(\int^\Lambda \frac{d^4k}{\not{k}\not{k}} \right) \phi^\dagger \phi \sim -\lambda_{t\bar{t}h}^2 \Lambda^2 \phi^\dagger \phi \,. \tag{2.8}$$

The Higgs boson therefore receives positive quadratic corrections from vector boson loops and its self interaction and negative quadratic corrections from all the fermions on top of its tree level mass of $\sqrt{2}\mu$. These corrections are proportional to the cut-off scale which is assumed to be very large.[6] This means that the Higgs boson mass which is constrained by electroweak precision measurements to be near the electroweak scale ($\sim 100\,\text{GeV}$) relies on the cancellation

[5] This is the normal renormalisation procedure for massive terms.

[6] There are theories which put the Planck scale near the electroweak scale, for example, due to the presence of large extra dimensions. Searches at the LHC probing the Standard Model at the highest possible energy scales so far found no evidence for the Standard Model breaking down near the electroweak scale (eg. [43]).

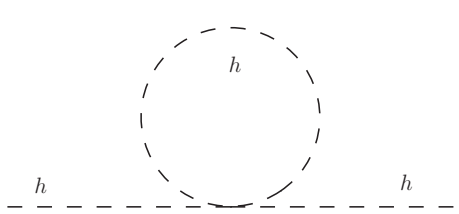

(a) The loop correction to the Higgs boson mass from the Higgs self-interaction.

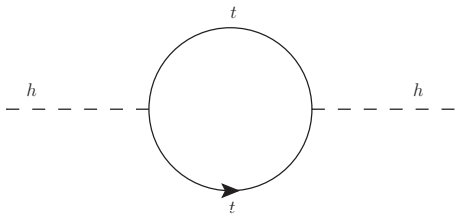

(b) The loop correction from the top quark to the Higgs boson mass

Figure 2.2: Examples of loop corrections to the Higgs boson mass which quadratically diverge leading to the Hierarchy problem.

of terms relating the masses of the fermions and vector bosons to the Higgs 4-point interaction to a precision of 1 part in 10^{34} assuming that the Standard Model is valid up to $\Lambda = M_P$. This extremely precise cancellation between different input parameters to the model appears highly un-natural and is considered one of the serious failings of the Standard Model. As we will see supersymmetry solves this problem through the symmetry between the Standard Model particles and their superpartners.

2.2 Introducing Supersymmetry

2.2.1 Introducing a new Symmetry (solving the Hierarchy Problem)

Supersymmetry introduces a new symmetry to the Standard Model between bosonic and fermionic states. We introduce an operator Q that generates transformations between these states.

$$Q|\text{Boson}> = |\text{Fermion}> \quad ; \quad Q|\text{Fermion}> = |\text{Boson}> \, .$$

To generate a symmetry such as this the set of operators, Q_α must be anticommuting spinors and their hermitian conjugates, $Q^\dagger_{\dot{\alpha}}$, are also symmetry generators. From the Haag-Lopuszanski-Sohnuius theorem [44][45] in a theory of chiral fermions such as in the Standard Model the algebra of this operator is as follows:

$$\left\{Q_\alpha, Q^\dagger_{\dot{\alpha}}\right\} = 2\sigma^\mu_{\alpha\dot{\alpha}} P^\mu$$

$$\{Q_\alpha, Q_\beta\} = \left\{Q^\dagger_{\dot{\alpha}}, Q^\dagger_{\dot{\beta}}\right\} = 0$$

$$[Q_\alpha, P^\mu] = \left[Q^\dagger_{\dot{\alpha}}, P^\mu\right] = 0 \, ,$$

where P^μ is the generator of translations in spacetime. The particles are therefore arranged into *supermultiplets* which contain a set of states and their superpartners. Note that in general a large number of particles can live in each *supermultiplet*. The supersymmetic operators commute with the generators of the gauge transformations so all the particles in the same *supermultiplet* must lie in the same representation of the gauge group – they will have the same electric charges, weak isospins and will lie in the same colour representation. Also as the supersymmetric operators commute with P^μ the particles must all have the same mass. Finally by considering the operator $(-1)^{2s}$ (where s is the spin) acting on a state with a given four-momentum it can be shown that the number of bosonic and fermionic degrees of freedom in a *supermultiplet* must be equal.

Now returning to the loop corrections to the Higgs mass. In our unbroken supersymmetric theory each of the SM particles has been supplemented with appropriate superpartners to form

(a) The $\tilde{t}_L$ loop level contribution. (b) The $\tilde{t}_R$ loop level contribution.

Figure 2.3: The contributions to the Higgs mass at loop level from the superpartners to the top quark that cancel the quadratic divergence caused by the top quark itself.

supermultiplets. Consider the top quark loop from Figure 2.2(b) which provided a divergent contribution as seen in Equation 2.8. We now have an additional contribution from the partner particles. As the top has two degrees of freedom it is partnered with two scaler particles denoted $\tilde{t}_R$ and $\tilde{t}_L$. In the unbroken supersymmetric theory these will carry the same charges and have the same mass as the top particle. These particles will also contribute to the Higgs mass through loop diagrams as shown in Figure 2.3. As these are scalars they will provide positive quadratic divergences to the Higgs mass. Careful calculation of the contribution from scalars and fermions reveals that two additional scalars with the same masses and couplings precisely cancel out the fermion loop divergence. This is the case for all the quadratic divergences caused by the loop corrections from the SM particles. Therefore, in its unbroken form supersymmetry solves the hierarchy problem precisely by the definition of the symmetry. However, as we have not observed superpartners degenerate with their SM counterparts, supersymmetry must be a broken theory. In the following section we shall describe the softly broken Minimal Supersymmetric Standard Model which is the minimal extension to the SM to include supersymmetry.

2.2.2 The MSSM

The Minimal Supersymmetric Standard Model is usually formulated in terms of a *Superpotential*, W.[7] The full Lagrangian is given by the sum of the gauge invariant kinetic terms for all the particles and then the superpotential defining the interaction terms between the scalars and fermions:

$$\mathcal{L}_{\text{MSSM}} = \mathcal{L}_{\text{free}} - \frac{1}{2}\left(W^{ij}\psi_i\psi_j + W^*_{ij}\psi^{\dagger i}\psi^{\dagger j}\right) - W^i W^*_i + \mathcal{L}_{\text{bilinear}} + \mathcal{L}_{\text{D-term}}\,, \tag{2.9}$$

[7]For a full description of this notation see [46]

where W^i and W^{ij} are derivatives of the *Superpotential*, W, and are defined by:

$$W^i = \frac{\delta W}{\delta \phi_i} = M^{ij}\phi_j + \frac{1}{2}y^{ijk}\phi_j\phi_k \quad ; \quad W^{ij} = \frac{\delta^2}{\delta\phi_i\delta\phi_j}W\,. \tag{2.10}$$

The *Superpotential* itself is given by:

$$W_{\rm MSSM} = W_{\not R} + \bar{u}\mathbf{y_u}QH_u - \bar{d}\mathbf{y_d}QH_d - \bar{e}\mathbf{y_e}LH_d + \mu H_u H_d\,. \tag{2.11}$$

In writing this the fields $\bar{u}$, Q, $\bar{d}$, $\bar{e}$, L, H_u and H_d are taken to be all the scalar parts of the different chiral *supermultiplets* in the MSSM. The final two terms in Equation 2.9 arise when chiral and gauge fields are considered together and required to be invariant under gauge and supersymmetric transformations. The first of these includes terms which couple the fermion partners of the gauge fields to a scalar and its fermion partner with the same coupling (with a factor of $\sqrt{2}$) as the gauge field strength. The second of these gives the quartic scalar coupling again with a coupling defined by the gauge field strengths. For the origin of these terms see [46]. The R-Parity violating terms (see below) have not been written out explicitly but are included in $W_{\not R}$. There are several interesting points that are immediately obvious from these equations.

There are no mass terms for any of the particles. This is because all the particles acquire their masses through the same Higgs mechanism as detailed for the Standard Model in §2.1 or through the soft breaking terms.

The couplings are determined by the Yukawa matrices, $\mathbf{y_u}$, $\mathbf{y_d}$ and $\mathbf{y_e}$. These determine the couplings between a large number of different vertices. For example, if two of the incoming or outgoing particles are interchanged with their superpartners from any 3-point vertex with a Yukawa coupling then the new vertex has the same Yukawa coupling. Therefore the only new parameter above those in the SM required is μ.

The Extended Higgs Sector: It is clear from Equation 2.11 that the Higgs sector is different in the MSSM as it consists of two complex scalar doublets, H_u and H_d, as opposed to the single complex scalar doublet in the Standard Model. One reason for this extension can easily be seen

from the form of the *superpotential*. As the *superpotential* must be a holomorphic function, terms such as $H_d^* H_d$ and $\bar{u} Q H_d^*$ are forbidden. Therefore a single Higgs doublet is unable to provide masses, after the Higgs acquires a vacuum expectation value, to both up-type and down-type quarks.[8]

Breaking Supersymmetry: It is clear from the experimental evidence available to us that supersymmetry must be a broken symmetry as we have not observed superpartners degenerate with their SM particles. We have motivated that supersymmetry should be broken in such a way that the couplings do not change by large amounts and that the masses are not very large such that the Hierarchy problem does not return. We can therefore write down the SUSY breaking terms in the Lagrangian:

$$\begin{aligned}
\mathcal{L}_{\text{soft}} \;=\; & -\frac{1}{2}\left(M_3 \tilde{g}\tilde{g} + M_2 \tilde{W}\tilde{W} + M_1 \tilde{B}\tilde{B} + (\text{complex conjugate})\right) \\
& -\left(\tilde{\bar{u}}\mathbf{a_u}\tilde{Q}H_u - \tilde{\bar{d}}\mathbf{a_d}\tilde{Q}H_d - \tilde{\bar{e}}\mathbf{a_e}\tilde{L}H_d + (\text{complex conjugate})\right) \\
& -\tilde{Q}^\dagger \mathbf{m}^2_{\mathbf{Q}}\tilde{Q} - \tilde{L}^\dagger \mathbf{m}^2_{\mathbf{L}}\tilde{L} - \tilde{\bar{u}}\mathbf{m}^2_{\bar{\mathbf{u}}}\tilde{\bar{u}}^\dagger - \tilde{\bar{d}}\mathbf{m}^2_{\bar{\mathbf{d}}}\tilde{\bar{d}}^\dagger - \tilde{\bar{e}}\mathbf{m}^2_{\bar{\mathbf{e}}}\tilde{\bar{e}}^\dagger \\
& -m^2_{H_u} H_u^* H_u - m^2_{H_d} H_d^* H_d - (b H_u H_d + (\text{complex conjugate}))\,.
\end{aligned} \tag{2.12}$$

Here we have written down the most general gauge invariant, R-Parity conserving addition that can be made to the Lagrangian when we break supersymmetry. This makes no assumptions about how the symmetry was broken and therefore introduces a very large number of free parameters.

Higgs Mechanism in the MSSM: The Higgs mechanism in the MSSM follows the same principles as in the Standard Model which was given in detail in §2.1. Therefore it is only briefly summarised here primarily to show the structure of the other Higgs bosons.

The potential for the Higgs scalar fields in the MSSM after including the SUSY breaking

[8]Furthermore, the second Higgs doublet is required to ensure that the sum of the charges cancel such that there are no "triangle" gauge anomalies.

terms is:

$$\begin{aligned} V &= (|\mu|^2 + m_{H_u}^2)(|H_u^0|^2 + |H_u^+|^2) + (|\mu|^2 + m_{H_d}^2)(|H_d^0|^2 + |H_d^-|^2) \\ &+[b(H_u^+ H_d^- - H_u^0 H_d^0) + (\text{complex conjugate})] \\ &+\frac{1}{8}(g^2 + g'^2)(|H_u^0|^2 + |H_u^+|^2 - |H_d^0|^2 - |H_d^-|^2)^2 + \frac{1}{2}g^2|H_u^+ H_d^{0*} + H_u^0 H_d^{-*}|^2. \end{aligned} \tag{2.13}$$

Then H_u^+ is taken to be zero at the minimum of the potential which also implies that H_d^- must be zero at the minimum too. This means that the charged Higgs fields will not pick up vacuum expectation values. We take non-zero vacuum expectation values for the two neutral fields:

$$< H_u^0 >= v_u\,, \quad < H_d^0 >= v_d.$$

The Higgs fields have eight degrees of freedom of which three will be eaten as Nambu-Goldstone bosons and become the longitudinal modes of the Z^0 and $W^\pm$. There will therefore be five remaining Higgs mass eigenstates. Without loss of generality the gauge-eigenstates are expressed by:

$$\begin{pmatrix} H_u^0 \\ \\ H_d^0 \end{pmatrix} = \begin{pmatrix} v_u \\ \\ v_d \end{pmatrix} + \frac{1}{\sqrt{2}} R_\alpha \begin{pmatrix} h^0 \\ \\ H^0 \end{pmatrix} + \frac{1}{\sqrt{2}} R_{\beta_0} \begin{pmatrix} G^0 \\ \\ A^0 \end{pmatrix}$$

$$\begin{pmatrix} H_u^+ \\ \\ H_d^{-*} \end{pmatrix} = R_{\beta_\pm} \begin{pmatrix} G^+ \\ \\ H^+ \end{pmatrix}.$$

R_α, R_{β_0} and $R_{\beta_\pm}$ are orthogonal rotation matrices and are defined by:

$$\begin{aligned} R_\alpha &= \begin{pmatrix} \cos\alpha & \sin\alpha \\ \\ -\sin\alpha & \cos\alpha \end{pmatrix} \\ R_{\beta_0} &= \begin{pmatrix} \sin\beta_0 & \cos\beta_0 \\ \\ -\cos\beta_0 & \sin\beta_0 \end{pmatrix} \quad R_{\beta_\pm} = \begin{pmatrix} \sin\beta_\pm & \cos\beta_\pm \\ \\ -\cos\beta_\pm & \sin\beta_\pm \end{pmatrix}. \end{aligned}$$

To minimise the tree level potential we find:

$$\begin{aligned}
\beta &= \beta_0 = \beta_\pm \quad \text{with} \quad \tan\beta = \frac{v_u}{v_d} \\
m^2_{G^0} &= m^2_{G^\pm} = 0 \\
m^2_{A^0} &= \frac{2b}{\sin(2\beta)} = 2|\mu|^2 + m^2_{H_u} + m^2_{H_d} \\
m^2_{h^0,H^0} &= \frac{1}{2}\left(m^2_{A^0} + m^2_Z \mp \sqrt{(m^2_{A^0} - m^2_Z)^2 + 4m^2_Z m^2_{A^0}\sin^2(2\beta)}\right) \\
m^2_{H^\pm} &= m^2_{A^0} + m^2_W.
\end{aligned}$$

The five physical mass states are therefore h^0, H^0, $H^\pm$ and A^0. In the limit that m_{A^0} is large such that they decouple h^0 appears similar to the Standard Model Higgs boson with a tree level mass of $m_{h^0} \approx m_Z|\cos(2\beta)|$. However, this is subject to loop corrections that can be quite large and are described in §2.2.4.

Neutralino and Chargino Mixing: When the Higgs fields acquire their vacuum expectation values masses are given to the superpartners of the Higgs, W and B bosons. As there are also bi-linear terms in the MSSM Lagrangian which couple, for example, H^0_u, $\tilde{H}^0_u$ and $\tilde{B}^0$, a rotation in the basis of the superpartners is required to find the mass eigenstates which will be a mixture of the different gauge eigenstates. The four neutral gauge eigenstates; $\tilde{B}^0$, $\tilde{W}^0$, $\tilde{H}^0_d$ and $\tilde{H}^0_u$, we will get four mass eigenstates that traditionally are called neutralinos and are denoted in ascending mass order by $\tilde{\chi}^0_1$, $\tilde{\chi}^0_2$, $\tilde{\chi}^0_3$ and $\tilde{\chi}^0_4$. Similarly the charged gauge eigenstates $\tilde{W}^+$, $\tilde{H}^+_u$, $\tilde{W}^-$ and $\tilde{H}^-_d$ mix to form two (doubly-degenerate) mass eigenstates that are called charginos and are denoted in ascending mass order by $\tilde{\chi}^\pm_1$ and $\tilde{\chi}^\pm_2$. The two matrices which need to be diagonalised to find the masses of the gauginos are:

$$\mathbf{M}_{\tilde{N}} = \begin{pmatrix}
M_1 & 0 & -g'v_d/\sqrt{2} & g'v_u/\sqrt{2} \\
0 & M_2 & gv_d/\sqrt{2} & -gv_u/\sqrt{2} \\
-g'v_d/\sqrt{2} & gv_d/\sqrt{2} & 0 & -\mu \\
g'v_u/\sqrt{2} & -gv_u/\sqrt{2} & -\mu & 0
\end{pmatrix}$$

$$\mathbf{M}_{\tilde{C}} = \begin{pmatrix} \mathbf{0} & \mathbf{X}^T \\ \mathbf{X} & \mathbf{0} \end{pmatrix} \;\; ; \;\; \mathbf{X} = \begin{pmatrix} M_2 & gv_u \\ gv_d & \mu \end{pmatrix}.$$

Squark and Slepton Mixing: In Equation 2.12 there are terms that can lead to large flavour changing and CP-violating effects due to off-shell superpartners which mix the different squark or slepton generations. To avoid these constraints the supersymmetric breaking can be assumed to be flavour-blind such that:

$$\mathbf{m}^2_{\tilde{\mathbf{Q}}} = m^2_{\tilde{Q}}\mathbf{1} \; ; \; \mathbf{m}^2_{\tilde{\mathbf{u}}} = m^2_{\tilde{u}}\mathbf{1} \; ; \; \mathbf{m}^2_{\tilde{\mathbf{d}}} = m^2_{\tilde{d}}\mathbf{1} \; ; \; \mathbf{m}^2_{\tilde{\mathbf{L}}} = m^2_{\tilde{L}}\mathbf{1} \; ; \; \mathbf{m}^2_{\tilde{\mathbf{e}}} = m^2_{\tilde{e}}\mathbf{1}. \tag{2.14}$$

If these conditions are satisfied then the only flavour changing neutral currents will come from mixing induced by the trilinear couplings. These are often parametrised in terms of the Standard Model Yukawa matrices:

$$\mathbf{a_u} = \mathbf{A_u y_u} \; ; \; \mathbf{a_d} = \mathbf{A_d y_d} \; ; \; \mathbf{a_e} = \mathbf{A_e y_e}. \tag{2.15}$$

If the "A-terms" (trilinear couplings) are assumed to be proportional to the identity matrix then only the third generation has large couplings meaning that the flavour changing constraints that primarily involve the first two generations are avoided. Finally to avoid large CP-violating effects it is normal to assume that M_1, M_2, M_3 and the "A-terms" have no imaginary component. Together these conditions are known as *soft supersymmetry-breaking universality* and are often applied in model building. As only the third generation particles have large Yukawa couplings there will be little mixing between the first two generations. The mass eigenstates for the third generation will be a mixture of the left and right handed states, and are numbered 1 and 2 in ascending mass.[9]

[9]It should be noted that while the conditions of *soft supersymmetry-breaking universality* avoid experimental constraints and are motivated by some mediators they are not the only way to avoid these constraints. For example, if the masses of the first two generations of superpartners are very heavy then the flavour-changing and CP-violating processes are suppressed.

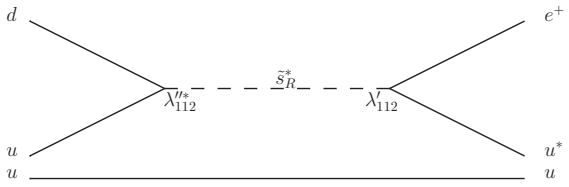

Figure 2.4: An example of proton decay facilitated by R-Parity violating operators. In the models considered in this thesis R-Parity is assumed to be conserved such that these processes are forbidden.

2.2.3 R-Parity

As mentioned in the introduction there are strong limits on the lifetime of the proton [11, 12]. There are several terms in the general MSSM Lagrangian which can lead to the rapid decay of the proton. More explicitly:

$$W_{\not R} = \frac{1}{2}\lambda^{ijk} L_i L_j \bar{e}_k + \lambda'^{ijk} L_i Q_j \bar{d}_k + \frac{1}{2}\lambda''^{ijk} \bar{u}_i \bar{d}_j \bar{d}_k + \mu'^i L_i H_u.$$

The first, second and fourth of these violate lepton number conservation, while the third violates baryon number conservation. These couplings all cannot be very large to agree with precision measurements [47]. Diagrams such as that shown in Figure 2.4 produce very strong limits on pairs of these couplings due to the long proton lifetime. The solution used in models within this thesis is to invoke a symmetry known as R-Parity or "matter parity". This assumes that the multiplicative quantum number defined by:

$$P_R = (-1)^{3(B-L)+2s}$$

is conserved, were B is the baryon number, L is the lepton number and s is the spin of the particle. This is found to be $+1$ for all SM particles and Higgs bosons, while their superpartners all have $P_R = -1$. Conservation of P_R ensures that the lightest supersymmetric particle is stable and that any produced supersymmetric particle will eventually decay to some number of SM particles and an odd number of lightest supersymmetric particles.

2.2.4 Maintaining Naturalness

The motivation given for TeV scale supersymmetry was the removal of the hierarchy problem. This was described in §2.2.1. As supersymmetry is a broken symmetry the cancellation between the corrections from the SM particles and the corrections introduced by their superpartners will not be complete. If the masses of the superpartners are very much larger than the TeV scale then we return to a situation when the radiative corrections are large and fine tuning is present.[10] As an example, in the decoupled regime, the tree level Higgs mass and the radiative correction at one-loop level from the stop and top only are [48][49]:

$$m_H^2 = m_Z^2 \cos^2 2\beta + \frac{3}{2\pi^2}\frac{m_t^4}{v^2}\left[\ln\frac{M_{\mathrm{SUSY}}^2}{m_t^2} + \frac{X_{\mathrm{SUSY}}^2}{M_{\mathrm{SUSY}}^2}\left(1 - \frac{X_{\mathrm{SUSY}}^2}{12M_{\mathrm{SUSY}}^2}\right)\right] + \dots , \tag{2.17}$$

where M_{SUSY} is the geometric mean of the masses of the two stop particles. X_{SUSY} is defined by $X_{\mathrm{SUSY}} = A_t - \mu\cot\beta$ where A_t is the trilinear coupling of the stop particles. Equation 2.17 shows that there will still be large corrections to the Higgs mass if the masses of the SUSY partners are large. The stop particle therefore cannot be much heavier than the top otherwise this loop correction becomes large and fine tuning returns.

The gluino gives large contributions to the stop masses at one-loop level such that it contributes to the Higgs mass at two loops. Therefore to avoid large corrections the gluino is also required to be relatively light. As the mass of the Z boson is also dependent on the parameter μ which directly determines the masses of the Higgsinos, these must also be light [49]. Large fine tuning is not introduced if the other superpartners are much more massive, however, the breaking mechanism would need to introduce this asymmetry. The amount of fine tuning that is permitted is a matter of taste and is not discussed here.[11]

[10] The reason that large corrections to the Higgs mass leads to fine tuning comes from the relationship between the Higgs mass and the Z boson mass which is given at tree level in the MSSM by:

$$m_Z^2 = \frac{|m_{H_d}^2 - m_{H_u}^2|}{\sqrt{1-\sin^2 2\beta}} - m_{H_u}^2 - m_{H_d}^2 - 2|\mu|^2. \tag{2.16}$$

Loop corrections can be included (at the one-loop level) using an effective potential by modifying m_{H_u} and m_{H_d}. It is clear that if these receive large corrections then to get m_Z at $\sim 90\,\mathrm{GeV}$ a large cancellation between μ and the corrected Higgs masses will be required such that we are back to a fine tuned situation.

[11] The observation of a new boson with a mass around 125 GeV obviously causes some tension as the second term in Equation 2.17 must be reasonably large to achieve this. Scans across parameter space (eg. [50]) show that there still do exist areas with low fine tuning and there is also the possibility that nature is not minimal

2.2.5 The MSUGRA/CMSSM Model

The MSUGRA model (Minimal SUper-GRAvity) which is also known as the CMSSM (constrained-MSSM) it a version of the (R-Parity conserving) MSSM with a defined set of boundary conditions set at the coupling unification scale [52, 53]. Historically it has been used as a benchmark for searches at colliders although with the most recent results from the LHC some tension is developing with experimental results [54, 55]. Here it is used an an example to demonstrate search sensitivity.

The MSUGRA/CMSSM model assumes the following relations at the coupling unification scale (M_U)[12]:

- Gaugino mass unification: $M_1(M_U) = M_2(M_U) = M_3(M_U) \equiv m_{1/2}$.
- Universal scalar masses: $m_Q = m_{\bar{u}} = m_{\bar{d}} = m_L = m_{\bar{e}} = m_{H_u} = m_{H_d} \equiv m_0$.
- Universal trilinear couplings: $\mathbf{A_u}(M_U) = \mathbf{A_d}(M_U) = \mathbf{A_e}(M_U) \equiv A_0\mathbf{1}$.

The only remaining free parameters in the model are b and μ from the Higgs(-Higgsino) sector. By using the minimisation of the Higgs potential conditions that satisfy the observed Z boson mass these two degrees of freedom can be reduced to the ratio of the two vacuum expectation values, $\tan\beta$, and the sign of μ. A complete MSUGRA/CMSSM model is therefore given by four continuous and one discrete degree of freedom; m_0, $m_{1/2}$, A_0, $\tan\beta$ and sign(μ), which specify the masses and couplings at the unification scale. These masses are then run down to the electroweak scale using the renormalisation group equations (RGEs). Typically exclusion limits from hadron colliders are displayed in the m_0 and $m_{1/2}$ plane for fixed values (or relations) of the other parameters since m_0 and $m_{1/2}$ are closely related to the coloured particle masses upon which the cross-section depends strongly.

2.2.6 The pMSSSM and Simplified Models

The model above clearly makes a lot of assumptions about the SUSY breaking sector so alternative methods of parametrising our ignorance have also been explored. The first step that

in which case there can be additional tree level contributions (eg. in the NMSSM [51]).

[12]This is the scale at which the gauge couplings become identical; $\alpha_1(M_U) = \alpha_2(M_U) = \alpha_3(M_U) \equiv \alpha_U$.

can be taken away from a model such as MSUGRA/CMSSM is to define the SUSY breaking parameters at the SUSY breaking scale such that RGE evolution is not necessary. The pMSSM [56] embodies this approach and has 19 free parameters which are motivated by respecting the flavour and CP constraints while allowing for as varied a spectrum as possible. The free parameters used are:

- $\tan\beta$ - ratio of Higgs vacuum expectation values.
- M_A - the mass of the pseudo-scalar Higgs boson.
- μ - the Higgs-higgsino mass parameter.
- M_1, M_2 and M_3 - the bino, wino and gluino mass parameters.
- $m_{\tilde{Q}_{1,2}}, m_{\tilde{u}_R,\tilde{c}_R}, m_{\tilde{d}_R,\tilde{s}_R}, m_{\tilde{L}_{1,2}}, m_{\tilde{e}_R,\tilde{\mu}_R}$ - the mass parameters of the first two generations of squarks and sleptons.
- $m_{\tilde{Q}_3}, m_{\tilde{t}_R}, m_{\tilde{b}}, m_{\tilde{L}_3}, m_{\tilde{\tau}_R}$ - the mass parameters of the third generation squarks and sleptons.
- $A_t = (\mathbf{A_u})_{3,3}$, $A_b = (\mathbf{A_d})_{3,3}$ and $A_\tau = (\mathbf{A_u})_{3,3}$ - the trilinear couplings of the third generation particles.

The simplest possible parametrisation of the SUSY spectrum is embodied in "simplified models". In a simplified model the masses of all the SUSY particles are put at high values ($>>1$ TeV) apart from a select few which are kinematically accessible. The branching ratios between these are then assumed and the values given. This obviously does not give a complete picture of a model but does show what areas of parameter space a search is sensitive to in an easy to visualise way. For example, the results of the search presented later are presented in a plane of gluino mass against $\tilde{\chi}_1^0$ mass when all other SUSY particles are put beyond the LHC reach and the gluino is forced to decay with 100% branching ratio to $t\bar{t}\tilde{\chi}_1^0$. This model is easy to envisage and is also well motivated by the naturalness arguments discussed in §2.2.4 as the gluino is light and the lightest stop can be slightly more massive than the gluino with all the other coloured sparticles having much larger masses. In this situation this decay mode will have

large branching ratio. A conservative estimate of the sensitivity of the analysis to any model like this can be obtained using a modified cross-section to account for the branching ratio.

2.3 Conclusions of the Theoretical Motivation

At the beginning of this chapter the Standard Model of particle physics was presented. The Higgs mechanism of electroweak symmetry breaking was detailed such that the "hierarchy problem" could be described in detail. Having established a significant problem with the Standard Model, supersymmetry was introduced as a possible solution to this problem. After establishing some of the notation usually used to describe supersymmetrc theories, the Minimal Supersymmetric Standard Model (MSSM) was introduced. The extended Higgs sector present in the MSSM was explained and the soft breaking terms were presented. The phenomenological properties of the particle content of the MSSM were described before R-Parity was introduced to avoid operators that would allow rapid decay of protons. The full undiscovered particle content of the MSSM is given in Table 2.2. As supersymmetry is broken, the cancellation of the dangerous contributions to the Higgs mass will not be complete. The conditions required to keep models natural were discussed in §2.2.4. Finally, several models were presented; one where supersymmetry was broken at the unification scale, MSUGRA/CMSSM; one where our ignorance was parametrised by breaking at the SUSY breaking scale such that RGE evolution is not necessary, the pMSSM; and finally the idea of simplified models where masses and parameters are fixed with most particles placed beyond the reach of the LHC.

Supersymmetry is therefore a well motivated theory which suffers from two obvious problems: the lack of observation of any of the particles in Table 2.2 and the lack of knowledge of the breaking mechanism of the symmetry. These two problems are clearly linked – observation of the SUSY mass spectrum will give clues as to the breaking mechanism. Therefore, we turn now to experiment to search for the particles in Table 2.2.

Name	**Spin**	P_R	**Gauge Eigenstates**	**Mass Eigenstates**
Higgs bosons	0	+1	H_u^0, H_d^0, H_u^+, H_d^-	h^0, H^0, A^0, $H^\pm$
squarks	0	-1	$\tilde{u}_L$, $\tilde{u}_R$, $\tilde{d}_L$, $\tilde{d}_R$	same as left
			$\tilde{c}_L$, $\tilde{c}_R$, $\tilde{s}_L$, $\tilde{s}_R$	same as left
			$\tilde{t}_L$, $\tilde{t}_R$, $\tilde{b}_L$, $\tilde{b}_R$	$\tilde{t}_1$, $\tilde{t}_2$, $\tilde{b}_1$, $\tilde{b}_2$
sleptons	0	-1	$\tilde{e}_L$, $\tilde{e}_R$, $\tilde{\nu}_e$	same as left
			$\tilde{\mu}_L$, $\tilde{\mu}_R$, $\tilde{\nu}_\mu$	same as left
			$\tilde{\tau}_L$, $\tilde{\tau}_R$, $\tilde{\nu}_\tau$	$\tilde{\tau}_1$, $\tilde{\tau}_2$, $\tilde{\nu}_\tau$
neutralinos	$\frac{1}{2}$	-1	$\tilde{B}^0$, $\tilde{W}^0$, $\tilde{H}_u^0$, $\tilde{H}_d^0$	$\tilde{\chi}_1^0$, $\tilde{\chi}_2^0$, $\tilde{\chi}_3^0$, $\tilde{\chi}_4^0$
charginos	$\frac{1}{2}$	-1	$\tilde{W}^\pm$, $\tilde{H}_u^+$, $\tilde{H}_d^-$	$\tilde{\chi}_1^\pm$, $\tilde{\chi}_2^\pm$
gluino	$\frac{1}{2}$	-1	$\tilde{g}$	same as left

Table 2.2: The MSSM particles that have not yet been discovered. The Higgs is listed despite the observation of a boson resembling a Higgs at the LHC as its properties are still to be confirmed. The first two generations of sleptons and squarks are assumed to mix negligibly as is the case in all the models considered here.

Chapter 3

Non-LHC Experimental Constraints

Prior to the operation of the LHC various searches had been performed for supersymmetric particles at other colliders. The limits from the Large Electron-Positron Collider (LEP) at CERN on the weakly interacting particles remain competitive due to the clean operating environment of lepton colliders. The Tevatron searches for strongly interacting particles were the strongest for coloured sparticles, however these were quickly surpassed by the LHC limits due to the higher operating centre of mass energy. There are also constraints that come from low energy precision data such as the branching fractions of heavy meson rare decays and the anomalous magnetic moment of the muon. Finally there is the compatibility of the predicted dark matter relic density of a model with that observed.

3.1 LEP Constraints

The Large Electron-Positron Collider (LEP) operated at CERN between 1989 and 2000 with a maximum achieved centre of mass energy of $\sqrt{s} = 209\,\text{GeV}$. Four detectors, OPAL [57], ALEPH [58], DELPHI [59] and L3 [60], recorded the collisions and performed direct searches for supersymmetric particles.

Limits on charginos ($\tilde{\chi}^{\pm}$) from LEP are very general and can apply to almost all corners of parameter space. One analysis performed a general search [61] for charginos, while another one specifically targeted scenarios where the chargino and the LSP are close to degenerate in mass [62]. The first of these set a limit assuming gaugino mass unification (at M_U) that

charginos masses must be > 103.5 GeV provided the sneutrinos are heavier than 300 GeV. The sneutrino mass condition is required as there is destructive interference in chargino production if the sneutrinos are light. In the low mass splitting analysis two scenarios are considered, a wino-like chargino close to degenerate with a bino LSP and a higgsino-like chargino close to degenerate with a bino LSP. For all values of mass splitting charginos are excluded up to masses of 92.4 GeV and 91.9 GeV respectively in the two scenarios, again under the condition that the sneutrinos are heavy.

Similarly the LEP limits on the superpartners of the charged leptons are very clean [63]. Limits are quoted on right-handed selectrons and smuons as these tend to have lower cross-section than their left-handed counterparts so are seen as conservative. The rest of the model is defined by mass unification (at M_U) of M_1 and M_2, and $\tan\beta = 1.5$, $\mu = -200\,\text{GeV}$. Selectrons (Smuons) with masses less than 93.5 (94.5) GeV are excluded provided $m_{\tilde{l}_R} - m_{\tilde{\chi}_1^0} > 4\,\text{GeV}$. The selectron limits improve to $m_{\tilde{e}_R} > 98.5\,\text{GeV}$ for mass splittings of greater than 10 GeV. The stau is generally a mix of both right and left handed eigenstates. A limit of $m_{\tilde{\tau}_1} > 86.2\,\text{GeV}$ is found for purely right-handed $\tilde{\tau}_1$ provided $m_{\tilde{\tau}_1} - m_{\tilde{\chi}_1^0} > 7\,\text{GeV}$.

The invisible width of the Z boson was measured accurately at LEP [37]. The consistency of the measurement with the presence of three generations of light, active neutrinos sets a limit on the mass of the sneutrinos to be larger than $45\,\text{GeV}$. This can also be used to set limits on the lightest neutralino, however, depending on the nature of the lightest neutralino the Z-neutralino coupling can be small such that there is no general limit.

At LEP there were also searches for the third generation squarks [64]. Limits were set in the MSSM considering the case when the lightest squark was purely left-handed and the case when the mixing angle minimised the LEP cross-section. Results were presented for stop pair production followed by the decay $\tilde{t}_1 \to c + \tilde{\chi}_1^0$ and sbottom pair production followed by the decay $\tilde{b} \to b + \tilde{\chi}_1^0$. For the former stops are excluded with masses below 93 GeV provided $m_{\tilde{t}_1} - m_{\tilde{\chi}_1^0} > 6\,\text{GeV}$, and for the later sbottoms are excluded with masses below 92 GeV provided $m_{\tilde{b}_1} - m_{\tilde{\chi}_1^0} > 6\,\text{GeV}$, both in the conservative mixing scenario.

Compared to hadron colliders the LEP limits on 1st and 2nd generation squarks and gluinos are weak so are not relevant.

3.2 Tevatron Constraints

The CDF [65] and D0 [66] detectors at the Tevatron $p\bar{p}$ collider searched for direct production of pairs of supersymmetric particles. Being a hardon collider the limits on particles from the coloured sector are strong.

Searches for squarks and gluinos were carried out in the final state of multiple high p_{T} jets, large $E_{\mathrm{T}}^{\mathrm{miss}}$ and either no highly electromagnetic or single track jets (CDF), or no identified electrons or muons (D0). No significant excess was observed in either analysis and limits of the mass of first two generation squarks and gluinos are interpreted in the $m_0, m_{1/2}$ plane of the MSUGRA/CMSSM with $A_0 = 0$, $\mu < 0$ and $\tan\beta = (5, 3)$ (CDF, D0) [67][68]. Limits exclude gluinos with masses below (280, 308) GeV independent of the squark masses in their respective models. CDF also excludes gluinos with masses below 392 GeV in their model under the condition $m_{\tilde{g}} = m_{\tilde{q}_{1,2}}$. D0 excludes squarks with masses below 379 GeV across the whole phase space of their model. These represented the most stringent tests of this model pre-LHC.

There were also searches at the Tevatron for the third generation squarks. CDF and D0 searched for stop quarks decaying to $c + \tilde{\chi}_1^0$ with 2.6fb^{-1} and 1fb^{-1} respectively. Stop quarks with masses below 180 GeV were excluded for the case with the largest kinematically allowed mass splitting [69][70]. CDF also searched for stop quarks decaying $\tilde{t} \to \tilde{\chi}_1^{\pm}(\to l\nu\tilde{\chi}_1^0)b$ in the di-lepton channel and stop quarks with masses between 128 GeV and 135 GeV for chargino and LSP masses near the LEP bounds for these particles [71]. Searches for sbottom quarks decaying $\tilde{b} \to b\tilde{\chi}_1^0$ excluded sbottom quarks with masses below 247 GeV for the massless LSP case with the limit weakening to exclude $160 < m_{\tilde{b}_1} < 200\,\mathrm{GeV}$ for $m_{\tilde{\chi}_1^0} = 110\,\mathrm{GeV}$ [72][73].

3.3 Low Energy Constraints

The presence of supersymmetric particles can affect the expected rates of rare decays and will also alter other observables such as the anomalous magnetic moment of the muon. In general the differences to the Standard Model values can be positive or negative as the additional loops can either contribute constructively or destructively. When considering complete models large areas of parameter space can be excluded by low energy constraints, in particular the observed

branching fraction of $b \to s\gamma$ [74], the recent evidence for $B_s \to \mu^+\mu^-$ [75] and $(g-2)_\mu$ [76]. As an example see [54] or [55] for how these constraints affect the MSUGRA/CMSSM model.

3.4 Dark Matter Constraints

Two types of constraint on SUSY models come from dark matter: the compatibility with the observed relic density and that predicted by the model, and the compatibility of the nature of the relic density with constraints from direct and indirect dark matter detection experiments. Constraints from direct and indirect dark matter detection experiments are highly model dependent and rely on modelling the density and velocity distribution of dark matter either locally (direct) or in particular areas of the galaxy (indirect) so are not considered here. For the MSUGRA/CMSSM case the effect of dark matter detection experimental results under the usual assumptions are given in [54] and [55].

The WMAP Collaboration has measured the dark matter relic density of the universe to be $\Omega_{DM} \simeq 0.227 \pm 0.014$ [30]. The Standard Model of cosmology can be used to evaluate the compatibility of a given model with this dark matter content of the universe. As an example Figure 3.1(a-c) shows three planes of the pMSSM. The SUSY spectrum and decay table is computed using SOFTSUSY-3.3.3 [77] and SUSY-HIT [78], then the relic density is computed using micrOMEGAs-2.4.5 [79]. The axes chosen are those which determine the neutralino mass spectrum and hence the nature and mass of the LSP. It is clear from the plots that by choosing the nature of the LSP carefully the dark matter relic density can match that observed. However, it should be noted that it is not a requirement that a SUSY model saturates this bound as the supersymmetric component may only be a small fraction of the total dark matter in the Universe. There are several mechanisms that can be used to reduce the relic density of a particular model. For example if another supersymmetric particle is placed close in mass to the LSP then co-annihilation can occur and the predicted relic density is dramatically reduced. This is an effective way of allowing LSPs with high bino fraction to not over-close the universe. An example of this is shown in Figure 3.1(d). Figure 3.2 shows the compatibility of the MSUGRA/CMSSM model used for interpretation later in the described analysis.

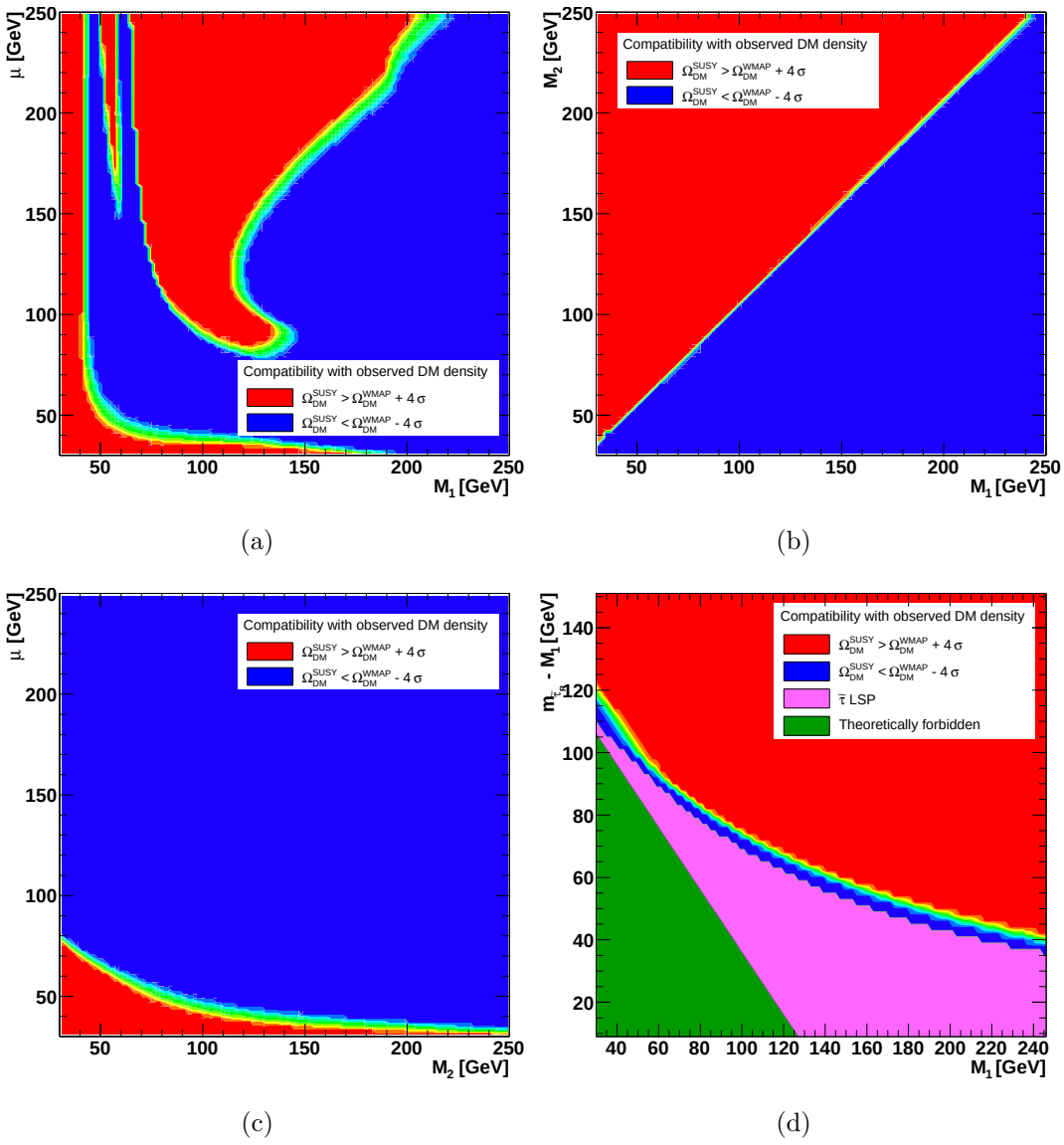

Figure 3.1: The compatibility of four pMSSM planes with the WMAP measured Dark Matter relic density. The central green band denotes compatibility within 1σ with successive bands denoting compatibility within 2, 3, 4 and $>4\sigma$. The red coloured regions possess too large a dark matter relic density and the blue regions do not saturate the WMAP measured Dark Matter relic density. The pMSSM model parameters other than those shown are set to high scale such that they have little influence on the system; $(M_1, M_2, M_3, A_t, M_A, \mu) = 2\,\text{TeV}$, $(m_{\tilde{Q}_3}, m_{\tilde{t}_R, \tilde{b}_R}) = 1\,\text{TeV}$, $(m_{\tilde{Q}_{1,2}}, m_{\tilde{u}_R, \tilde{c}_R}, m_{\tilde{d}_R, \tilde{s}_R}, m_{\tilde{L}_{1,2}}, m_{\tilde{L}_3}, m_{\tilde{e}_R, \tilde{\mu}_R}, m_{\tilde{\tau}_R}) = 4\,\text{TeV}$, $(A_b, A_\tau) = 0$, $\tan\beta = 10$.

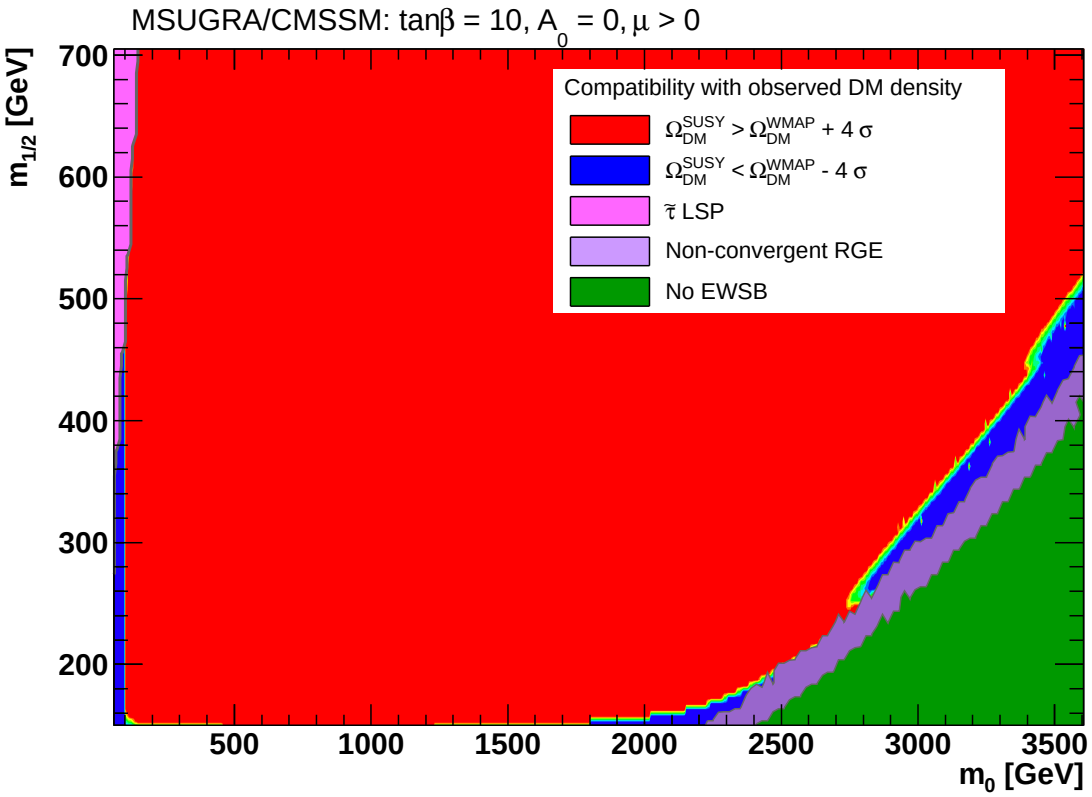

Figure 3.2: The compatibility of a plane of the MSUGRA/CMSSM parameter space with the WMAP measured Dark Matter relic density. The colour scheme is as in Figure 3.1.

Chapter 4

The ATLAS Detector

The ATLAS experiment [8] is a multi-purpose particle physics detector with a forward-backward symmetric cylindrical geometry and nearly 4π coverage in solid angle.[1] The layout of the detector is dominated by four superconducting magnet systems, which comprise a thin solenoid surrounding inner tracking detectors, and a barrel and two end-cap toroids supporting a large muon spectrometer. An inner detector consisting of a silicon pixel detector, a silicon strip detector and a transition radiation detector provide tracking information. The calorimeters are of particular importance to this analysis. In the pseudorapidity region $|\eta| < 3.2$, high-granularity liquid-argon (LAr) electromagnetic sampling calorimeters are used. An iron/scintillator-tile calorimeter provides hadronic coverage for $|\eta| < 1.7$. The end-cap and forward regions, spanning $1.5 < |\eta| < 4.9$, are instrumented with LAr calorimetry for both electromagnetic and hadronic measurements. Outside the toroid magnet there are muon detectors. The layout of the detector is shown in Figure 4.1.

A full description of the detector can be found elsewhere [80] such that here the technologies and performance are briefly summarised. More detail is given for the calorimeters as these are more relevant for the analysis discussed here. Additionally the ATLAS trigger system is described in §4.6 with particular details of the $E_{\mathrm{T}}^{\mathrm{miss}}$ trigger given in §4.6.1 as I was closely involved with this trigger during the course of my D.Phil.

[1] ATLAS uses a right-handed coordinate system with its origin at the nominal interaction point in the centre of the detector and the z-axis along the beam pipe. Cylindrical coordinates (r, ϕ) are used in the transverse plane, ϕ being the azimuthal angle around the beam pipe. The pseudorapidity η is defined in terms of the polar angle θ by $\eta = -\ln\tan(\theta/2)$.

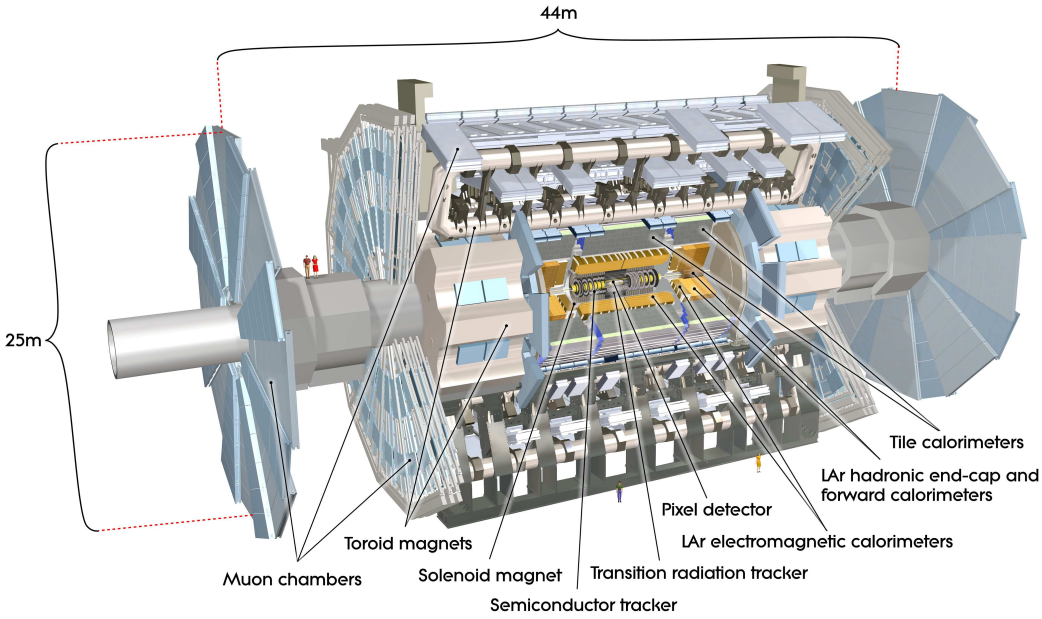

Figure 4.1: Cut-away view of the ATLAS detector. The dimensions of the detector are 25 m in height and 44 m in length. The overall weight of the detector is approximately 7000 tonnes [8].

4.1 The Large Hadron Collider

The Large Hadron Collider (LHC) delivers luminosity to the ATLAS detector. The protons are initially accelerated by a linear accelerator which then feeds them into the PS Booster and Proton Synchrotron. These accelerate the proton beams to 26 GeV and they are then fed into the Super Proton Synchrotron (SPS). The SPS is 7 km in circumference and accelerates the beams to 450 GeV. This is the injection energy to the LHC.

The LHC is 27 km in circumference and 1,232 superconducting di-pole magnets are used to bend the beams round the ring. The LHC increases the beam energies using radio frequency (RF) cavities and quadrupole magnets are used to focus the beam to maximise the luminosity delivered per crossing.

In 2010 and 2011 the beams were accelerated to 3.5 TeV giving a centre of mass collision energy of 7 TeV. In 2012 this was increased to give a centre of mass collision energy of 8 TeV. In 2010 the LHC delivered an integrated luminosity of 48.1 pb^{-1}. In 2011, 5.61 fb^{-1} was delivered and 23.3 $fb^{-1}$of 8 TeV data was delivered in 2012. The larger amount of data taken in the latter years was achieved by increasing the instantaneous luminosity. This resulted in many interactions per crossing with an average mean number of interactions per crossing in 2012 of

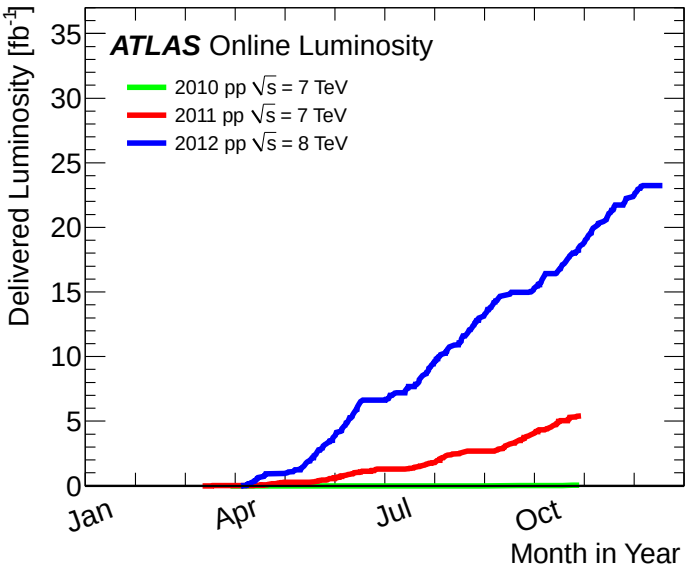

Figure 4.2: The cumulative luminosity delivered to ATLAS by the LHC in 2010, 2011 and 2012 [81].

20.7 [81]. The effect of these additional interactions on the analysis is discussed further in §7.5.

The proton beams are structured into trains of many bunches of protons. The spacing between bunches within the train was 75 ns in 2010 and the first part of 2011 and was then shortened to 50 ns for the rest of 2011 and 2012 running. This parameter is of particular importance for the ATLAS detector as the total response time of the calorimeters is much longer than this such that observations are affected by collisions both before and after the collision of interest. These effects need to be corrected for in the jet calibration discussed in §4.4.3.

4.2 The Magnet Systems

Four large superconducting magnets are present in ATLAS. The inner-most of these is a solenoid magnet that surrounds the inner detector and is inside the calorimeters. This provides a 2 T magnetic field for measuring charged particles' momenta. Due to the position of this magnet care is taken to keep the material budget of the full structure low. To achieve this the material of the coil (Al-stabilised NbTi) and the heat shield (Al) were carefully chosen and the magnet shares the same vacuum vessel as the electromagnetic calorimeter. The steel in the hadronic calorimeter is used to return the flux of the magnet further reducing the necessary material

budget. Outside the calorimeter systems lie three toroid magnets which produce a magnetic field for the muon spectrometer. In the barrel region the field strength is approximately 0.5 T, while in the end-cap regions it is approximately 1 T.

4.3 Inner Detector

The ATLAS inner detector uses three different sub-detectors to provide accurate tracking information. Nearest the interaction point is the pixel detector extending radially outwards from 45.5 mm to 242 mm, surrounding the pixel detector is a silicon microstrip detector (SCT) which extends radially out to 549 mm. Finally, a straw tube Transition Radiation Tracker (TRT) extends the tracking in the central region radially outward from 554 mm to 1082 mm. Figure 4.3(a) shows a cut-away view of the three inner detectors and Figure 4.3(b) shows a schematic diagram of the location of the various parts of the inner detector.

Pixel detector

The pixel detector sits closest to the beamline. This detector therefore used the most novel and leading-edge technology such that the high radiation conditions could be tolerated. The detector consists of three barrel layers at radii of 50.5, 88.5 and 122.5 mm from the beam axis and three disks on either side with inner and outer radii of 88.8 mm and $R = 149.6$ mm respectively. Tracking is present up to $|\eta| = 2.5$ and the layers are arranged so typically a track has to pass through three layers.

SCT detector

Outside the pixel detector is a silicon microstrip detector (SCT). Again tracking is provided up to $|\eta| = 2.5$ and the detector consists of a series of barrels and disks. Four barrels of radii from 299 mm to 514 mm cover the tracking in the central region. Nine disks on either side provide tracking at higher pseudorapidities. In each layer of the barrel there are strips that lie parallel to the beam axis that measure in r-ϕ and also strips at a small stereo angle such that the longitudinal position can also be determined. A similar configuration is present in the disks. The layout of the layers is such that four layers are traversed by each track.

TRT detector

Finally, a transition radiation detector (TRT) completes the inner detector tracking. This consists of two central sections, joined at approximately $\eta = 0$, with an end-cap at either side. In the barrel straw tubes of 4 mm diameter lying parallel to the beam direction provide r-ϕ information for tracking with approximately 30 hits expected per track. In the end-caps the straw tubes are arranged radially.

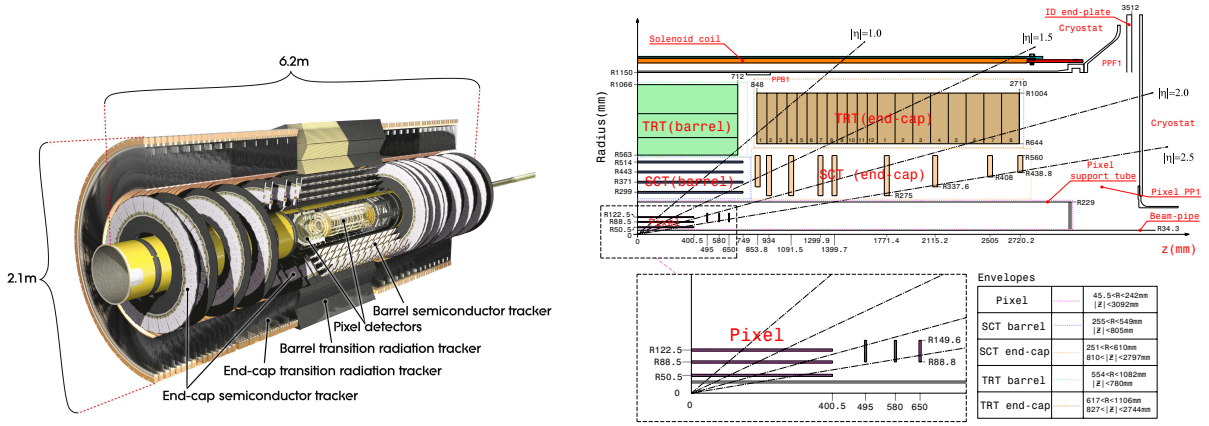

(a) (b)

Figure 4.3: (a) A cut-away view of the ATLAS inner detector [8]. (b) The layout of the layers of the inner detector [8].

4.4 Calorimeters

Two different technologies are used in the ATLAS calorimeters. Liquid Argon (LAr) technology is used for electromagnetic calorimetry up to $|\eta| = 3.2$ and for hadronic calorimetry from $|\eta| = 1.5$ up to the most forward acceptance of $|\eta| = 4.9$. An Iron-Scintillator hadronic calorimeter (the "Tile Calorimeter") is used at larger radii up to $|\eta| = 1.7$. Figure 4.4 shows a drawing of the calorimeters - fuller details of the positions and design of the calorimeters are given in the following sub-sections. Following this in §4.4.3 the methods employed to cluster calorimeter cells to reduce noise and their subsequent calibration are described.

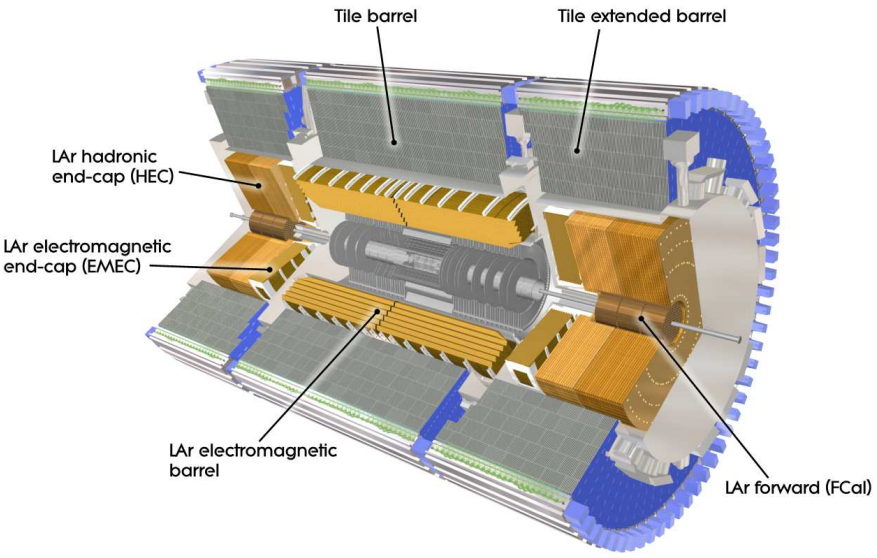

Figure 4.4: A cut-away drawing of the ATLAS calorimeters [8].

4.4.1 Liquid-Argon Calorimeter (LAr)

The liquid-Argon sampling calorimeter in ATLAS is divided up into several different components each housed in their own cryostat[2]. A central barrel and two (one each side) end-caps provide electro-magnetic calorimetry, while further out in z two hadronic end-caps are deployed. Finally, the very forward region is covered by two additional calorimeters. The different components consist of several layers and a "pre-sampler" is used to recover energy lost in the material in front of the calorimeter. The positions in $|\eta|$ of the different components are given in Table 4.1.

Electromagnetic barrel calorimeter

In the barrel accordion-shaped electrodes and lead absorber plates are used to ensure uniformity around ϕ is achieved. The first sampling layer has a finer η granularity to aid in the reconstruction of the precise pointing of photons in this plane. Figure 4.5 shows this structure. The calorimeter is designed to contain electromagnetic showers, so accurate measurement of electrons and photons can be achieved. Figure 4.6(a) shows the depth of the EM calorimeter in units of radiation length. For the barrel region over 25 radiation lengths are present. It can also be seen in Figure 4.6(a) that significant material is present before the main accordion calorime-

[2]The end-cap and forward calorimeters share the same cryostats

	Barrel	End-cap
EM Calorimeter		
Pre-sampler	$\|\eta\| < 1.52$	$1.5 < \|\eta\| < 1.8$
1st layer	$\|\eta\| < 1.475$	$1.375 < \|\eta\| < 3.2$
2nd layer	$\|\eta\| < 1.475$	$1.375 < \|\eta\| < 3.2$
3rd layer	$\|\eta\| < 1.35$	$1.5 < \|\eta\| < 2.5$
LAr hadronic end-cap		
All 4 layers	-	$1.5 < \|\eta\| < 3.2$
LAr forward calorimeter		
1st layer	-	$3.1 < \|\eta\| < 4.83$
2nd layer	-	$3.2 < \|\eta\| < 4.81$
3rd layer	-	$3.29 < \|\eta\| < 4.75$

Table 4.1: The $|\eta|$ coverage of the different components of the LAr calorimeter.

ter. To recover this energy a pre-sampler is placed in front of the main accordion calorimeter. The principle of this is to use the material in front of the pre-sampler as an absorber and the pre-sampler itself consists of an instrumented, active liquid argon layer. In Figure 4.6(b) the depth of material in front of this can be seen in detail. It should be noted that at the junction between the barrel and end-cap there exists a region (known as the *crack*) where performance is slightly degraded.

Electromagnetic end-cap calorimeter

As with the barrel LAr calorimeter, the electromagnetic end-cap calorimeters use accordion-shaped electrodes and lead plates. They consist of wheels around the beam axis and the accordion-shaped electrodes lie in axial plane. The wheel covers pseudorapidities of $1.375 < |\eta| < 3.2$. Figure 4.6(c) shows the depth in radiation lengths across the end-cap region. As with the barrel, the presence of significant material prior to the calorimeter necessitates the use of a pre-sampler. This covers the pseudorapidity range of $1.5 < |\eta| < 1.8$. It is not necessary for the pre-sampler to extend to higher pseudorapidities as in these regions the dead material is lower and for a given p_{T} the energy of the particles is higher.

Hadronic end-cap calorimeter

Further along the z-axis from the electromagnetic end-cap calorimeter are two further wheels

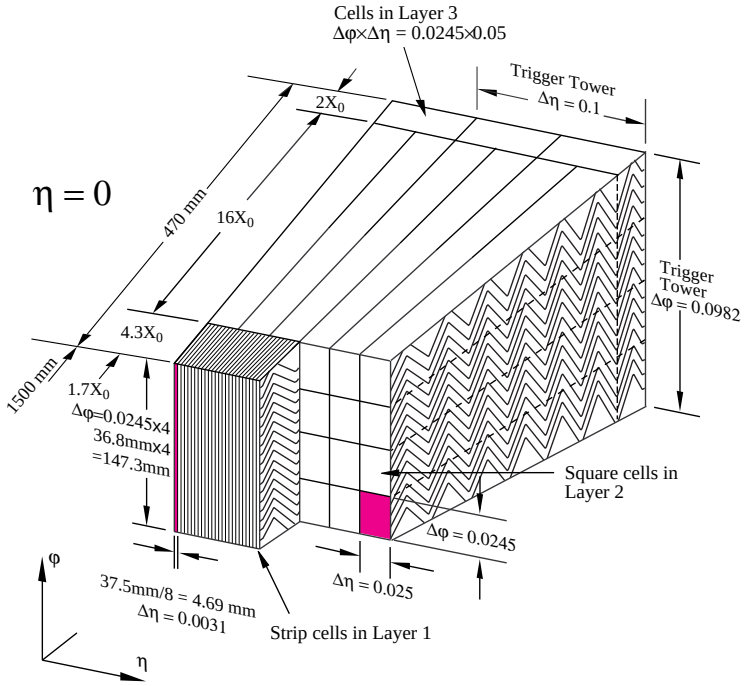

Figure 4.5: A sketch of the accordion and cell struction of the EM calorimeter [8].

for measuring hadronic showers. These use liquid Argon with copper plates as the absorption material. The copper is arranged in plates of 25 mm in the first and 50 mm in the second wheel, with 8.5 mm gaps between the plates. This results in a sampling fractions of 4.4% and 2.2% for the two wheels respectively. Hadronic showers are well contained within these detectors due to the large number of hadronic interaction lengths that they cover. Figure 4.7 shows the depth of the calorimeter. It can be seen that about 12 interaction lengths are present in the region of the hadronic end-cap calorimeter.

Forward calorimeter

In the very forward region there exists three sections of calorimeter; the first is a copper/liquid-argon designed for electromagnetic measurements while the other two are hadronic calorimeters made from tungsten/liquid-argon. Copper is used for its good resolution and ability to remove heat from the system. The hadronic calorimeters are designed to be very dense so many interaction lengths are present but also such that lateral shower size is small. The motivation for this is to ensure that there is little leakage from the Forward calorimeter into the hadronic end-cap calorimeter which would degrade the performance in high luminosity running conditions. Behind the Forward calorimeter there is a copper shielding plug to minimise the background

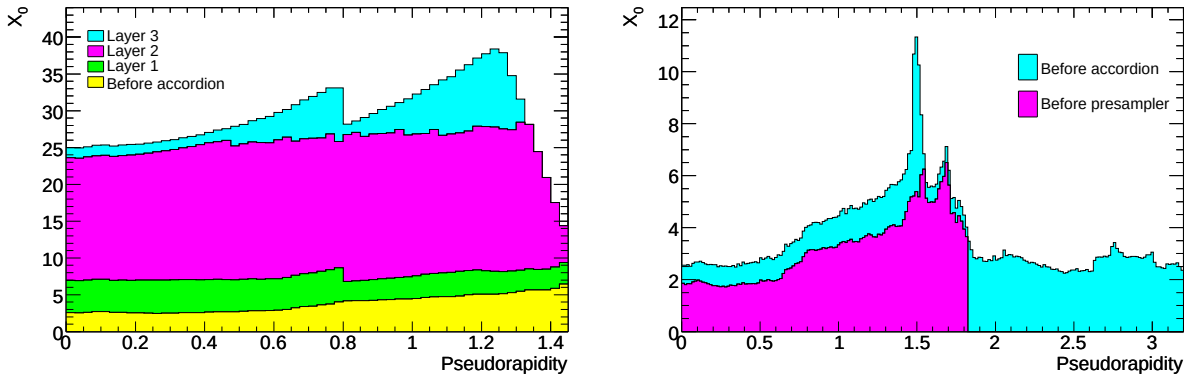

(a)

(b)

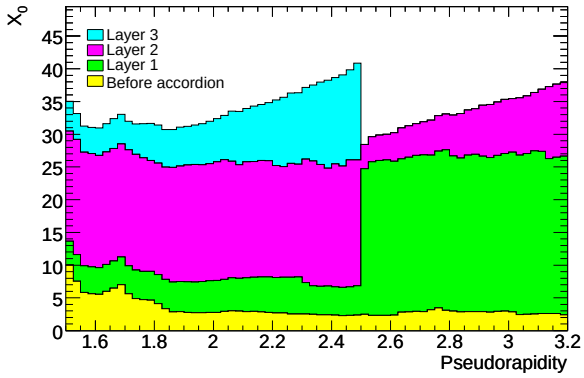

(c)

Figure 4.6: The cumulative depth of the electromagnetic calorimeters in units of radiation length, X_0, as a function of $|\eta|$. (a) shows the depth for the barrel calorimeter, (b) shows in detail the material in front of the accordion including the pre-sampler and (c) shows the depth for the electromagnetic end-cap [8].

hadronic activity reaching the muon systems.

4.4.2 Tile Calorimeter

In the central region the LAr calorimeter provides roughly one hadronic interaction length of active material. Therefore an additional calorimeter is required to contain hadronic showers - an iron/scintillator calorimeter known as the "Tile calorimeter" fulfils this role. The design of the calorimeter is a "central barrel" ($|\eta| < 1$) and two "extended barrels" outside ($0.8 < |\eta| < 1.7$). The design of the tile calorimeter is "tiles" of scintillator embedded in iron. These are arranged in rows radially and each row is offset from the previous one to give better coverage. This results in a sampling fraction of $\sim 4\%$. A diagram of a single module is shown in Figure 4.8. The calorimeter is required to minimise hadronic leakage which would otherwise give rise to tails in the jet response. As can be seen in Figure 4.7 other than for a very small region between the barrel and extended barrel over 9 interaction lengths of material are present ensuring that hadronic leakage is small. The calorimeter is designed to achieve an intrinsic resolution for jets of:

$$\frac{\Delta E}{E} = \frac{50\%}{\sqrt{E\,[\mathrm{GeV}]}} \oplus 3\%, \text{ for } |\eta| < 3.$$

Due to the non-compensating nature of the calorimeter there are intrinsic non-linearities, however using the longitudinal hadronic shower depth which can be measured using the granularity of the calorimeter this can be restored to the level of 1-2% [82].

4.4.3 Topo-clustering and Calibration

The ATLAS calorimeter systems consist of a very large number of individual cells such that if these are considered individually then the combined noise from both the read-out electronics and previous interactions in the calorimeter (as the calorimeter response is longer than the bunch crossing interval) would be significant. Furthermore, due to the fine granularity of the calorimeter, incoming particles will normally deposit their energy across many cells in both the lateral and longitudinal directions. Therefore it is desirable to use a clustering algorithm to group the cells from each object in a way which reduces noise terms.

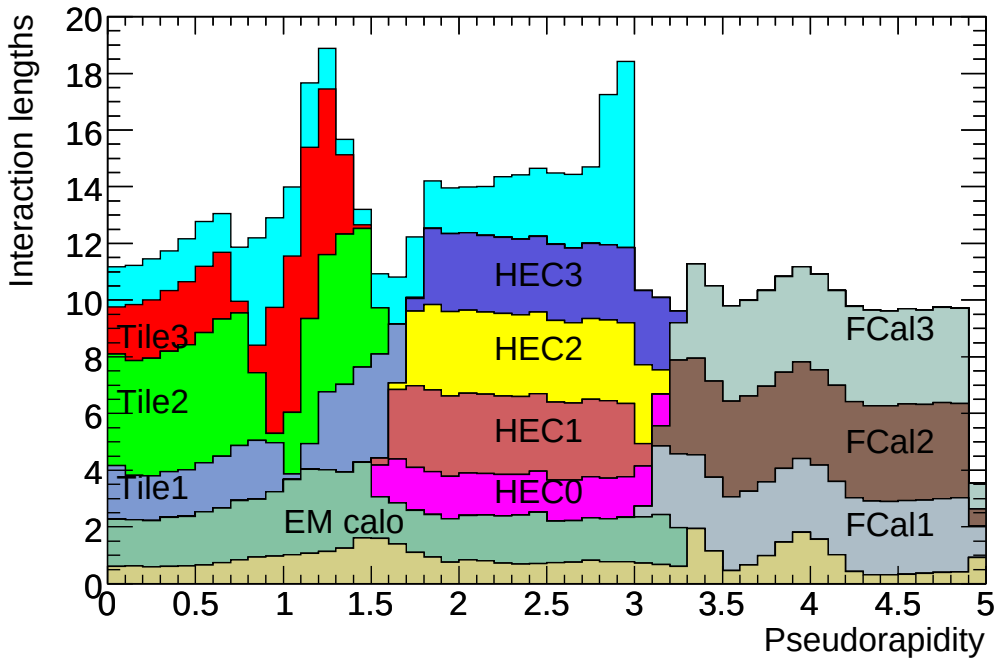

Figure 4.7: The cumulative depth in units of hadronic interaction length of the different layers of the hadronic calorimeter as a function of $|\eta|$ as well as the material in front of the calorimeter. The first and second wheels of the hadronic end-cap are split into two layers each [8].

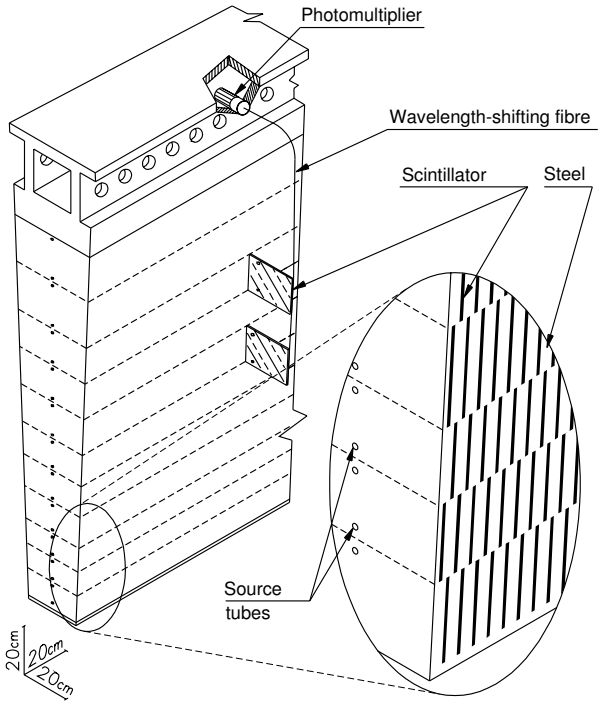

Figure 4.8: A tile module [8].

ATLAS utilises a topological clustering algorithm to cluster calorimeter cells to form "topological clusters" [83] from which jets are formed and the $E_{\mathrm{T}}^{\mathrm{miss}}$ is calculated. For each cell the noise threshold is estimated and clusters are seeded by cells with signal-to-noise ratio greater than 4. For each cluster, adjacent cells with signal-to-noise ratio greater than 2 which are not already a member of a cluster are added to that cluster. If the cell is adjacent to two clusters then the clusters are merged. This is repeated iteratively until no more cells are being added. At that stage all adjacent cells are then added to the clusters. This final step ensures that the edges of showers are not missed. As many clusters may be close to each other, additional cluster splitting is performed by looking for energy maxima within clusters. This ensures that clusters do not grow to cover large areas of the detector when large energy deposits are present. This procedure limits the noise contributions while the maximal information is retained.

Electromagnetic and hadronic energy deposits will result in different responses in the ATLAS calorimeters due to their non-compensating nature. Two different calibration schemes for hadronic jets are used in ATLAS. In the simpler one, known as "EM+JES", the energy of a jet is corrected using a multiplicative factor, dependent on p_{T} and η, to account for the difference between hadronic and electromagnetic showers[3] [86]. This corrects jets well on average but does not take into account jet-by-jet variations. The *local cluster weighting* (LC) scheme accounts for these variations by considering each topological cluster and determining from its characteristics if it is hadronic or electromagnetic in nature [87]. Clusters that are determined to be hadronic are then given a weighting factor at the cluster level based on single pion simulations and test beam measurements. Jets are then formed from these calibrated clusters before having a final correction factor applied similar in nature to that of the EM+JES scheme [86].

4.5 Muon Systems

The magnetic field provided by the toroid magnet causes muon tracks to bend and it is this curvature that is measured by the muon system. Different detector systems are used to provide

[3]This correction factor is determined to correct jets back the particle level and includes using data-driven methods to constrain the uncertainties [84]. Additionally in this calibration scheme corrections are applied to take account of jets originating from the beam spot rather than the centre of the detector and to account for the contributions to the jet from additional collisions [85]. The latter correction depends on the average number of interactions per crossing and the number of reconstructed vertices.

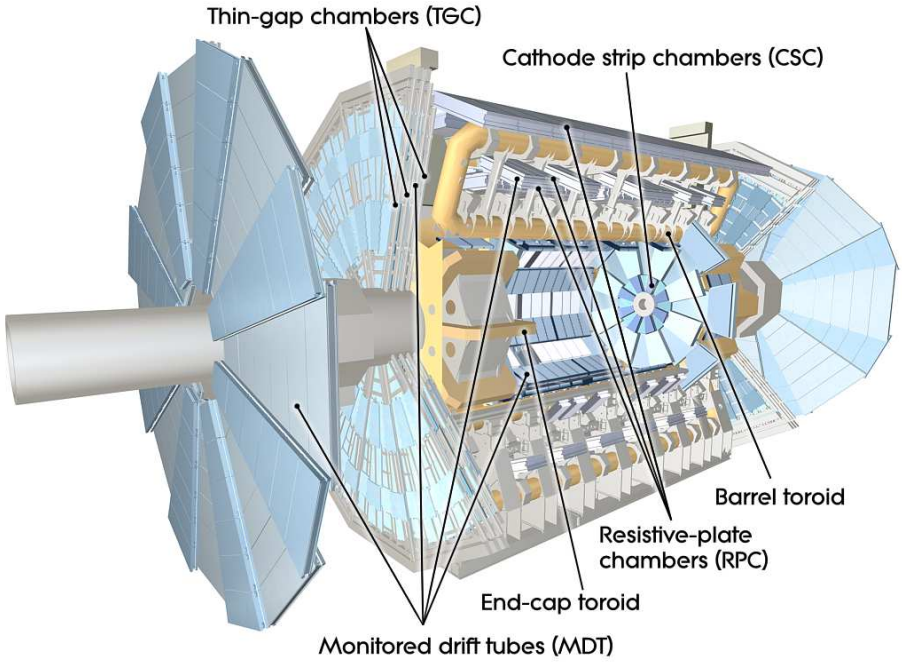

Figure 4.9: A cut-away drawing of the ATLAS muon detectors [8].

precision measurements and triggering. Precision tracking is achieved using monitored drift tubes (MDT) aided by cathode strip chambers (CSC) in the forward regions. Triggering in the most central regions is provided by resistive plate chambers (RPC) and thin gap chambers (TGC) up to $|\eta| = 2.4$. The positioning of the different systems can be seen in Figure 4.9. The triggering systems are also used to provide the coordinate in the non-bending ϕ plane as the precision chambers are designed to measure the η coordinate. The RPC and TGC technologies are chosen as tracking information can then be provided $O(10$ ns) after the particle passes through and with a time resolution narrow enough to correctly identify the correct beam crossing. The MDT measures precisely the coordinate in the bending, η, plane allowing the measurement of muon momenta from as low as ~ 3 GeV (limited due to energy losses in the calorimeters) up to the highest energies.

4.6 Trigger

ATLAS operates a three level trigger system. The first level, Level 1 (L1), is hardware based while the two subsequent levels, Level 2 (L2) and Event Filter (EF) are software based. The purpose of the trigger is to select the events of most interest from the very large number of

beam crossings most of which only produce soft QCD collisions.

The general design of the ATLAS trigger menu is based on general objects and combinations of objects that are useful to as many different analyses as possible. For example, large proportions of the available bandwidth is used for single electron and muon items which are used by many different analyses. Similarly $E_{\mathrm{T}}^{\mathrm{miss}}$ triggers and combined triggers requiring $E_{\mathrm{T}}^{\mathrm{miss}}$ and a single jet are useful for many analyses so are given significant bandwidth. For some objects the rate of production is too high to be feasibly recorded offline. This is due to a several computing constraints; for example the event size is $\sim$1.4 Mb such that recording data at very high rates is not feasible. For such items only a fraction of events that pass the trigger are recorded. This is known as a *pre-scaled* trigger. The lowest threshold for each item that does not need to be pre-scaled is known as the *lowest unpre-scaled trigger* and it is these that are used for most search analyses that wish to use the full delivered integrated luminosity.

The L1 hardware trigger operated in 2012 with an input rate of 40 MHz, with bunch crossings occuring at a maximum rate of 20 MHz, and an output rate of 70 kHz. This is then fed into L2 which reduced the rate to 5 kHz and this was then reduced to a 700 Hz output rate of the Event Filter. These rates are at the limit of the current data acquisition model. The 700 Hz of offline output could not all be immediately processed and therefore some proportion of this was stored offline for processing later, during the shutdown period.

4.6.1 $E_{\mathrm{T}}^{\mathrm{miss}}$ Trigger

During the period of my D.Phil I was involved in the $E_{\mathrm{T}}^{\mathrm{miss}}$ trigger group. My primary contribution was the writing of the software for an improved version of the Level 2 $E_{\mathrm{T}}^{\mathrm{miss}}$ trigger and the software to monitor this new trigger item. This was first implemented in the final stages of data taking in 2011 where it was tested *in-situ* and then ran as the primary $E_{\mathrm{T}}^{\mathrm{miss}}$ algorithm at L2 in 2012. I also participated in the design of the 2012 menu items based on $E_{\mathrm{T}}^{\mathrm{miss}}$ triggers.

The 2011 $E_{\mathrm{T}}^{\mathrm{miss}}$ Trigger

At Level 1 the $E_{\mathrm{T}}^{\mathrm{miss}}$ is formed using "trigger towers", which are coarse grained calorimeter elements where the energy in the x and y directions are summed, and these are then easily

combined by the hardware. A simple noise threshold of around 1 GeV was employed for each trigger tower to enter the computation in 2011. The large size of these trigger towers and the simplicity of the cuts against noise results in a reasonably large resolution at this level which can be improved on at the higher trigger levels.

In 2010 and 2011 the default algorithm at Level 2 was identical to that used at L1. Therefore no additional information was present at L2 and no additional rejection of unwanted events could be achieved.[4]

The Event Filter has more time allowed per event than at L2 allowing more complicated algorithms to be run. In 2011 the default algorithm at EF used the full ∼188,000 calorimeter cells. This was achieved by a large parallel computing system that accesses the information from the front-end readout systems. Noise cuts can then applied at a cell level. In 2011 these consisted of only including cells where $E > 3\sigma_{\text{cell}}$ where σ_{cell} is the cell noise distribution width. This one-sided approach was implemented to avoid large unphysical negative energy contributions.

Improvements implemented for 2012 running

By the end of 2011 the limiting factor in the rate of the $E_{\text{T}}^{\text{miss}}$ trigger was the input rate into the Event Filter (being the same as the output rate from L1). The L1 resolution also dominated the correspondence between online triggered events and the offline efficiency. The rate for all the $E_{\text{T}}^{\text{miss}}$ triggers together into the Event Filter would have to be much less than 1 kHz in 2012 (target rates were $\sim 400\,\text{Hz}$). Extrapolation of the L1 rates to 2012 operating conditions showed that the threshold would need to be raised considerably to achieve this. The L1 noise thresholds were tightened to reflect the 2012 operating conditions, however, this was insufficient to reduce the rate to allow the L1 thresholds to remain low.

It was therefore desirable to improve the L2 algorithm, which can cope with a higher input rate, to increase the rejection such that low L1 thresholds could be maintained. This was made possible by changing the way that the data flowed through the system. The electronic front-end readout boards on the detector were adapted to take the energy of up to 128 cells

[4]At L1 there are a limited number of items that can be present in the menu so some additional flexibility is added by the inclusion of this algorithm at L2.

and then apply the noise cuts like those present in the 2011 EF algorithm and then pass this summary information to the trigger farm. This allows L2 to use the full granularity of the detector and greatly improves the resolution. Small differences in the L2 and EF computations remain due to the information being rounded down to the nearest 64 MeV for each front-end board, and other smaller effects (eg. lack of tile quality information and approximations for the η positions of some regions). This algorithm was tested online at the end of 2011. Figure 4.10 shows the improvement in the resolution measured with respect to the more accurate EF calibration on events triggered using an electron trigger. Also the efficiency with respect to offline $E_{\mathrm{T}}^{\mathrm{miss}}$ is improved as is demonstrated in Figure 4.11 where the trigger efficiency for the same cut value is shown for the new L2 algorithm and the L1 algorithm. This improvement increases the rejection at L2, and in 2012 the item requiring $E_{\mathrm{T}}^{\mathrm{miss}}$>40 GeV at L1 could record almost all of the 2012 data unprescaled[5], which was the same highest unprescaled item as in 2011. This improved algorithm ran as the default algorithm for all missing energy trigger items in 2012 and in Figure 4.12(a) the improvement is demonstrated using early 2012 data. For the monitoring of this trigger the time taken for this algorithm to be completed means that running it on every event at L2, rather than only those seeding $E_{\mathrm{T}}^{\mathrm{miss}}$ chains, would use too many resources. Instead the same algorithm is run at EF for all events passing any L2 trigger allowing the online result to be available for all events recorded.

At EF improvements were also made allowing topoclusters to be formed using the same criteria as offline instead of using cell level information. This then uses the local cluster calibration [87] so distinction is made between electromagnetic and hadronic objects. This yields more similar results to the full offline calibration than the cell based algorithm. This improvement is shown in Figure 4.12(b).

The result of these modifications to all three different trigger levels is that the lowest unprescaled trigger in 2012 has offline thresholds which are similar to those which were available in 2011 despite the increased operating energy and number of collisions per crossing. A definitive statement to this effect is not possible as the efficiency of the $E_{\mathrm{T}}^{\mathrm{miss}}$ trigger is dependent on the

[5]For most of the year it remained unprescaled, although in some periods the first three bunches of each bunch train were excluded. This choice of excluding the first three bunch crossings is due to the fact that in these bunches the lack of previous interactions means that the effect of out-of-time collisions is not compensated for as efficiently leading to larger noise contributions in these bunches.

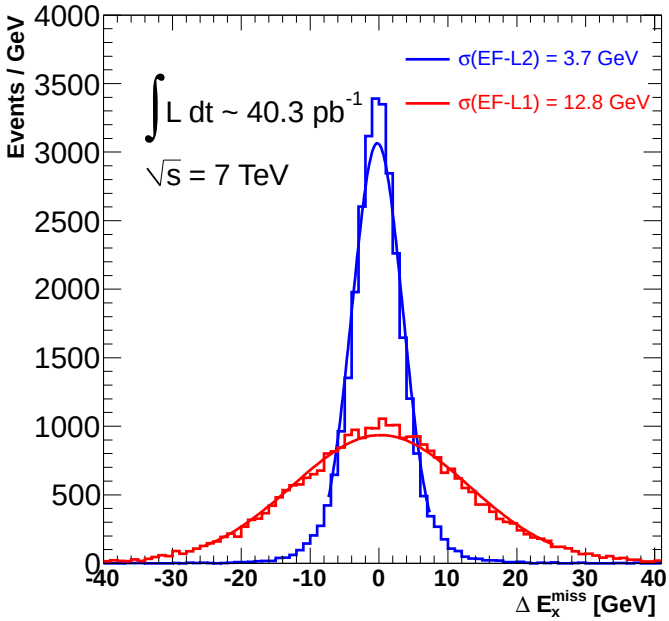

Figure 4.10: The improvement in the resolution due to the changes implemented at Level 2. The resolution is measured with respect to the more accurate Event Filter cell based algorithm. Data were recorded in the last run of 2011 and was triggered on using a single electron trigger. A significant improvement in the resolution is observed. A simple Gaussian is used to demonstrate the level of improvement.

topology of the events considered. These triggers, and combined jet and $E_{\mathrm{T}}^{\mathrm{miss}}$ triggers, are used by many of the ATLAS supersymmetry searches, for example the search with 2-6 jets, $E_{\mathrm{T}}^{\mathrm{miss}}$ and no isolated electrons or muons used a jet and $E_{\mathrm{T}}^{\mathrm{miss}}$ combined trigger [88].

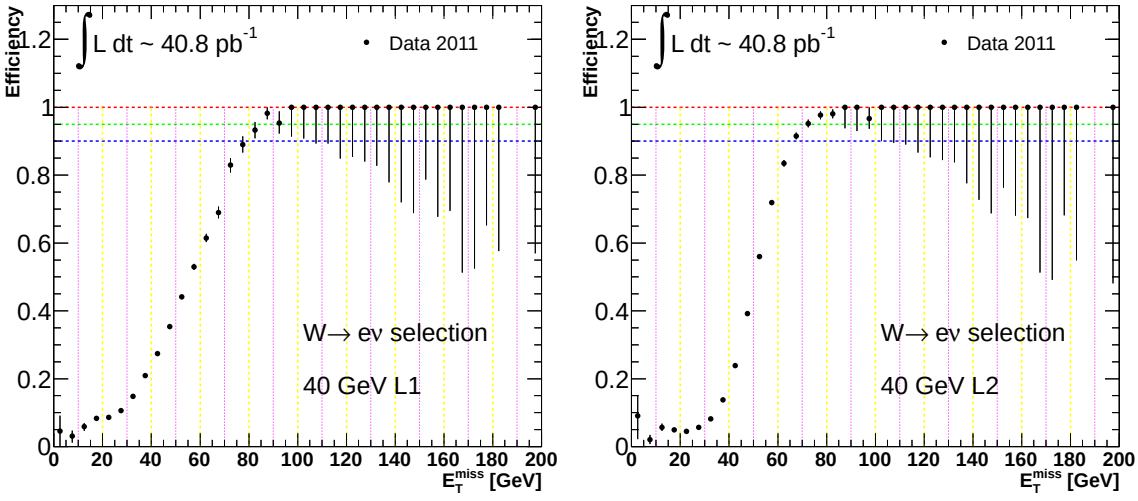

Figure 4.11: The efficiency of the L1 (left) and improved L2 (right) algorithms with respect to offline $E_{\mathrm{T}}^{\mathrm{miss}}$ formed from topological clusters at the electromagnetic scale for events passing a $W \to e\nu$ selection. A clear improvement in the efficiency is demonstrated.

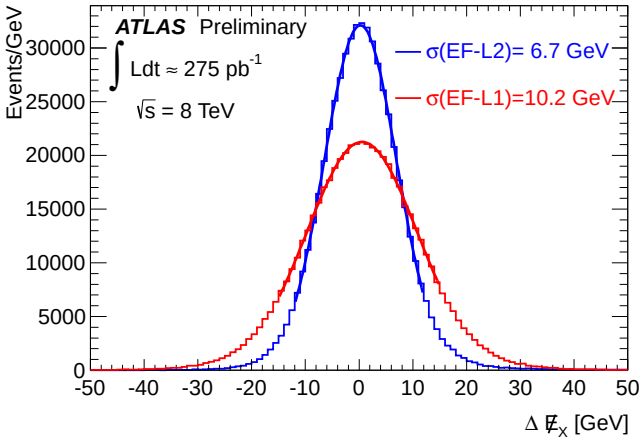

(a)

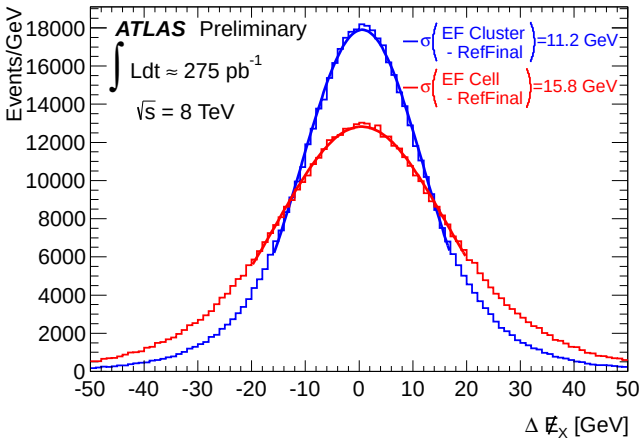

(b)

Figure 4.12: Improvements to the L2 (a) and EF (b) from the various improvements to the two different algorithms. The L2 improvements are compared to the resolution at EF, while the improvements at EF are measured relative to the offline computation. Both distributions have been produced using early 2012 data. (a) is equivalent to 4.10 with 2012 data. *(These figures were created by another member of the collaboration.)*

Chapter 5

Monte-Carlo Simulation

Monte-Carlo simulations are used to aid in the determination of the Standard Model backgrounds as well as in the simulation of signal models. The area of phase space that is probed by this search is particularly difficult to simulate (at leading order this is primarily due to CPU processing times rather than theoretical constraints). The best available generators are used to gain the most precise predictions possible. For high jet multiplicity final states these are leading order (LO) multi-leg generators interfaced with parton showers. Next-to-leading order (NLO) calculations interfaced with parton showers using the `PowHeg` [89] or `MC@NLO` [90] methods only have a single real emission in the calculation and rely on the parton shower to provide additional splittings such that these are less accurate at high jet multiplicity. NLO calculations of multi-parton final states are possible [91, 92, 93], however, interfacing these calculations with parton showers is still an active area of research [94, 95].[1]

5.1 Leading Order Generators and Parton Showers

Monte-Carlo generators consist of several parts. The long distance interactions are captured by the *parton density functions* which are non-perturbative and while the evolution of the functions comes from theory, experiment is relied upon to provide the inputs. A matrix element

[1] For the W+jets and Z+jets backgrounds to this search the `SHERPA` Monte-Carlo uses the `MENLOPS` procedure [96, 97]. This combines a NLO calculation of the inclusive process with leading order calculations for the higher multiplicities using an adapted version of the `PowHeg` formalism [89]. As we are most interested in the highest multiplicities where the calculation is at LO the details of how this is done are not described here.

calculation is used to calculate the hard core process at leading order in α_S and a *parton shower* is used to generate additional initial and final state radiation down to a soft scale when hadronisation is then performed. Finally the *underlying event* consisting of soft emission and the remnant of the colliding hadron is also simulated. Out of these components those that are most important for multi-jet final states are the matrix element calculation and the parton shower.

For a physical simulation of a hadronic jet it is necessary to "dress" partons from the final state of the hard process such that there can be an arbitrarily large number of branchings. This is the task of the parton shower. Considering a single additional emission in the colinear (or soft) limit, the matrix element can be factorised into the hard process and a co-linear splitting term. Note that this is not the case for hard emissions. This makes the showering of partons universal between different physical processes. A second branching which is softer than the first can also be factorised out, along with further subsequent softer and softer emissions. However, it should be noted that no interference terms between different initial partons is considered (yet) as they are independently showered. This simple model is implemented through the use of *Sudakov Form Factors*, $\Delta(Q^2, t)$ which are defined by the probability that no branching occurs between two scales, Q^2 and t, for a particle. Using the *Sudakov Form Factors* and the probability of a splitting occuring, $dp(t_i)$, the parton shower can be evolved down through any number of splittings to a low scale, Q_0^2 ($\sim 1\,\mathrm{GeV}$) where hadronisation is deemed to start to occur. For example the probabilities of 0, 1 and 2 branchings at scales t_1 and t_2 would be given by:

$$\begin{aligned} dP_0 &= \Delta(Q^2, Q_0^2) \\ dP_1(t_1) &= \Delta(Q^2, t_1) dP(t_1) \Delta(t_1, Q_0^2) \\ dP_2(t_1, t_2) &= \Delta(Q^2, t_1) dP(t_1) \Delta(t_1, t_2) dP(t_2) \Delta(t_2, Q_0^2) \Theta(t_1 - t_2). \end{aligned}$$

This is, in general, how Monte-Carlo programs shower hard partons by randomly generating events with various numbers of branchings weighted by their probability. To get the soft emission limit correct the parameter t that the branchings are ordered under should be proportional

to the angle of emission. This means that emissions only take place within a cone around each parton which partially takes into account interference effects between different partons, however, there will also be dead areas in the phase space.[2] As the LHC is a hadron collider initial state radiation is also important and this is handled in a very similar way; starting at the hard process and evolving backwards in time emitting partons at widest angles first down to the final scale that is the splitting scale of the initial parton density function.

From this description it is clear that while parton showers can be tuned to data such that at large angles they give reasonable descriptions of experimental data it is undesirable to rely on them for hard jet emission which is what we are interested in. The solution to this problem is to merge matrix element calculations with several hard partons in the final state with a parton shower model.

5.2 Multi-leg Generators and Matching Schemes

Matrix element calculations at leading order can be computed for a large number of additional partons and fully take into account interferance effects, fill all of phase space correctly and are valid when the partons involved are hard and well separated, such that we are in the perturbative regime. This is obviously complementary to the parton shower which is valid in the soft and co-linear reigme such that it is desirable to interface the two approaches. "Matching Schemes" describe methods of combining the approaches. Care needs to be taken that processes are not double counted in the method and that the more accurate calculation is used for the different parts of the process.

The MLM Matching Scheme

The MLM matching scheme [98, 99] proceeds by defining a minimum E_{T} threshold, $E_{\mathrm{T}}^{\mathrm{min}}$, for partons in the hard matrix element and also a minimum hard separation between them $\Delta R_{jj} > \Delta R_{\mathrm{min}}$. Events are then showered without any specific hard emission veto. A jet cone algorithm, using the same ΔR_{min} and $E_{\mathrm{T}}^{\mathrm{min}}$, is applied to the showered event. Starting

[2]Some generators allow the user to relax this condition leading to "power shower" emission where the whole phase space will be populated, however, in this case the parton shower is being used far from the soft and co-linear limit where it is valid so should be used with care.

with the hardest matrix element parton it is then tested whether there is a jet within ΔR_{min} of that parton then it is considered matched, the jet is removed from the event and the next parton is tested. If any parton is not matched to a jet then the event is rejected. If any jets remain after this matching process then the event is rejected unless it originated from the highest jet multiplicity that is computed at the matrix level. This procedure results in both the removal of events where a hard jet is created by the parton shower which could be more accurately computed by using a higher parton multiplicity matrix element and also events where two partons from the matrix element form a single jet such that the matrix element with one less parton should be used accompanied by the parton shower. This method also removes the possibility of double counting regions of phase space between the different matrix element samples and uses the most appropriate calculation for the different parts of the calculation.

The CKKW Matching Scheme

The CKKW matching scheme [100, 101] is more complicated than the MLM procedure but maintains full LO accuracy for the hard matrix element and also the full next-to-leading-logarithm (NLL) accuracy of the parton shower, with the dependence on the matching parameter scale cancelling at NLL accuracy.

- For matching, it uses the relative transverse momenta measure, $k_\perp$:

$$\left(k_\perp^{(ij)}\right)^2 = 2\text{min}\left(p_{\text{T}}^{(i)}, p_{\text{T}}^{(j)}\right)^2 \frac{\left[\cosh(\eta^{(i)} - \eta^{(j)}) - \cos(\phi^{(i)} - \phi^{(j)})\right]}{D^2}.$$

  Particles are defined to be in different jets if $k_\perp^{(ij)} > k_\perp^0$ and also each jet is required to have transverse momentum greater than the matching scale, $k_\perp^0$.

- Matrix element cross-sections are modified by re-weighting factors based on the *Sudakov form factors* and the different scales in α_S to account for the probability of additional radiation.

- The parton shower then uses the scale at which the given parton was produced as its starting scale and the algorithm used is constructed such that no unwanted additional raditation is produced.

These steps ensure that there is no double counting between matrix elements of different multiplicity and also that in the different regimes the appropriate calculation is used. Initial probabilities for each different multiplicity matrix element are defined by their relative cross-sections where the partons are required to satisfy the separate jet criteria of the $k_\perp$ scheme. For a given event a jet reconstruction algorithm based on the $k_\perp$ distance parameter is then used to recluster partons, also ensuring that the colour combination rules are obeyed, back to a 2→2 process. This gives a possible history of the event and using this history the *Sudakov form factors* are computed and applied to weight the event on the probability of no emission above the matching scale during this evolution. Also using this history the strong couplings constants, $\alpha_S(Q^2)$, are evaluated at the various vertex splittings and these are also used to reweight the events.

After re-weighting, the parton shower is applied with the starting scale set to the final splitting of that parton from the reconstructed possible history. For all events, apart from those of the highest matrix element order computed, a veto on the parton shower is applied such that no additional radiation above the matching scale is allowed. For the highest multiplicity matrix elements the veto is relaxed to the scale of the softest clustering in the event such that the parton shower can provide additional jets beyond the number that can be calculated in the matrix element.

Implementation

In this analysis `SHERPA` Monte-Carlo [102] is used as the baseline generator. This implements an extended version of the CKKW matching scheme[3] [103] in its leading order matrix element + parton shower processes. The shower implemented in `SHERPA` [104] is based on Catani-Seymour dipole factorisation [105]. $t\bar{t}$ samples are generated with up to 4 additional partons in the matrix element calculation. The matching scale is set to 30 GeV. As the top quarks can decay to up to 5 jets (including a hadronic tau) and $E_{\mathrm{T}}^{\mathrm{miss}}$ before adding additional partons, the Monte-Carlo should not have to rely on the parton shower for signal regions with up to 9 jets – the highest multiplicity we probe. For W+jets and Z+jets samples are generated with up to

[3] A different distance criteria is used and truncated showers are applied to intermediate partons, however the principles remain the same.

5 additional partons in the matrix element with a 20 GeV matching scale. Further jets rely on the parton shower. Data are used to validate how well the parton shower manages to generate these extra jets and large uncertainties are associated with these processes.

For signal samples `HERWIG++` [106] is used which does not implement a multi-leg matrix element approach, however as the signal models used for interpretation have a very large number of jets in the decay chain of the core process we are not relying on the parton shower to produce many additional jets.

5.3 GEANT4 Detector Simulation

Particles with lifetimes $> 10\,\text{mm}$ are treated as stable by the generator. Following hadronisation and decays such that all the remaining particles are stable with respect to this definition the event is passed to the ATLAS detector simulation [107]. This uses GEANT4 software [108]. Following simulation of the hard interaction additional minimum bias collisions are added to simulate the multiple interactions per beam crossing. Reconstruction of the events after digitisation of the hits in the detector uses the same software as that applied to data.

Chapter 6

LHC Searches in the Fully Hadronic Channel for SUSY Particles

While both ATLAS and CMS have searched for supersymmetry in many different final states here I will describe in detail only the ATLAS searches which are in the fully hadronic state and require $E_{\mathrm{T}}^{\mathrm{miss}}$. Typically in the most generic models of supersymmetry such as MSUGRA/CMSSM these analyses which veto high p_{T} leptons and require jets and $E_{\mathrm{T}}^{\mathrm{miss}}$ (hereafter referred to as 0-lepton) are the most powerful.

With data taken in 2010 at 7 TeV corresponding to an integrated luminosity of 35 pb^{-1} a search was performed in the 0-lepton channel [4] cutting on the discriminating values outlined in the documentation produced before the start up of the LHC [109]. The primary discriminating variable was m_{eff}^{n} which is the scalar sum of the $E_{\mathrm{T}}^{\mathrm{miss}}$ and the p_{T} of the leading n jets, and in addition the signal regions required either ≥ 2 or ≥ 3 hadronic jets. Cuts on $E_{\mathrm{T}}^{\mathrm{miss}}$, the minimum azimuthal angle between the $\vec{E}_{\mathrm{T}}^{\mathrm{miss}}$ and any hadronic jets and the ratio $E_{\mathrm{T}}^{\mathrm{miss}}/m_{\mathrm{eff}}^{n}$ were used to reduce the background from jet mis-measurement to a negligible level. No significant deviations from the expected number of SM events were observed and limits were set in the MSUGRA/CMSSM model. These are shown in Figure 6.1(a). From the figure it is clear that even with this relatively small amount of data the limits from the LHC far exceed those from the Tevatron due to the increased centre of mass energy.

In 2011 the luminosity rapidly increased and the 2010 search was updated (and improved)

regularly [5, 6, 110]. The same approach as in 2010 was employed cutting to remove mis-measurement backgrounds and making a final cut on m_{eff}^{n}. As the amount of recorded integrated luminosity increased more of the phase space was probed and the signal regions were tightened requiring higher values of m_{eff}^{n} and larger numbers of jets. The evolution of the limits (as no significant excesses were observed) is shown in Figures 6.1(b)-6.1(d). The limit in each case is taken from the signal region with the best expected sensitivity in that area of phase space from a selection of signal regions with different requirements on m_{eff}^{n} and jet multiplicity. At low m_0 the limit comes from requiring ≥ 2 jets, whereas at large values of m_0 it is dominated by the largest jet multiplicity cut used ≥ 6 jets. The background estimations of the dominant backgrounds of $t\bar{t}$, W+jets and Z+jets come from a partially data-driven method where a Monte-Carlo prediction is normalised in a region of phase space close to that of the signal region but with low amounts of expected signal contamination. For example the $t\bar{t}$ and W+jets backgrounds are normalised in regions requiring a hard lepton, the transverse mass, m_{T},[1] near the W mass and with other cuts similar to those of the signal region. This minimises the dependence on the Monte-Carlo simulations that are at fixed order and also detector related uncertainties cancel in this normalisation. The analysis has also been updated with data taken in 2012 at $\sqrt{s} = 8\,\text{TeV}$ [88]. No significant excess was observed and the limits covered more of the parameter space (see Figure 6.1(e)).

It was pointed out both within the collaboration and in the literature (eg. [111]) that if additional steps are present in the decay of strongly produced pairs of supersymmetric particles then the amount of $E_{\text{T}}^{\text{miss}}$ present in the event will be reduced and there will be large jet multiplicity. Such models are also theoretically well motivated [112]. Therefore a new search strategy was pioneered by the author to target this final state. The strategy behind this analysis is given in detail in the following chapter where the latest incarnation of this analysis is discussed in detail. New analysis techniques had to be developed to deal with a large component of the background now coming from mis-measured jets. The first results of this new analysis were published with 1.34 fb^{-1} of 7 TeV data [2]. This was then updated with the full 2011 dataset [3]. The limits set by this new analysis in the MSUGRA/CMSSM plane are shown in Figure

[1] m_{T} is defined using the $E_{\text{T}}^{\text{miss}}$, the p_{T} of the lepton, p_{T}^{l}, and the azimuthal angle between the $E_{\text{T}}^{\text{miss}}$ and the lepton, ϕ_l, by; $m_{\text{T}} = \sqrt{2E_{\text{T}}^{\text{miss}} p_{\text{T}}^{l}(1 - \cos(\phi_l))}$.

6.2.

Figure 6.3 shows a comparison of the ATLAS searches for strongly produced SUSY particles with the full 2011 dataset in the MSUGRA/CMSSM plane. Competitive searches were performed in final states with 0-leptons and $\geq 2-4$ jets [110], 1-2 leptons and $\geq 2-4$ jets [113], 1-lepton and ≥ 7 jets [114] and the multi-jet 0-lepton final state [3]. It is clear from the expected limit curves that at low values of m_0 the low jet multiplicity 0-lepton search is the most sensitive while at high values of m_0 the 0-lepton multi-jet analysis is the most powerful.

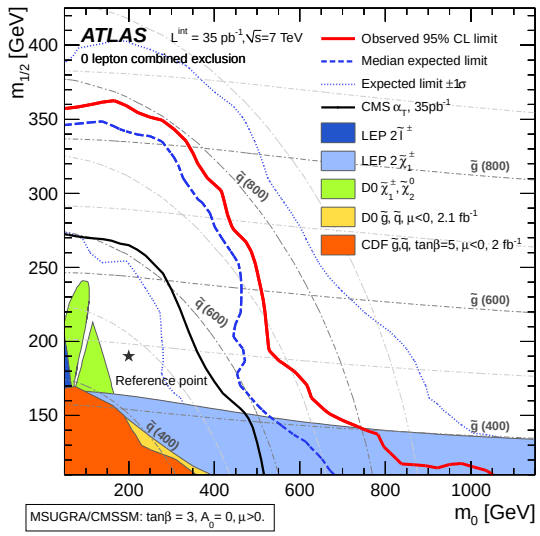

(a) 0-lepton limits with 35pb^{-1} of 7 TeV data.

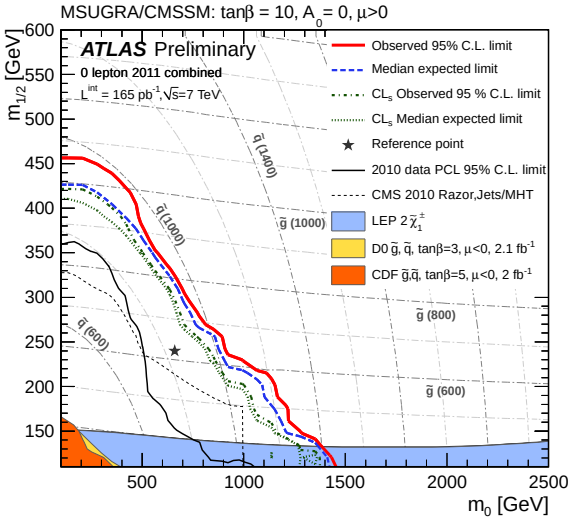

(b) 0-lepton limits with 165pb^{-1} of 7 TeV data.

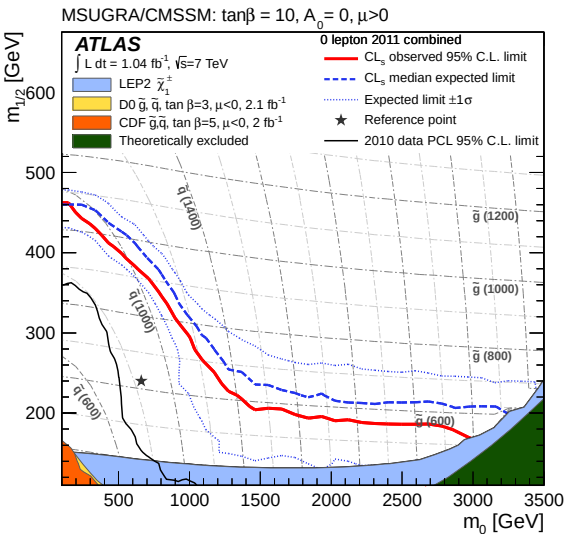

(c) 0-lepton limits with 1fb^{-1} of 7 TeV data.

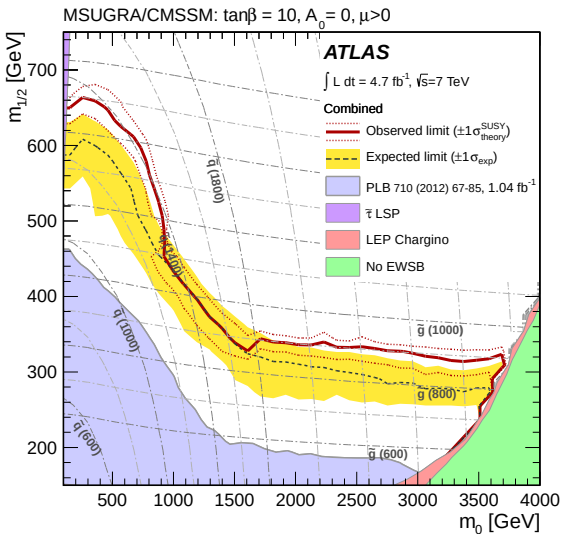

(d) 0-lepton limits with 4.7fb^{-1} of 7 TeV data.

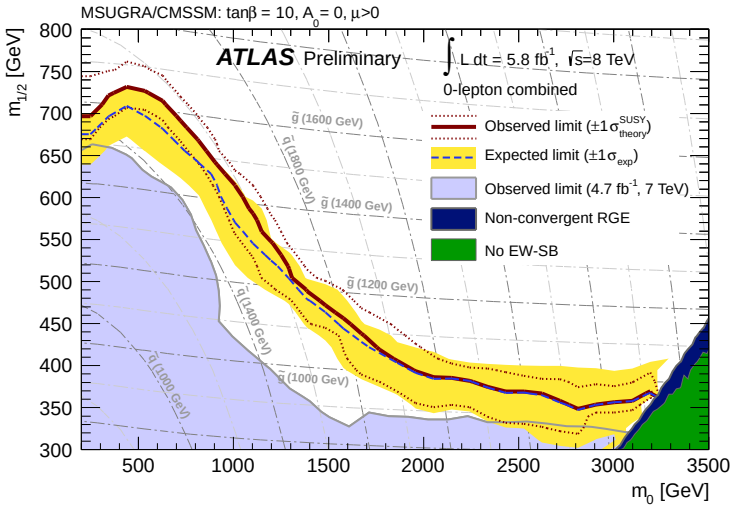

(e) 0-lepton limits with 5.8fb^{-1} of 8 TeV data.

Figure 6.1: Limits set by the ATLAS 0-lepton analyses requiring ≥ 2 to ≥ 6 jets in 2010 (a)[4], 2011 (b)-(d)[5, 6, 110] and 2012 (e)[88]. Note the different scales on the axes of the plots.

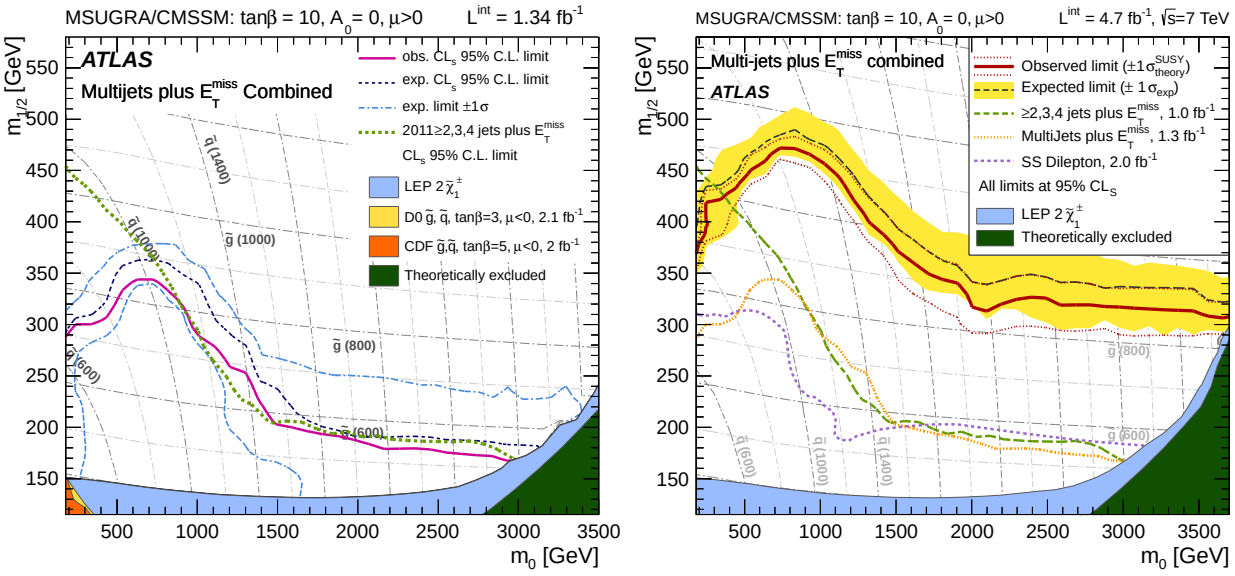

(a) Multi-jet limits with 1.34 fb^{-1} of 7 TeV data [2]. (b) Multi-jet limits with 4.7 fb^{-1} of 7 TeV data [3].

Figure 6.2: Limits set by the ATLAS 0-lepton high jet multiplicity analyses in 2011.

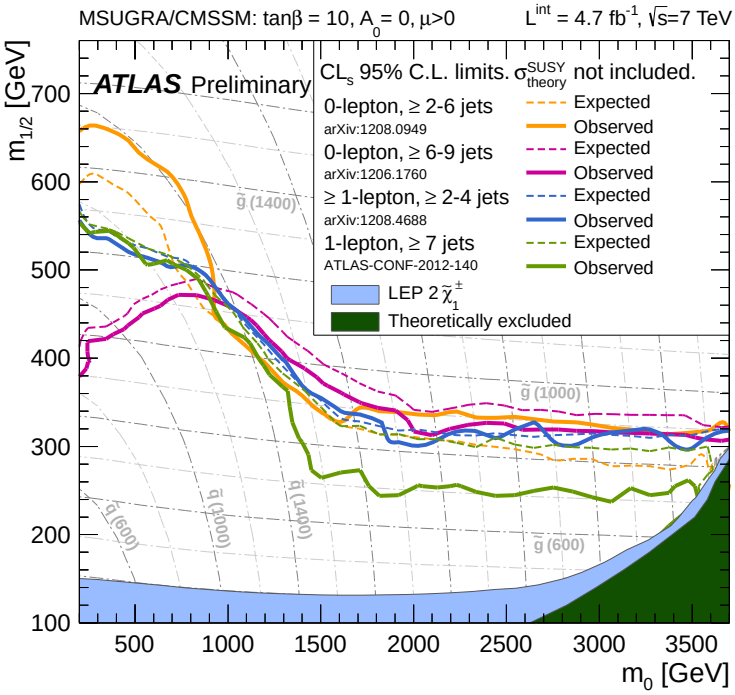

Figure 6.3: A comparison of the expected and observed limits using the full 2011 dataset of the 0-lepton analysis, multi-jet analysis and leptonic analysis. At large values of m_0 it is seen that the multi-jet analysis is the most powerful. Figure from [114].

Chapter 7

5.8 fb^{-1} 8 TeV Search for SUSY Requiring High Jet Multiplicity

7.1 Introduction

As it was explained in the previous section, with the lack of discrepancy from the Standard Model expectation in the early SUSY searches, it was desired to explore areas of parameter space that were harder to probe. One such area comes from the case where there is a longer decay chain (or a decay chain through more massive Standard Model particles) such that more of the energy is contained in the visible sector compared to the $E_{\mathrm{T}}^{\mathrm{miss}}$. These final states will have large numbers of jets and this becomes one of the most powerful discriminating variables. A new analysis was designed to target this final state. Here we describe in detail the latest version but the arguments for the basis of the selection are the same as those used to motivate the first version of the analysis [2].

The target is models with $E_{\mathrm{T}}^{\mathrm{miss}}$ and large numbers of jets so the primary backgrounds will be $t\bar{t}$ and W+jets, each contributing when the lepton does not pass the criteria to be vetoed, $Z \to \nu\nu$+jets, and a multi-jet background where the $E_{\mathrm{T}}^{\mathrm{miss}}$ primarily originates from jet mis-measurement. The selection of high jet multiplicity leads to a difficult final state for accurate Monte-Carlo simulation so data-driven normalisation at large jet multiplicity is necessary to give confidence in the predictions of the $t\bar{t}$, W+jets and $Z \to \nu\nu$+jets backgrounds. As the

$E_{\mathrm{T}}^{\mathrm{miss}}$ cuts cannot be as hard as in previous SUSY searches, the fraction of the total background from multi-jet processes will be larger which leads to new experimental challenges.

The description of the analysis begins with the methods of reconstruction of the offline objects: jets, electrons, muons and missing transverse energy (§7.2). This is then followed by a description of the triggers employed to record the data as these influence the selection of events (§7.3). The Monte-Carlo simulated samples used to aid in the background determination and signal interpretation are described (§7.4). Another concern is the multiple interactions that happen each crossing in high luminosity hadron colliders. These effects are described next as these can also influence the analysis selection (§7.5). A pre-selection designed to remove non-collision and detector related effects is employed (§7.6) before the selection for the analysis signal and control regions described in §7.7 is applied. The background estimation is split into two sections: the backgrounds dominated by jet-mismeasurement (§7.8.1) and those where the $E_{\mathrm{T}}^{\mathrm{miss}}$ originates from prompt leptons (referred to as the "leptonic" backgrounds) (§7.8.2). The results in the signal region are given in §7.9 and are also interpreted in two planes of supersymmetric phase space.

7.2 Object Definitions

Jets: Jets are formed using the anti-k_t algorithm [115] from inputs that are topological clusters of calorimeter cells [83] which are calibrated using the local cluster weighting method [87, 86]. A correction parametrised by the number of reconstructed primary vertices, the average number of interactions per crossing and the jet η is applied to correct for the mean expected contributions to the jet energy from other collisions from the same and previous bunch crossings [85]. Subsequently a correction to the jet direction is performed such that it points at the hard scatter vertex and the 4-vector is corrected (in both energy and η) such that the jet is calibrated to the particle level [86]. Finally a small residual correction is applied to data only based on in-situ measurements [84]. Jet candidates are required to have $p_{\mathrm{T}} > 20\,\mathrm{GeV}$ and $|\eta| < 2.8$ apart from when they are used in the computation of the missing transverse energy. For the evaluation of systematic uncertainties an algorithm based on the impact parameter and secondary vertex information is used to tag jets initiated by b quarks. The algorithm used is

the output of a neural network which takes as inputs the weights of three other algorithms: `JetFitter+IP3D`, `IP3D` and `SV1` [116]. A working point is chosen which selects 70% of b-jets, with mistag rates of ∼20% for c-jets and $\sim 1\%$ for light quark and gluon jets.

Electrons: Candidates are reconstructed from clusters of cells in the electromagnetic calorimeter matched to a track in the ID. They are required to have $p_{\mathrm{T}} > 20$ GeV and $|\eta| < 2.47$, and to satisfy the "medium" electron shower shape and track selection criteria of Ref. [117], with modifications to reduce the impact of pile-up and cope with tighter trigger requirements induced by the higher instantaneous luminosity. Electrons are accepted if $E_{\mathrm{T}} > 20$ GeV and $|\eta| < 2.47$ where $E_{\mathrm{T}} = E^{\mathrm{clust}}/\cosh\eta$, E^{clust} is the energy of the cluster, and η is taken to be that measured with the tracker, η^{track}, if the track contains at least four hits in the silicon layers of the ID and that measured by the calorimeter cluster, η^{clust}, otherwise. For control region selections requiring electrons, tighter shower-shape and track criteria are applied [117] and additionally they are required to be well isolated such that the $\sum p_{\mathrm{T}}$(tracks) in a cone of radius [1] $\Delta R < 0.2$ must be less than 10% of the electron's p_{T}.

Muons: Candidates are formed by matching reconstructed tracks in the inner detector with either complete or partial tracks reconstructed in the muon spectrometer [118], with the requirement that they satisfy $p_{\mathrm{T}} > 10$ GeV and $|\eta| < 2.4$. Again, for control region selections an additional isolation requirement is made. The $\sum p_{\mathrm{T}}$(tracks) in a cone of radius $\Delta R < 0.2$ around the muon must be less than 1.8 GeV.

Overlap of objects: When jets are formed all clusters of calorimeter cells are considered. The result of this is that electrons will also additionally be reconstructed as jets. Also, there will be electrons and muons inside jets from heavy flavour decays which we do not wish to enter at the analysis level. Therefore a removal procedure is applied to resolve these overlaps. Firstly, if an electron candidate is found to lie within $\Delta R < 0.2$ of a jet then the jet candidate is removed as it is interpreted as an electron. Next, if a muon is found within $\Delta R < 0.4$ of a jet then the muon is ignored at the analysis level. Finally, if an electron is found within

[1] $\Delta R = \sqrt{(\Delta\eta)^2 + (\Delta\phi)^2}$

$0.2 < \Delta R < 0.4$ of a jet then the electron candidate is ignored.

Missing Transverse Energy: This is formed from the negative vector sum of all the jet, electron and muon candidates as well as all jet candidates with $p_{\mathrm{T}} > 7\,\mathrm{GeV}$ and $|\eta| < 4.5$ and all clusters of calorimeter cells which are not associated to such objects. Overlap between the different objects (jets, electrons and muons) is resolved at the level of calorimeter clusters with electrons taking top priority, then jets and finally calorimeter deposits from muons. The objects are calibrated using the full calibration associated with such objects and the resolution of the energy present in clusters not associated with objects is improved using tracking by using the tracks of particles that are too soft to reach the calorimeter and for calorimeter clusters with associated tracks the track momentum is used to improve resolution.[2]

7.3 Triggers and Data Sample

It is an obvious criterion for any analysis that a suitable trigger is required to record the data used. Multi-jet triggers are used for this analysis. A six jet trigger is used for the 55 GeV jet p_{T} signal regions and a five jet trigger is used for the signal regions which count 80 GeV jets. At Level 1 and Level 2, looser requirements are made on the numbers of jets so as to mitigate jet merging/splitting between the different algorithms that are used at the different levels. Using data recorded by muon triggers the efficiency of the triggers can be measured. Figure 7.1 shows the cumulative efficiency for the triggers used in the analysis for two different offline calibration schemes. In this analysis the local cluster weighting calibration scheme is used (LCTopo:- blue points). The triggers are $> 98\%$ efficient for forming the control regions with 6 or 5 jets for the 55 GeV and 80 GeV jet cuts respectively and are $\sim 100\%$ efficient for all signal region selections.

[2]There are some small differences between the $E_{\mathrm{T}}^{\mathrm{miss}}$ computation used in the analysis and that used in 2011 [119] and 2010 [120] performance studies due to, for example, improvements in the treatment of clusters of cells not associated with objects, however, the principles of the computation is the same.

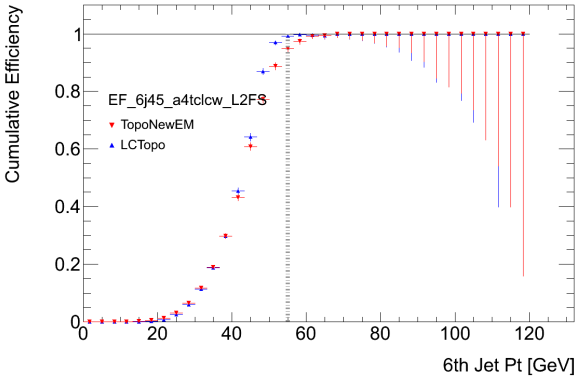

(a) 6-jet trigger efficiency as a function of 6th jet p_{T}.

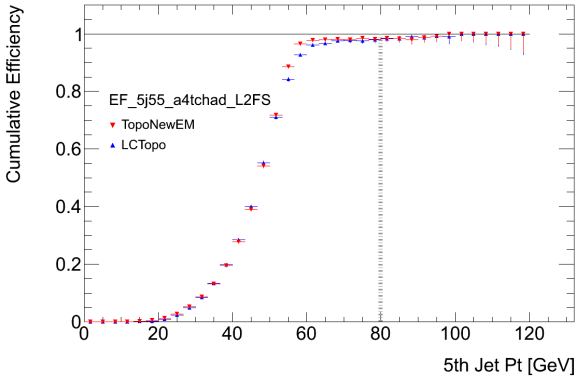

(b) 5-jet trigger efficiency as a function of 5th jet p_{T}.

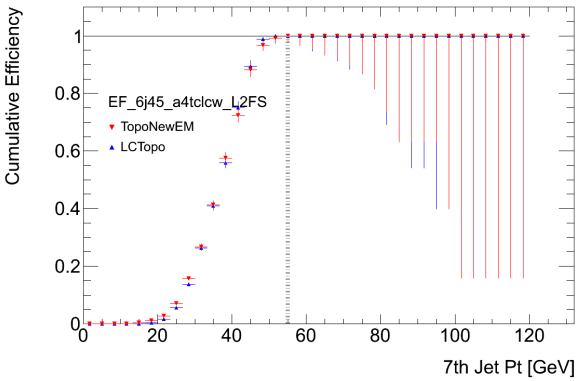

(c) 6-jet trigger efficiency as a function of 7th jet p_{T}.

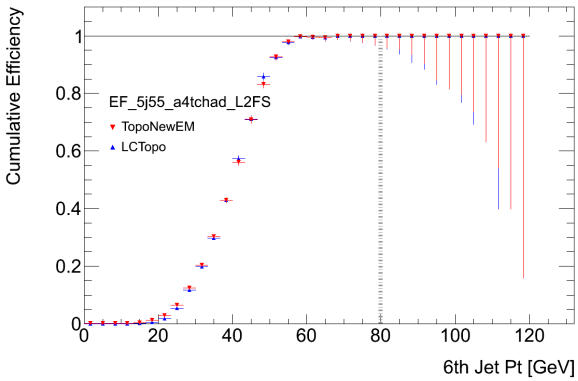

(d) 5-jet trigger efficiency as a function of 6th jet p_{T}.

Figure 7.1: The cumulative efficiency of the 6-jet and 5-jet trigger as a function of the 6th jet (a) and 5th jet p_{T} (b) respectively. As all the signal regions require an additional jet offline compared with the trigger requirement (c) and (d) show the 6-jet trigger efficiency as a function of the 7th jet p_{T} and the 5-jet trigger efficiency as a function of the 6th jet p_{T}. The data shown are triggered by a muon trigger. Two separate offline jet calibration schemes are shown and the one used in this analysis is that corresponding to the blue points. *(Figures were produced by another member of the analysis team.)*

7.3.1 Data Sample

The data sample used for this search was recorded between March and June 2012 with centre of mass operating energy of $\sqrt{s} = 8\,\text{TeV}$. During this period the bunch separation was 50 ns and the mean number of interactions per crossing, μ, reached as high as 32. The effect of the additional interactions from the same crossing is referred to as *in-time pile-up* and the detector effects due to residual offsets from previous collisions is *out-of-time pile-up*. Simulation of these effects is included in the Monte-Carlo samples used. However, due to the difficulty in their modelling it is desirable in the analysis to avoid large dependence on their accurate simulation.

7.4 Monte-Carlo Samples

Monte-Carlo simulation samples are used to aid in the determination of the Standard Model background to this search and also to simulate signals for both optimisation and limit setting. The physics behind the choices of generator for the primary backgrounds is described in a previous section (§5) such that here parameter choices and generators are simply listed.

The $t\bar{t}$, W+jets and Z+jets backgrounds are the most important of the SM backgrounds that uses simulated samples. `SHERPA 1.4.0` [121] is used with the `CT10` PDF set [122]. The $t\bar{t}$ samples contain up to four additional partons in the matrix element with a CKKW matching scale of 30 GeV and the W+jets and Z+jets samples have up to five additional partons in the matrix element with a CKKW matching scale of 20 GeV. In all cases additional jets can be generated through the parton shower. The `SHERPA` generator also provides the parton showering as well as the fragmentation and hadronisation. The samples are all normalised to their theoretical cross-sections [123].

For comparison with the leading order multi-leg baseline samples, $t\bar{t}$ samples with NLO calculations interfaced with parton showers have been simulated using `MC@NLO 4.03` [90, 124] and `PowHeg` [89]. In both samples showering is provided by `HERWIG` [125] with the AUET2 tune [126] and the underlying event is simulated using `JIMMY` [127]. The `CT10` PDF set is used in both cases.

Two different signal models are considered: a simplified model of gluino pair produc-

tion followed by their decay, $\tilde{g} \rightarrow t + \bar{t} + \tilde{\chi}_1^0$ (through an off-shell stop), and a plane of MSUGRA/CMSSM space. For the MSUGRA/CMSSM plane we fix $\tan\beta = 10$, $A_0 = 0$ and $\mu > 0$ and plot m_0 against m_{12} as it is these parameters that give the strongest dependence on the masses of the supersymmetric particles which determines the cross-section. The mass spectra and decays are calculated using `SUSY-HIT` [78] interfaced with `SOFTSUSY` [77] and `SDECAY` [128]. `Herwig++ 2.5.2` [106] is used in both cases to simulate the events. Signal cross-sections are computed for the different production processes and are calculated to next-to-leading order in the strong coupling constant α_S, including the resummation of soft gluon emission at next-to-leading-logarithmic accuracy (NLO+NLL) [129, 130].[3] An envelope of cross-section predictions is defined using the 68% confidence-level (CL) ranges of the `CTEQ6.6` [131] (including the α_S uncertainty) and `MSTW2008` [132] PDF sets, together with independent variations of the factorisation and renormalisation scales by factors of two or one half. The nominal cross-section value is then taken to be the midpoint of the envelope, and the uncertainty assigned is half the full width of the envelope, following closely the PDF4LHC recommendations [133].

7.5 Pile-Up Effects on Physics Objects

In 2012 the running conditions of the LHC were such that there were multiple interactions expected for each bunch crossing. At each crossing the *1st primary interaction vertex*[4] is defined as the interaction which produces the largest scalar sum of transverse momentum. The other interactions create undesirable effects in the detector. There are two main effects: there is the additional noise in the calorimeter which alters the jet energy scale and degrades the $E_{\mathrm{T}}^{\mathrm{miss}}$ resolution, and there is the possibility that one of the additional vertices produces a hard jet which enters the analysis.

The second effect is evaluated by looking at the fraction of the total transverse track momentum pointing at a jet coming from different vertices. Figure 7.2 shows a pictorial representation of this quantity. In Figure 7.3(a)-(b) this fraction is shown for a $Z \rightarrow \mu^+\mu^-$ selection. It is

[3] The NLL correction is used for when the gluino mass lies between 200 GeV and 2 TeV. For masses outside this range cross sections at NLO accuracy obtained with `Prospino 2.1` [129] are used.

[4] *Primary* refers to the fact that this is not a secondary vertex which is due to the displaced decay of a long lived hadron such as a B-meson.

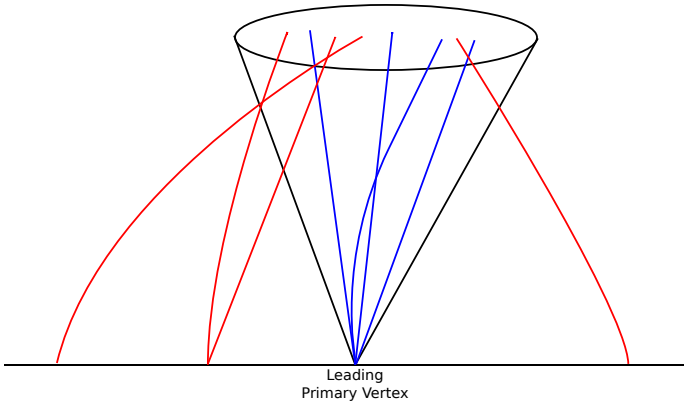

Figure 7.2: A pictorial illustration of the quantity used to evaluate the effect of pile-up. The ratio is taken of the sum of the transverse momenta of tracks from the leading primary vertex associated with the jet (blue) to the sum of the transverse momenta of all tracks associated with the jet (red and blue). *(Not to scale.)*

seen that the chance of the lowest p_{T} jet above $p_{\mathrm{T}} = 55\,\mathrm{GeV}$ coming from a vertex other than the primary vertex is $\sim 4\%$ and is well described by the simulation. As this is small and well modelled it will not significantly affect the analysis.[5]

The pile-up offset correction [85] corrects for the average expected change in the jet energy scale. No variation in the number of jets is seen as a function of the number of primary vertices as shown in Figure 7.3(c). From these studies we can confirm that for jets with $p_{\mathrm{T}} > 55\,\mathrm{GeV}$ which are used in our selection we are relatively safe against effects due to the mis-modelling of pile-up interactions. The degradation of the $E_{\mathrm{T}}^{\mathrm{miss}}$ resolution will enter the analysis, however, for the backgrounds where the $E_{\mathrm{T}}^{\mathrm{miss}}$ originates from the detector resolution, data-driven methods are used. Since the resolution function is determined from data, the Monte Carlo simulation is of no particular importance.

7.6 Pre-Selection

A pre-selection is defined to remove detector related effects. This consists of removing events with jets that fail criteria which suggest that they may be from detector noise or from cosmic ray showers [134]. These criteria are based on the fractions of energy deposited in the different layers and sub-detectors of the calorimeter, the shape of the energy pulse across time, the

[5] This is also an upper bound as these jets could be trackless jets from the 1st primary vertex with a random track from a pile-up vertex.

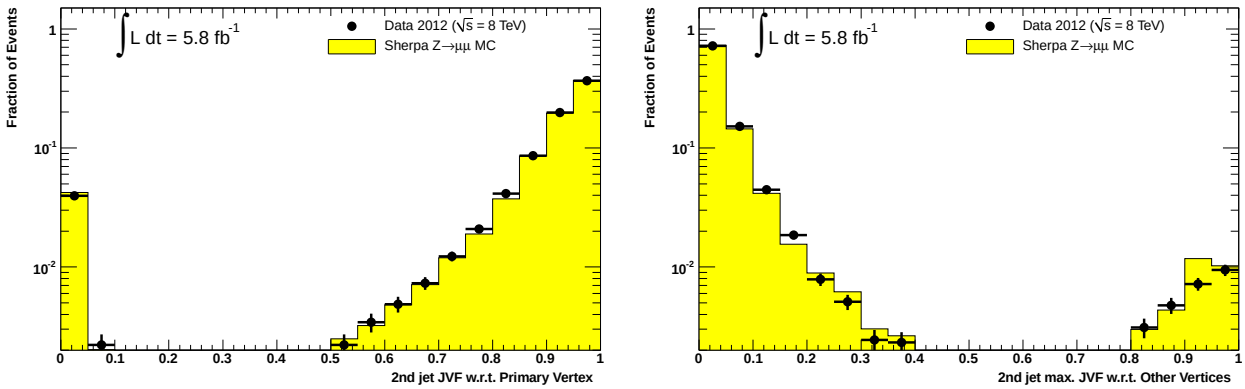

(a) The fraction of the momenta of tracks pointing at the sub-leading jet which originate from the 1st primary interaction vertex.

(b) The maximum fraction of the momenta of tracks from a vertex other than the leading primary vertex pointing at the sub-leading jet.

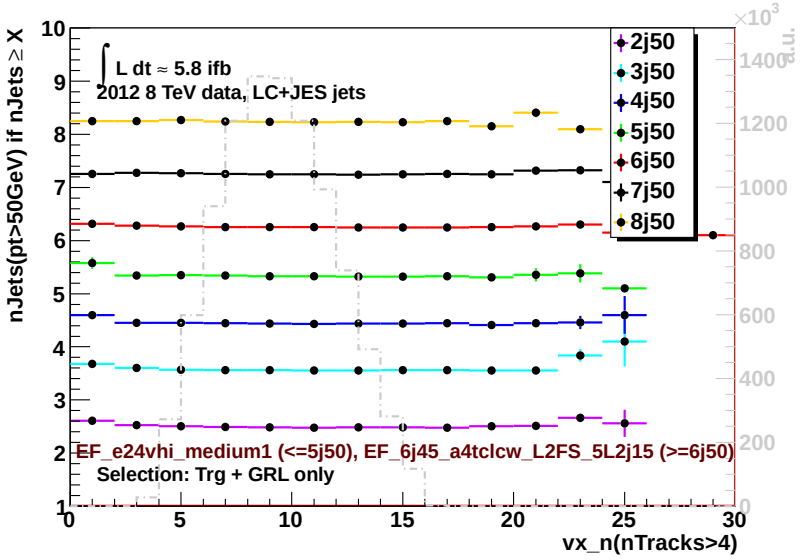

(c) The average number of jets with $p_{\mathrm{T}} > 50\,\mathrm{GeV}$ after requiring n jets above 50 GeV as a function of the number of reconstructed primary vertices. No dependence is observed.

Figure 7.3: Plots showing the effect of pile-up interactions on the analysis. (a) and (b) show the fraction of momentum of tracks pointing at either the leading primary vertex (a) or the maximum fraction pointing at one of the other vertices (b). An event selection of $Z \to \mu^+\mu^-$ candidates with two additional jets with $p_{\mathrm{T}} > 55\,\mathrm{GeV}$ is used. Only events with at least one track pointing at the jet are included and where the tracks are unambiguously associated with vertices. Only a small fraction of the lowest p_{T} jet above $p_{\mathrm{T}} = 55\,\mathrm{GeV}$ are found to originate from pile-up interactions. Figure (c) shows the dependence of the jet energy scale on the number of primary vertices. Electron triggers are used for low jet multiplicity and a multi-jet trigger is used for high jet multiplicity. No dependence on the jet multiplicity for high p_{T} jets with the number of primary vertices is observed. *(Figure (c) was produced by another member of the analysis team.)*

amount of energy originating from negative energy cells and the fraction of the jets energy that can be matched to charged tracks pointing at the jet. These are optimised to reject the great majority of detector related effects, and with a very low inefficiency for real jets from collisions. They are applied to most ATLAS analyses.

As searches looking for large amounts of $E_{\mathrm{T}}^{\mathrm{miss}}$ are particularly sensitive to non-collision backgrounds additional cuts are applied to ensure that these are negligible in the final analysis. These consist of:

- requiring the primary vertex with the largest sum of transverse track momentum to have > 4 tracks,
- rejection of events with muons which have longitudinal or transverse impact parameters greater than 5 mm or 2 mm respectively with respect to the primary vertex, or which have significantly different momentum as measured by the muon spectrometer and tracker.
- rejection of events where either of the leading jets has $p_{\mathrm{T}} > 100\,\mathrm{GeV}$, is central, and has a very low fraction of its energy that can be matched to charged tracks pointing at it,
- if the energy weighted mean time of up to the leading four selected jets is greater than 5 ns again the event is rejected.

During the period that the data were taken there were some tile drawers which were non-operational primarily due to low-voltage power supply issues. This leads to a degradation in the $E_{\mathrm{T}}^{\mathrm{miss}}$ resolution for events where jets fall in these areas. Also in any period of operation there are some cells which are noisy so they are masked further degrading the optimal detector resolution. The amount of energy that is lost in the dead area can be estimated by two separate methods; by using the average of the surrounding cells or by using the jet profile in the surrounding area. By default in ATLAS the first of these methods is employed in jet reconstruction and the measurement of the $E_{\mathrm{T}}^{\mathrm{miss}}$. We compute the correction to the $E_{\mathrm{T}}^{\mathrm{miss}}$ that would be applied if the second more sophisticated method was employed. If the correction from any single jet is found to be $> 10\,\mathrm{GeV}$ in the direction of the $E_{\mathrm{T}}^{\mathrm{miss}}$ and $> 10\%$ of the total $E_{\mathrm{T}}^{\mathrm{miss}}$ then the event is rejected. Occasionally the jet profile correction is insufficient to fully estimate the lost energy so a second cut is also employed; events are rejected if they have a jet which lies within

Signal region	**7j55**	**8j55**	**9j55**	**6j80**	**7j80**	**8j80**
Number of isolated leptons (e, μ)	$= 0$					
Jet p_{T}	$> 55\,\mathrm{GeV}$			$> 80\,\mathrm{GeV}$		
Jet $\lvert\eta\rvert$	< 2.8					
Number of jets	≥ 7	≥ 8	≥ 9	≥ 6	≥ 7	≥ 8
$E_{\mathrm{T}}^{\mathrm{miss}}/\sqrt{H_{\mathrm{T}}}$	$> 4\ \mathrm{GeV}^{1/2}$					

Table 7.1: Definitions of the six signal regions.

0.2 rad of the $E_{\mathrm{T}}^{\mathrm{miss}}$ in the azimuthal plane, with $p_{\mathrm{T}} > 40\,\mathrm{GeV}$, $|\eta| < 2.8$, and which has lost more than 5% of its energy according to the jet profile estimation such that is is determined to be pointing at a dead area of the detector.

The above pre-selection is employed in all aspects of the analysis.

7.7 Signal Regions

Signal regions are based on loose optimisation studies as they are designed to be fairly generic and not look for any specific model of Supersymmetry at the expense of losing sensitivity to others. The number of jets above a two different p_{T} cuts (55 GeV and 80 GeV) with $|\eta| < 2.8$ are counted and signal regions are defined requiring at least n jets, where the value of n depends on the signal region. Finally a $E_{\mathrm{T}}^{\mathrm{miss}}/\sqrt{H_{\mathrm{T}}} > 4\,\mathrm{GeV}^{1/2}$ is applied to cut out the majority of the background from sources without real $E_{\mathrm{T}}^{\mathrm{miss}}$ where H_{T} is defined as the scalar sum of the p_{T} of all jets with $p_{\mathrm{T}} > 40\,\mathrm{GeV}$ and $|\eta| < 2.8$. The value of this final cut is chosen such that good statistics remain in the regions used to validate the method used to determine the background from multi-jet events. Signal regions are defined up to the highest multiplicities where the signal region expectation from the Standard model background is > 1 event. Table 7.1 details the selection of the six signal regions.

7.8 Background Estimation

The Standard Model backgrounds to this search can be categorised into two distinct types: those dominated by $E_{\mathrm{T}}^{\mathrm{miss}}$ originating from jet mis-measurement and those where the $E_{\mathrm{T}}^{\mathrm{miss}}$ is dominated by prompt neutrinos passing through the detector undetected. The methods for evaluating these are different. In §7.8.1 the method for determining the backgrounds without prompt neutrinos (including fully hadronic $t\bar{t}$, hadronically decaying vector bosons and pure QCD processes) is described. The backgrounds with prompt neutrinos, primarily consisting of semi- and di-leptonic $t\bar{t}$, W bosons decaying to a charged lepton and a neutrino and Z bosons decaying to neutrinos, are referred to as "leptonic" backgrounds and the method for determining these backgrounds is described in §7.8.2.

7.8.1 Multi-jet Background

Description of the method

The backgrounds which have no prompt neutrinos from the decays of vector bosons are all treated together. These include pure QCD processes, fully hadronic $t\bar{t}$ events as well as hadronically decaying vector bosons. In events where many high p_{T} jets are present the $E_{\mathrm{T}}^{\mathrm{miss}}$ primarily arises due to a momentum imbalance due to the mis-measurement of the energy of the jets. Both the simulation of the physics of these multi-jet processes and the modelling of the detector jet resolution are difficult so data driven techniques are used to ensure that the uncertainties on the predicted size of these backgrounds are under control. The selection cut on $E_{\mathrm{T}}^{\mathrm{miss}}/\sqrt{H_{\mathrm{T}}}$ is chosen such that this is possible. The jet resolution of the ATLAS detector is proportional to $\sqrt{p_{\mathrm{T}}}$ across a large range of jet p_{T}. This leads to the $E_{\mathrm{T}}^{\mathrm{miss}}$ resolution of events with high jet multiplicity being approximately proportional to $\sqrt{H_{\mathrm{T}}}$. Therefore it is expected that the distribution of the ratio $E_{\mathrm{T}}^{\mathrm{miss}}/\sqrt{H_{\mathrm{T}}}$ will be very similar for selections requiring different numbers, n, of jets, for large n. This means that a template for the $E_{\mathrm{T}}^{\mathrm{miss}}/\sqrt{H_{\mathrm{T}}}$ distribution can be extracted from lower jet multiplicity selections where SUSY signal contamination is expected to be small and then applied to the signal region jet multiplicity requirements. This template is normalised in the region requiring $E_{\mathrm{T}}^{\mathrm{miss}}/\sqrt{H_{\mathrm{T}}} < 1.5\,\mathrm{GeV}^{1/2}$.

For example, the multi-jet prediction for a signal region requiring ≥ 8 jets with $p_{\mathrm{T}} > 55\,\mathrm{GeV}$ and $E_{\mathrm{T}}^{\mathrm{miss}}/\sqrt{H_{\mathrm{T}}} > 4\,\mathrm{GeV}^{1/2}$ can be found by forming a template describing the shape of the $E_{\mathrm{T}}^{\mathrm{miss}}/\sqrt{H_{\mathrm{T}}}$ distribution from events with exactly six jets with the same p_{T} threshold. This is then normalised in the region with $E_{\mathrm{T}}^{\mathrm{miss}}/\sqrt{H_{\mathrm{T}}} < 1.5\,\mathrm{GeV}^{1/2}$ and ≥ 8 jets. The normalised template then provides the prediction for the signal region selection with $E_{\mathrm{T}}^{\mathrm{miss}}/\sqrt{H_{\mathrm{T}}} > 4\,\mathrm{GeV}^{1/2}$. For all the regions used to form the prediction the numbers of observed events are corrected for the expected contamination from "leptonic" processes.

The invariance of this variable under changes in jet multiplicity is tested in data at lower multiplicity than that which we probe and the good closure was seen in both 2011 and 2012 data. In 2012 the average number of other interactions per crossing (pile-up) increased which results in increased soft energy throughout the detector. This energy does not normally take the form of hard jets and therefore contributions to the term in the $E_{\mathrm{T}}^{\mathrm{miss}}$ calculation which includes clusters which are not part of hard objects. This means that while the $E_{\mathrm{T}}^{\mathrm{miss}}$ is dominated by jet mis-measurement there is a second order effect which is dependent on the sum of the unclustered energy. This second order effect is taken into account by forming templates separately for 8 bins (0 to 0.7 with width of 0.1 and a final inclusive bin) of;

$$\sum \mathrm{E}_{\mathrm{T}}^{\mathrm{CellOut}}/H_{\mathrm{T}}, \tag{7.1}$$

where the numerator is the scalar sum of all the clusters that are not associated with hard objects, such that this variable captures the relative importance of the soft terms compared to the resolution of the hard jets. The distribution in data of this variable in the region of $E_{\mathrm{T}}^{\mathrm{miss}}/\sqrt{H_{\mathrm{T}}} < 1.5\ \mathrm{GeV}^{1/2}$ is shown in Figure 7.4.

This method of predicting the multi-jet background is tested by looking at the prediction for exactly six jets with $p_{\mathrm{T}} > 55\,\mathrm{GeV}$ where the prediction is taken from events with exactly five jets with $p_{\mathrm{T}} > 55\,\mathrm{GeV}$. Similarly for the higher jet threshold, we consider the prediction for exactly five jets with $p_{\mathrm{T}} > 80\,\mathrm{GeV}$ using templates from exactly four jets with $p_{\mathrm{T}} > 80\,\mathrm{GeV}$. Figure 7.5 shows the distribution of $E_{\mathrm{T}}^{\mathrm{miss}}/\sqrt{H_{\mathrm{T}}}$ for these two selections. The events in both cases are taken from pre-scaled triggers which require at least five jets above 45 GeV or at least four jets above 65 GeV. Very good agreement in the shape of the distributions is seen

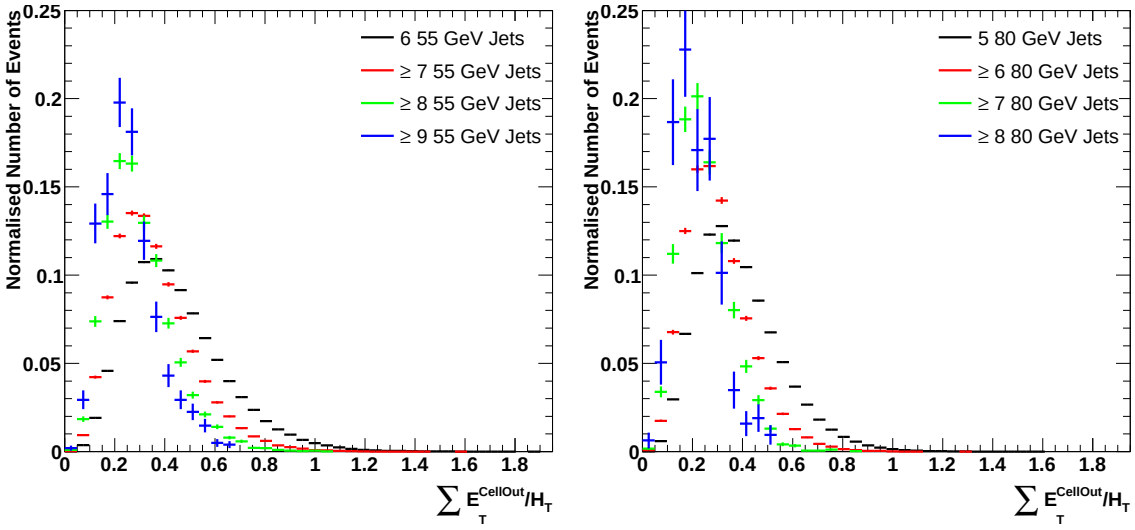

(a) (b)

Figure 7.4: The distribution of $\sum \mathrm{E}_{\mathrm{T}}^{\mathrm{CellOut}}/H_{\mathrm{T}}$ in the region with $E_{\mathrm{T}}^{\mathrm{miss}}/\sqrt{H_{\mathrm{T}}}$< 1.5 $\mathrm{GeV}^{1/2}$.

between the prediction and the observed numbers of events. Adequate numbers of events are present beyond the cut value of 4 $\mathrm{GeV}^{1/2}$ such that confidence in the method is achieved. Furthermore, as more jets are required the kinematic differences between the control region and signal region multiplicities are reduced such that the method can be expected to provide more accurate predictions than the closure achieved in these control regions.

Systematic uncertainties

As this method is completely data driven (with the exception of the subtraction of the "leptonic" backgrounds in the computation) different uncertainties dominate than is usually the case in LHC SUSY searches (where the Jet Energy Scale determination provides large uncertainties eg. [110]). Here, data driven uncertainties are derived based on the agreement observed in similar regions to the signal regions but where signal contamination is expected to be small, and by varying the exact prescription of the method.

Closure: The closure of the method has already been shown in Figure 7.5. The degree to which the various assumptions made in forming the template are valid can be evaluated by looking at the degree of agreement in regions of phase space surrounding the signal region which are expected to contain little signal. Regions which are both at lower multiplicity and with the same $E_{\mathrm{T}}^{\mathrm{miss}}/\sqrt{H_{\mathrm{T}}}$ criteria, and at the same multiplicity as the signal regions but

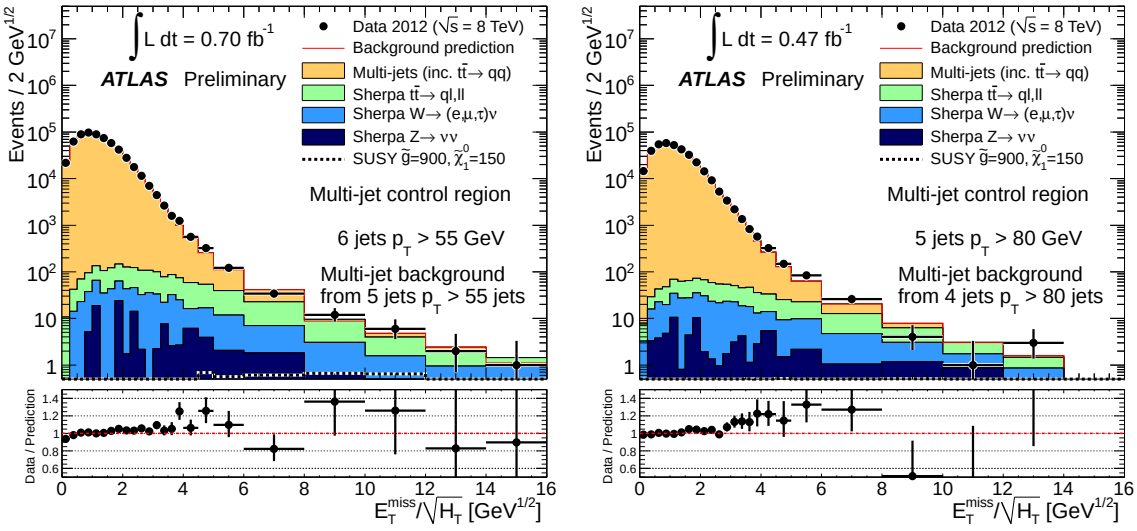

(a) (b)

Figure 7.5: The $E_{\mathrm{T}}^{\mathrm{miss}}/\sqrt{H_{\mathrm{T}}}$ distributions for jet multiplicities lower than the signal region where the multi-jet prediction has been taken from a selection one lower in jet multiplicity. Good agreement between the prediction and observed shapes of the distribution is observed. These regions are used to test the assumptions of the method of determining the multi-jet background and it is observed to work well and the small deviations seen are taken as systematic uncertainties on the method.

lower $E_{\mathrm{T}}^{\mathrm{miss}}/\sqrt{H_{\mathrm{T}}}$, are considered such that as much of phase space as possible is covered. The systematic uncertainty is taken as the maximal deviation from prediction in various bins of $E_{\mathrm{T}}^{\mathrm{miss}}/\sqrt{H_{\mathrm{T}}}$. For the 55 GeV p_{T} cut, regions in $E_{\mathrm{T}}^{\mathrm{miss}}/\sqrt{H_{\mathrm{T}}}$ are defined in the following ranges for exactly six jets: $[1.5-2, 2-2.5, 2.5-3.5, 4+]\,\mathrm{GeV}^{1/2}$. Additionally, regions for all higher inclusive jet multiplicities up to that of the signal region defined by: $[1.5-2, 2-2.5, 2.5-3.5]\,\mathrm{GeV}^{1/2}$ are considered. In the regions with the 80 GeV p_{T} cut an identical approach is taken checking the larger set of bins for five jets and then the lower $E_{\mathrm{T}}^{\mathrm{miss}}/\sqrt{H_{\mathrm{T}}}$ set for all multiplicities up to the signal regions. All these regions are shown in Figures 7.5 and 7.11 (the latter is in the results section as it contains the signal region distribution at high values of $E_{\mathrm{T}}^{\mathrm{miss}}/\sqrt{H_{\mathrm{T}}}$). It is found that the closure uncertainties range from 8.7-19% for the loosest to tightest signal regions. It should be noted that the tightest signal regions have larger systematics due to the lack of events in some of the regions checked.

Heavy flavour decays: When heavy flavour hadrons decay they can do so through leptonic channels which result in neutrinos that contribute to the detector resolution. These effects are captured at leading order through the template method and any large deviations caused by

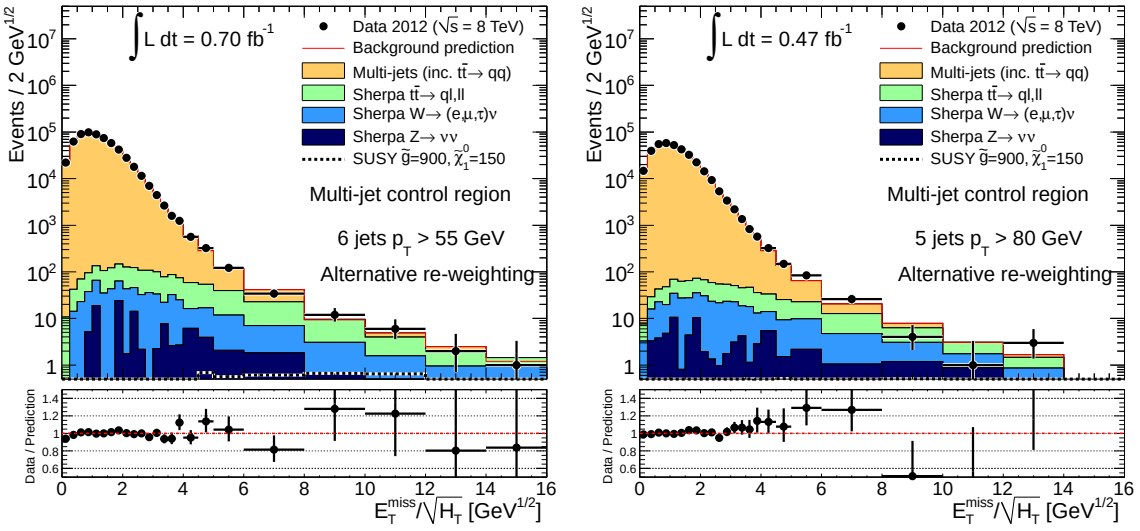

(a) (b)

Figure 7.6: The $E_{\mathrm{T}}^{\mathrm{miss}}/\sqrt{H_{\mathrm{T}}}$ distributions for jet multiplicities lower than the signal region where the multi-jet prediction has been taken from a selection one lower in jet multiplicity and the alternative re-weighting is used.

this effect would have been observed in the closure tests. However, the fraction of events with heavy flavour hadrons may change with jet multiplicity. Therefore to take this into account separate templates are formed for events with a b-tagged jet and those without any b-tagged jets. These two orthogonal contributions are then summed and compared to the approach that does not take the varying heavy flavour fraction into account. The difference between the two predictions is taken as a systematic uncertainty.

Soft energy re-weighting: The upper cut used to define which clusters enter the re-weighting of the template to account for the soft energy contributions to the $E_{\mathrm{T}}^{\mathrm{miss}}$ is raised to include jets up to 20 GeV to check the dependence of the prediction on the exact value of this cut. The difference between the signal region predictions with the two different cut values is taken as a systematic uncertainty on the method prescription. The agreement for the lower multiplicity control regions using this alternative re-weighting is shown in Figure 7.6.

Subtraction of "leptonic" backgrounds: There are uncertainties on how well the "leptonic" contributions are known for their subtraction in the formation of the template. These are known to within 20% taking into account both experimental and theoretical uncertainties. This degree of agreement is also demonstrated in control regions requiring an electron or muon

Signal Region	Closure	Heavy Flavour	Soft Energy	"Leptonic" subtraction	Total
7j55	±8.7%	±8.3%	±9.0%	±9.6%	±18%
8j55	±17%	±17%	±8.9%	±11%	±28%
9j55	±17%	±23%	±8.5%	±12%	±32%
6j80	±19%	±11%	±3.4%	±9.2%	±24%
7j80	±19%	±22%	±2.4%	±9.1%	±30%
8j80	±19%	±30%	±1.8%	±8.9%	±37%

Table 7.2: The different systematics on the multi-jet background for the six signal regions. Similar levels of uncertainty come from closure, "leptonic" subtraction and heavy flavour components.

in §7.8.2. A conservative systematic is estimated by scaling the Monte-Carlo prediction used in the template creation up and down by 20%. The difference between these and the nominal prediction is taken as systematic uncertainty on the shape of the template due to the uncertainty on the subtraction of the "leptonic" backgrounds.

Summary of systematics: The systematic uncertainties for the six different signal regions from the sources described above are listed in Table 7.2. For the tightest signal regions the largest source of uncertainty comes from the varying heavy flavour fraction while for the loosest signal regions the different contributions provide similar contributions to the overall systematic.

7.8.2 "Leptonic" Backgrounds

Description of the method

The method used to determine the main backgrounds having real $E_{\mathrm{T}}^{\mathrm{miss}}$ from prompt neutrinos is to normalise these backgrounds in regions with very similar kinematic criteria to the signal regions, but differ in that they are required to contain either one (for W and $t\bar{t}$) or two (for Z) high p_{T} electron(s) or muon(s). Monte-Carlo simulation is then used to determine the ratio between these control regions and the signal regions - the transfer factor, TF:

$$\begin{aligned} (\text{Events predicted in SR}) &= (\text{Events observed in CR}) \times \text{TF} && (7.2) \\ &= (\text{Events observed in CR}) \times \frac{(\text{MC prediction in SR})}{(\text{MC prediction in CR})} && (7.3) \end{aligned}$$

We choose to select regions that are as close as possible to the signal regions (even when statistical uncertainties become limiting) such that the reliance on the accuracy of the simulations is reduced as much as possible. As a result we find a high degree of cancellation of both the experimental and theoretical uncertainties on these backgrounds when using this ratio rather than the raw prediction. For the very tightest signal regions there are insufficient events in the control regions, and so the Monte-Carlo predictions with their full uncertainties are used. In these cases careful validation of the Monte-Carlo simulations (which are at leading order) is necessary to make sure that they are able to describe these areas of phase space accurately.

$t\bar{t}$ and W+jets backgrounds: To control and validate the simulations of these processes events were selected that containted an electron on muon with $p_{\mathrm{T}} > 25\,\mathrm{GeV}$ which satisfied the additional isolation criteria and, in the case of electrons, tighter shower shape criteria. These events were additionally required to have no additional leptons. With this selection there is still a small amount of contamination from non-prompt leptons from heavy flavour decays and hadronic jets which fake electrons. This is then minimised by applying a cut on the transverse mass of the lepton, defined by:

$$m_{\mathrm{T}} = \sqrt{2E_{\mathrm{T}}^{\mathrm{miss}} p_{\mathrm{T}}^{l}(1 - \cos(\Delta\phi))},$$

where $\Delta\phi$ is the azimuthal angle between the lepton and the missing transverse energy vector. For events with a single muon a cut of $m_{\mathrm{T}} > 40\,\mathrm{GeV}$ is seen to reduce this background to an acceptable level while for events with electrons a more stringent cut of $m_{\mathrm{T}} > 60\,\mathrm{GeV}$ is applied. To reduce the possibility of supersymmetric events populating these regions, an upper cut of $m_{\mathrm{T}} < 100\,\mathrm{GeV}$ is also applied. After this selection a reasonably pure sample of $t\bar{t}$ and W+jets is observed at high jet multiplicity.

Many different kinematic distributions were studied with this selection and the `SHERPA` Monte-Carlo was observed to provide a reasonable description. Although, in some inclusive variables such as the $E_{\mathrm{T}}^{\mathrm{miss}}$ it was observed to provide a slightly harder spectra than the data. Comparison with NLO simulations at low jet multiplicity where they are still reliable showed that this may be a NLO effect not taken into account in the `SHERPA` Monte-Carlo. Truth level

studies of $t\bar{t}$ showed similar results and it was noticed that by re-weighting the events that were initiated by two gluons from the parton distribution function but keeping the overall top cross-section constant, better agreement with the NLO calculation would be seen in the inclusive variables at low multiplicity. Examples of these distributions are shown in Figure 7.7. This re-weighting of the Monte-Carlo is tested against the data and the data/Monte-Carlo agreement of the jet multiplicity distribution is seen to be improved. As this is not a full calculation but a re-weighting based on the data, the full difference between the re-weighted Monte-Carlo and the nominal sample is taken as an additional systematic uncertainty on the top background.

Control regions should be as close kinematically to the signal regions as possible. To accomplish this, the same jet multiplicity as the signal region is required and, as the majority of the background that satisfies the signal region requirements comes from hadronically decaying taus, the lepton is included in the jet multiplicity count if it satisfies the relevant criteria. The same $E_{\mathrm{T}}^{\mathrm{miss}}/\sqrt{H_{\mathrm{T}}}$ criteria are also applied. This selection, also detailed in Table 7.3, is very close to the signal region but contains little signal contamination. This jet multiplicity distribution for the signal region jet criteria is shown in Figure 7.8 and for the prediction of these backgrounds in the $\geq$7 and $\geq$8 55 GeV jet and the $\geq$6 and $\geq$7 80 GeV jet signal regions sufficient statistics exist in the control regions of the same multiplicity. Therefore, to form the prediction for these signal regions the Monte-Carlo is used to provide the ratio between the control region and the signal region and this is then applied to the observed number of data events in the control region.

It finally remains to evaluate the background from non-prompt leptons or hadronic activity faking leptons in these control regions. This is accomplished by reversing the additional isolation and shower shape criteria to select a sample of events with fake leptons. For this sample the multi-jet triggers are used since the single lepton triggers include isolation criteria. This selection is then used to form a template for the shape of the $E_{\mathrm{T}}^{\mathrm{miss}}/\sqrt{H_{\mathrm{T}}}$ distribution and this is then normalised in the region with $E_{\mathrm{T}}^{\mathrm{miss}}/\sqrt{H_{\mathrm{T}}} < 2$ GeV$^{1/2}$ for the isolated selection. Due to the lack of significant statistics of non-prompt muons even when the isolation criteria are reversed the electron template is used for the prediction in both cases. Also, to improve statistics the m_{T} criteria are not applied. Even without the m_{T} cuts it is found that the

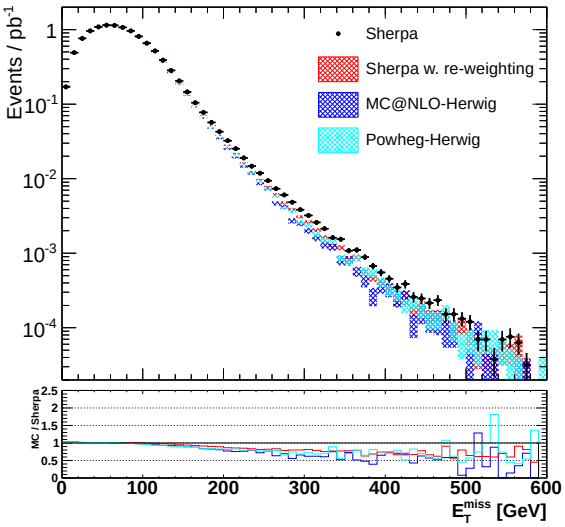

(a) The Missing Transverse Energy.

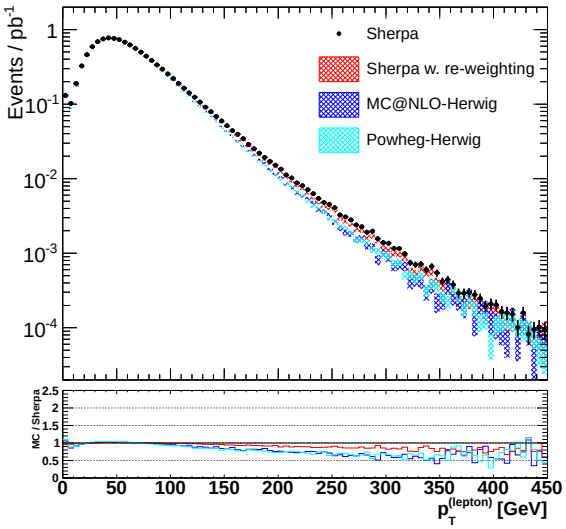

(b) The leading lepton p_{T}.

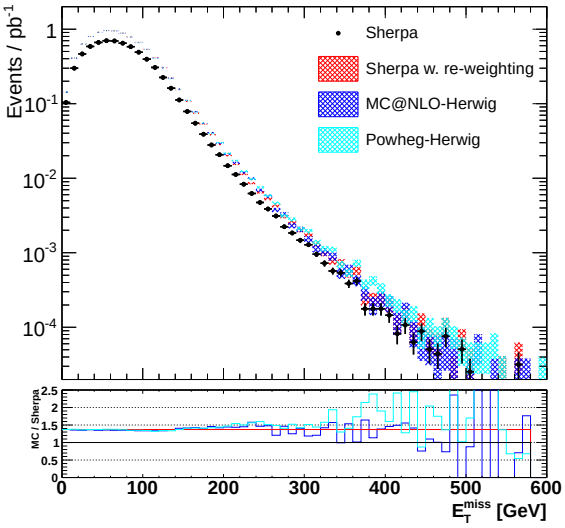

(c) The Missing Transverse Energy for events initiated by two gluons from the PDFs.

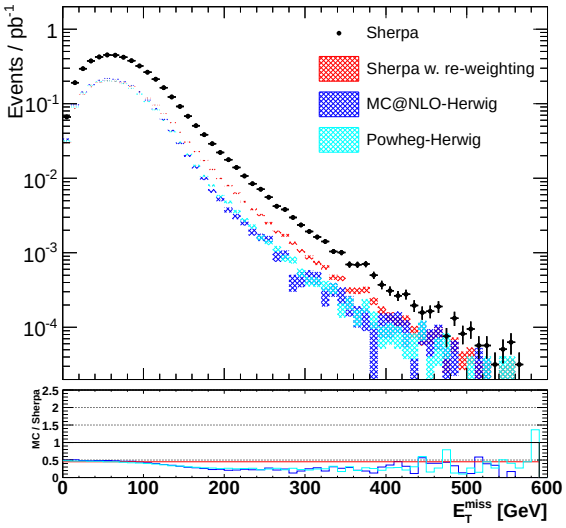

(d) The Missing Transverse Energy for events not initiated by two gluons from the PDFs.

Figure 7.7: Truth level motivation for the $t\bar{t}$ re-weighting. (a) and (b) show the $E_{\mathrm{T}}^{\mathrm{miss}}$ and leading lepton p_{T}, for di-leptonic (electron or muon) $t\bar{t}$ events. The `PowHeg` and `MC@NLO` (both showered with `HERWIG`) simulations are seen to be softer than the `SHERPA` Monte-Carlo. (c) and (d) show the $E_{\mathrm{T}}^{\mathrm{miss}}$ distribution for events initiated by two gluons and others respectively. It is clear that the agreement between the LO multi-leg Monte-Carlo can be improved by re-weighting in this variable. This is seen in (a) and (b) where the re-weighted Sherpa distribution is also shown. All of the error bands are purely statistical.

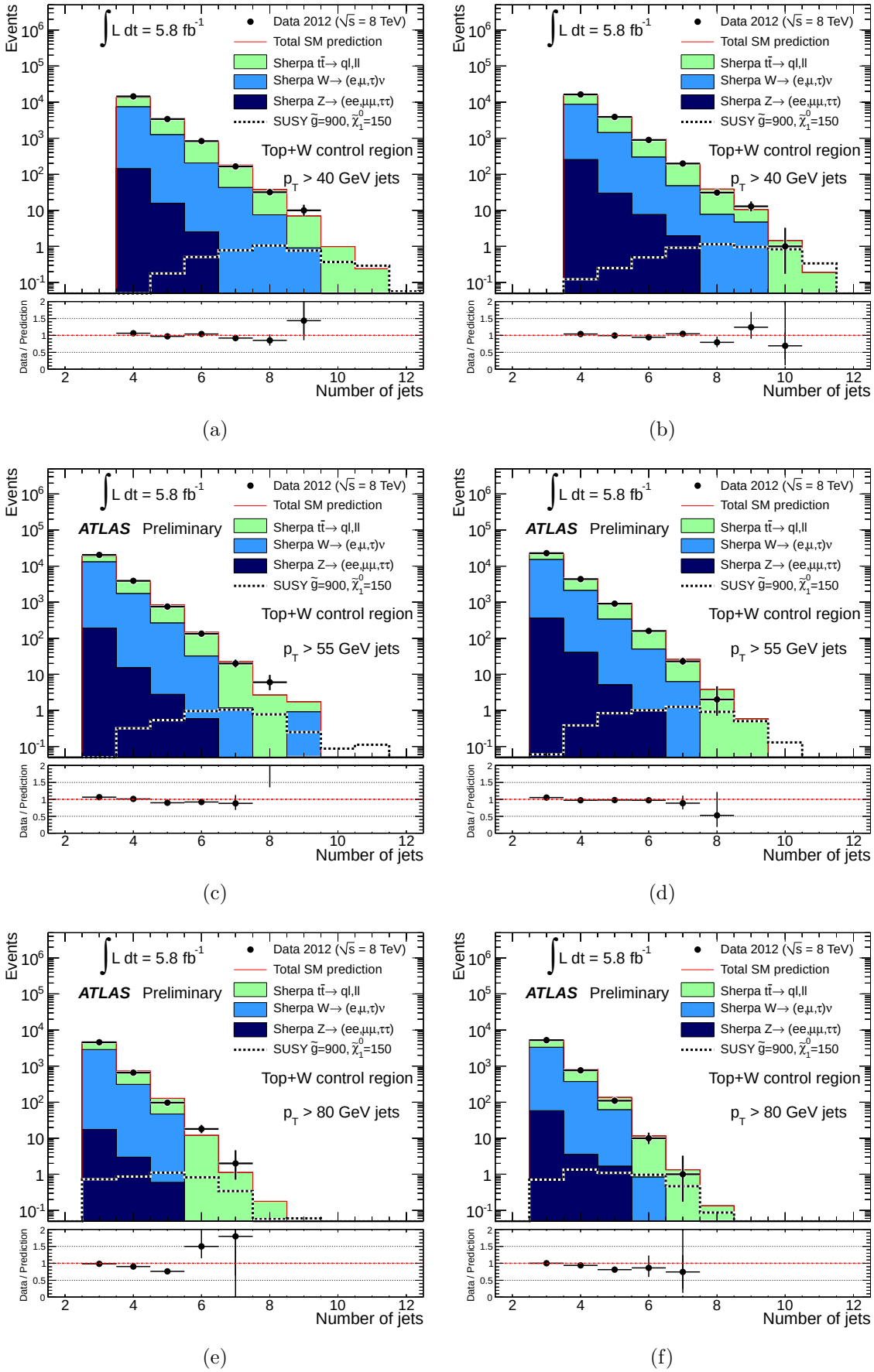

Figure 7.8: The jet multiplicity distribution for the control regions for $t\bar{t}$ and W+jets. (a) and (b) show the jet multiplicity distribution for $p_{\mathrm{T}} > 40\,\mathrm{GeV}$ jets for the electron and muon selections respectively. (c) and (d) show the distribution for $p_{\mathrm{T}} > 55\,\mathrm{GeV}$ jets while (e) and (f) are for $p_{\mathrm{T}} > 80\,\mathrm{GeV}$ jets.

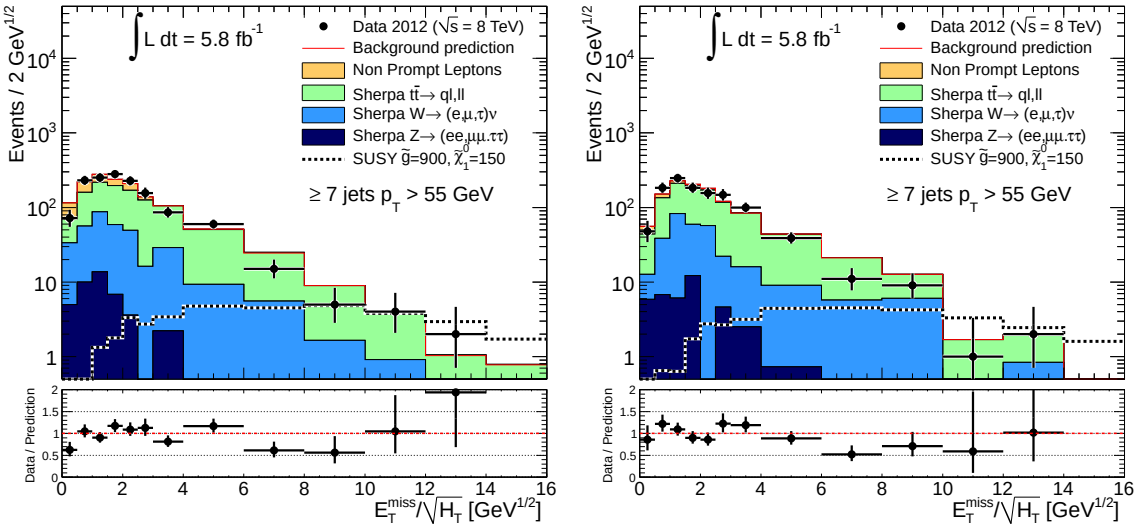

(a) (b)

Figure 7.9: The $E_{\mathrm{T}}^{\mathrm{miss}}/\sqrt{H_{\mathrm{T}}}$ distribution for a single electron (a) or muon (b) selection and ≥ 7 jets with $p_{\mathrm{T}} > 55\,\mathrm{GeV}$ (including the lepton). The background from processes without prompt leptons is mainly at low values of $E_{\mathrm{T}}^{\mathrm{miss}}/\sqrt{H_{\mathrm{T}}}$ and above the cut value of $4\,\mathrm{GeV}^{1/2}$ it is negligible.

background from these sources is negligible - for the seven 55 GeV jet selection the predictions using this method are 0.1 and 0.03 events for the electron and muon selections respectively. The $E_{\mathrm{T}}^{\mathrm{miss}}/\sqrt{H_{\mathrm{T}}}$ distributions are shown in Figure 7.9, showing good agreement using this method. It is therefore safe to discard this background as the m_{T} cuts will reduce it even further.

Z+jets background: In the signal regions the Z+jets background originates from the boson decaying $Z \to \nu\bar{\nu}$ such that it is natural to consider a control region where a Z boson decays to light charged leptons, e or μ. The same approach as the $t\bar{t}$ and W+jets estimation is followed defining validation and control regions. However, due to the small cross-section of a Z boson in association with a very large number of jets insufficient statistics remain at the highest multiplicities to normalise the Monte-Carlo. Therefore the prediction is taken directly from Monte-Carlo which we have validated at lower multiplicity.

Validation regions are defined by requiring two leptons, the first with $p_{\mathrm{T}}> 25\,\mathrm{GeV}$ and the sub-leading with $p_{\mathrm{T}}> 20\,\mathrm{GeV}$. The invariant mass of the lepton pair has to lie between 80 GeV and 100 GeV and both of them are required to satisfy the additional shower shape and isolation criteria. This forms a very pure sample of Z+jets events. The performance of the Monte-Carlo is then tested with this selection and good agreement is seen between the data and prediction

	$t\bar{t}$ + jets and W + jets		Z + jets
Lepton type	electron	muon	muon
Lepton p_{T}	$p_{\mathrm{T}} > 25$ GeV, $\lvert\eta\rvert < 2.4$		
Lepton $\lvert\eta\rvert$	< 2.47	< 2.4	< 2.4
Lepton multiplicity	$= 1$		$= 2$
m_{T} or $m_{\mu\mu}$	60 GeV $< m_{\mathrm{T}} <$ 100 GeV	40 GeV $< m_{\mathrm{T}} <$ 100 GeV	80 GeV $< m_{\mu\mu} <$ 100 GeV
Emulate SR	$e \rightarrow$ jet	$\mu \rightarrow$ jet	$\mu \rightarrow \nu$
Jet p_{T}, $\lvert\eta\rvert$, mult.	As in Table 7.1.		
$E_{\mathrm{T}}^{\mathrm{miss}}/\sqrt{H_{\mathrm{T}}}$			

Table 7.3: Definitions of the control regions for the $t\bar{t}$, W+jets and Z+jets backgrounds.

in the variables of interest.

To form control regions that are as close in kinematics as possible to the signal regions we consider that in the signal region we require $E_{\mathrm{T}}^{\mathrm{miss}}/\sqrt{H_{\mathrm{T}}} > 4$ GeV$^{1/2}$. To emulate this cut we require that $E_{\mathrm{T}}^{\mathrm{miss}}/\sqrt{H_{\mathrm{T}}} > 4$ GeV$^{1/2}$ having added the transverse momenta of two leptons to form the equivalent $E_{\mathrm{T}}^{\mathrm{miss}}$ that would be present if the boson had decayed to neutrinos. Control regions would then require the same jet multiplicity cuts as the signal regions as shown in Table 7.3. Figure 7.10 shows the jet multiplicity distribution for 40, 55 and 80 GeV jet requirements. Good agreement is seen to the highest multiplicities that statistics still remain, however for the signal region multiplicities insufficient statistics remain to use these for normalisation of the Monte-Carlo estimation. However, the Monte-Carlo is seen to be reliable to the highest multiplicities and very conservative systematics are assigned to this background.

Systematic uncertainties

There are two types of systematic uncertainties associated with these backgrounds; those that originate from detector related uncertainties, such as the energy scale and resolution of jets and how well they are described by the simulations, and those that originate from the theoretical description of the generated events.

Experimental uncertainties are dominated by the jet energy scale (JES) uncertainty and the jet energy resolution (JER) uncertainty. These are determined centrally within the collaboration using data driven calibration methods such as the balancing of a jet against a photon or two leptons from the decay of the Z boson. The corresponding uncertainties on the electron and

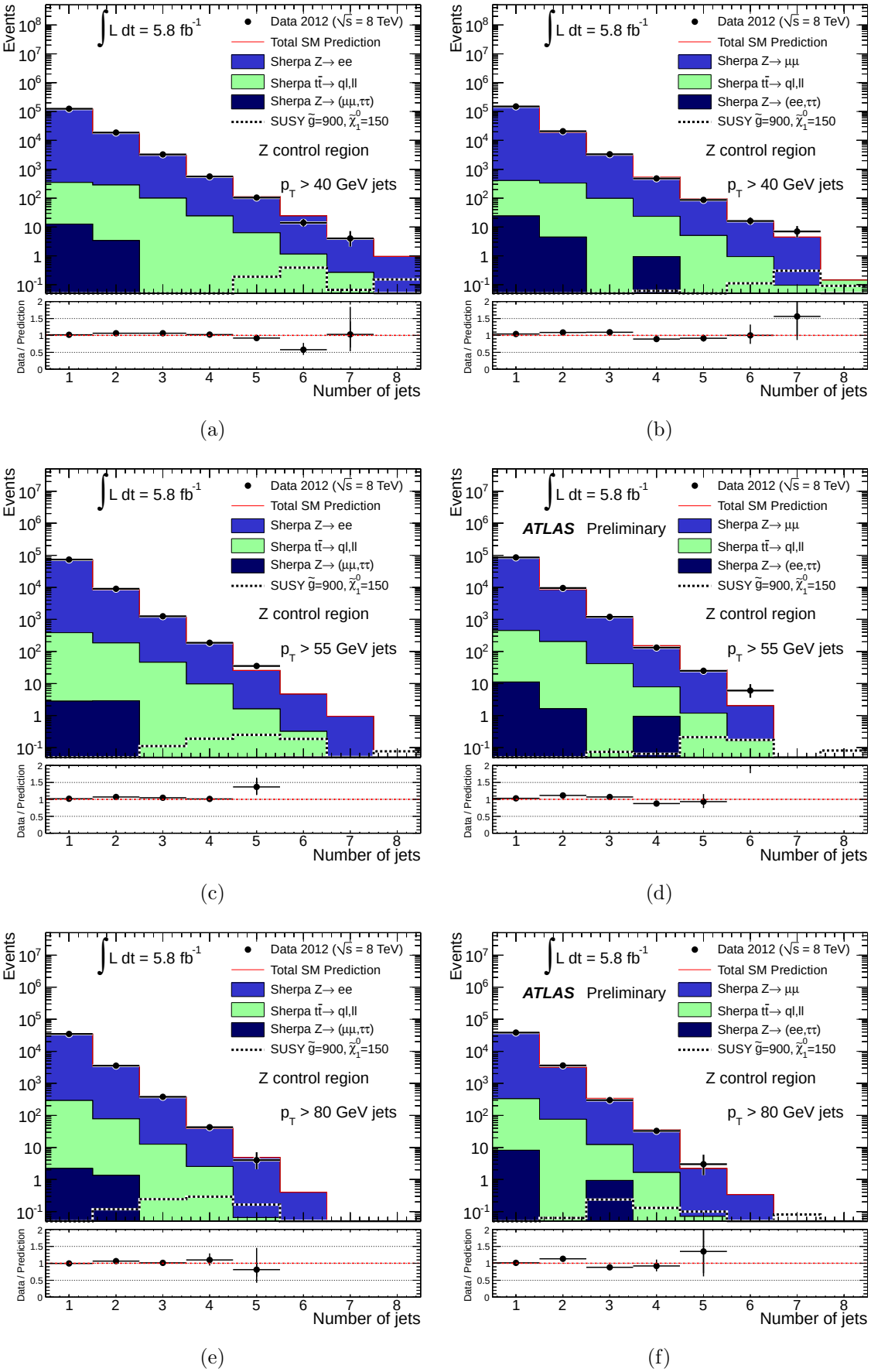

Figure 7.10: The jet multiplicity distribution for the control regions for Z+jets. (a) and (b) show the jet multiplicity distribution for $p_{\mathrm{T}} > 40\,\mathrm{GeV}$ jets for the electron and muon selections respectively. (c) and (d) show the distribution for $p_{\mathrm{T}} > 55\,\mathrm{GeV}$ jets while (e) and (f) are for $p_{\mathrm{T}} > 80\,\mathrm{GeV}$ jets.

muon energy scales and resolutions are better known and are found to be negligible. Similarly the uncertainties from electron and muon identification efficiencies are also negligible compared with the other sources of systematic uncertainty. The number of additional pile-up interactions is shifted up by 10% to provide a measure of the sensitivity of the analysis to the modelling of these additional soft interactions. This dependence is found to be relatively small. Table 7.4 shows the values of these different sources of systematic uncertainty and also demonstrates how in the regions where there are sufficient control region statistics how these are reduced by using transfer factors. For example in the ≥ 8 jets with $p_{\mathrm{T}} > 55\,\mathrm{GeV}$ signal region the upward uncertainty on the JES is reduced from almost 60% to 8%.

Theoretical uncertainties come from varying the generator parameters and generating new samples. These variations are produced at truth level and are compared to the nominal samples at truth level. For the primary $t\bar{t}$ background, the factorisation scale is varied up and down by a factor of two, the matching scale is raised and lowered by 10 GeV and samples are generated with one fewer parton in the matrix element calculation to assess the sensitivity to the finite number of legs that can be present in the calculation. Furthermore, as the $t\bar{t}$ and W backgrounds are measured together in the same control regions there is an additional degree of freedom in the relative contribution of these two background sources. To assess this the W cross-section is scaled up by 25% and the difference between the predictions under this new assumption is taken as a systematic uncertainty. Finally, as mentioned earlier, the re-weighting of the $t\bar{t}$ background to improve agreement in kinematic variables is removed to assess how much this is changing the prediction. The uncertainty due to the CKKW matching scale is found to be negligible. The values of the other systematics are given in Table 7.4. Again there is factorisation of these uncertainties in when the transfer factor approach is used, particularly in the uncertainty due to the finite number of partons and the re-weighting procedure.

For the Z+jets background where the numbers of expected events in control regions are too low to use to normalise the Monte-Carlo estimation an additional systematic uncertainty is used to cover effects which might arise from the use of lower p_{T} jets in the validation of the Monte-Carlo. As this is a very small background this additional systematic used to cover potential mis-modelling in the Monte-Carlo has little effect on the final results.

Error Source	7j55 SR	7j55 CR	7j55 TF	8j55 SR	8j55 CR	8j55 TF	9j55 SR
JES	$^{+38\%}_{-28\%}$	$^{+35\%}_{-23\%}$	$^{+1.3\%}_{-6.3\%}$	$^{+59\%}_{-20\%}$	$^{+46\%}_{-19\%}$	$^{+8\%}_{-1\%}$	$^{+89\%}_{-31\%}$
JER	$\pm 10\%$	$\pm 5\%$	$\pm 5\%$	$\pm 15\%$	$\pm 27\%$	$\pm 9\%$	$\pm 7\%$
Pile-Up	$\pm 1.2\%$	$\pm 3.3\%$	$\pm 2\%$	$\pm 2.1\%$	$\pm 0.0\%$	$\pm 2\%$	$\pm 3.1\%$
Fac. Scale	$^{+13\%}_{-1\%}$	$^{+9\%}_{-4\%}$	$^{+3\%}_{-7\%}$	$^{+9\%}_{-11\%}$	$^{+10\%}_{-16\%}$	$^{+6\%}_{-1\%}$	$^{+31\%}_{-8\%}$
No. partons	$\pm 16\%$	$\pm 6\%$	$\pm 9\%$	$\pm 25\%$	$\pm 17\%$	$\pm 7\%$	$\pm 24\%$
W fraction	$\pm 6\%$	$\pm 4\%$	$\pm 1.8\%$	$\pm 6\%$	$\pm 3\%$	$\pm 3\%$	-
No re-weight	$\pm 27\%$	$\pm 25\%$	$\pm 1.6\%$	$\pm 31\%$	$\pm 31\%$	$\pm 0.3\%$	$\pm 52\%$

Error Source	6j80 SR	6j80 CR	6j80 TF	7j80 SR	7j80 CR	7j80 TF	8j80 SR
JES	$^{+34\%}_{-22\%}$	$^{+49\%}_{-24\%}$	$^{-10\%}_{+3.8\%}$	$^{+32\%}_{-16\%}$	$^{+59\%}_{-39\%}$	$^{-17\%}_{+37\%}$	$^{+24\%}_{-2\%}$
JER	$\pm 7\%$	$\pm 11\%$	$\pm 4\%$	$\pm 3\%$	$\pm 9\%$	$\pm 11\%$	$\pm 4\%$
Pile-Up	$\pm 1.3\%$	$\pm 0.7\%$	$\pm 0.6\%$	$\pm 1.1\%$	$\pm 6\%$	$\pm 7\%$	$\pm 10\%$
Fac. Scale	$^{-4\%}_{-3\%}$	$^{+8\%}_{-7\%}$	$^{+4\%}_{-11\%}$	$^{-24\%}_{-6\%}$	$^{+2\%}_{-17\%}$	$^{+12\%}_{-25\%}$	$^{+40\%}_{-0\%}$
No. partons	$\pm 12\%$	$\pm 5\%$	$\pm 6\%$	$\pm 4\%$	$\pm 18\%$	$\pm 27\%$	$\pm 29\%$
W fraction	$\pm 7\%$	$\pm 1\%$	$\pm 6\%$	$\pm 9\%$	$\pm 0\%$	$\pm 9\%$	-
No re-weight	$\pm 30\%$	$\pm 31\%$	$\pm 1\%$	$\pm 26\%$	$\pm 54\%$	$\pm 18\%$	$\pm 12\%$

Table 7.4: The different systematics on the $t\bar{t}$ and W backgrounds. The systematics on the control region (CR) and signal region (SR) are given as well as the uncertainty on the transfer factor (TF). This demonstrates how the use of control regions results in the reduction of systematic errors.

Finally the finite Monte-Carlo statistics lead to an additional uncertainty and when control regions are used for the normalisation, the statistical uncertainty on the finite number of observed events is also included.

7.8.3 Minor Backgrounds

Other minor backgrounds such as di-boson events, single top events and $t\bar{t}$ production in association with an additional vector boson were investigated using Monte-Carlo simulations and were all found to be negligible in comparison with the systematic uncertainties associated with the $t\bar{t}$, W+jets and Z+jets backgrounds.

7.8.4 Summary of the Standard Model Background

The methodology for the prediction of the Standard Model backgrounds has been presented. The method used to determine the multi-jet background relies on a data-driven estimation

and the uncertainties are dominated by the assumptions used in the method. The $t\bar{t}$ and W backgrounds are determined using control regions for normalisation for those signal regions with sufficient numbers of events, while the Monte-Carlo prediction is taken for the tightest regions. The small background from $Z(\rightarrow \nu\nu) +$ jets is taken from simulation. As the uncertainties on the multi-jet and "leptonic" backgrounds originate from different sources they are treated as independent when forming the total uncertainty.

7.9 Results and Interpretation

Figure 7.11 shows the $E_{\mathrm{T}}^{\mathrm{miss}}/\sqrt{H_{\mathrm{T}}}$ distribution after all cuts apart from the final cut on this variable. Very good agreement is seen in the lower $E_{\mathrm{T}}^{\mathrm{miss}}/\sqrt{H_{\mathrm{T}}}$ multi-jet control regions and above the final cut value of $4\,\mathrm{GeV}^{1/2}$ there is no evidence of new physics. The number of predicted and observed events in the six different signal regions are given in Table 7.5. Good agreement within the uncertainties is observed.

As no significant excess is observed limits can be set on new physics with the signature of high jet multiplicity and missing transverse momentum. Model independent limits at the 95% confidence level on the number of beyond the Standard Model events that can pass our cuts, $N_{\mathrm{BSM,max}}^{95\%}$, are given in Table 7.5. These can also be expressed as lower bounds on the allowed cross-section, $\sigma_{\mathrm{BSM,max}}^{95\%}$, multiplied by the acceptance, A, and efficiency, ϵ. These limits can be applied to any model provided the contamination from signal in the control regions used in the analysis is negligible and that the acceptance and efficiency can be estimated from simulation.

We also interpret the results in two planes of supersymmetric space. These limits include the experimental uncertainties on the signal points and the primary JES, JER and pile-up uncertainties are treated as correlated between signal and Standard Model processes. Figure 7.12 shows the limit in the simplified model where the squarks are all assumed to be beyond the reach of the LHC and gluino pair production is the only channel available. These are then assumed to decay as $\tilde{g} \rightarrow t + \bar{t} + \tilde{\chi}_1^0$, where $\tilde{\chi}_1^0$ is the lightest supersymmetric particle and is pure bino. A profile likelihood test in conjunction with the CL_s prescription [135] is used to test each point in the parameter space and therefore provide a 95% confidence limit exclusion region. The signal region with the best expected limit at each point in parameter space is used

Signal region	**7j55**	**8j55**	**9j55**	**6j80**	**7j80**	**8j80**
Multi-jets	219 ± 39	23 ± 7	2.8 ± 0.9	134 ± 32	12 ± 4	1.1 ± 0.4
$t\bar{t} \to q\ell, \ell\ell$ and $W(\to \ell\nu)+$jets	121^{+23}_{-25}	18 ± 8	$2.0^{+2.2}_{-1.3}$	97 ± 24	14^{+10}_{-12}	$1.8^{+1.7}_{-1.4}$
$Z(\to \nu\nu)$ + jets	13 ± 13	1 ± 1	$0^{+0.4}$	12 ± 12	2 ± 2	$0^{+0.4}$
Total Standard Model	353 ± 48	42 ± 10	$4.8^{+2.4}_{-1.6}$	243 ± 42	28^{+11}_{-12}	$2.9^{+1.8}_{-1.5}$
Data	381	48	3	248	26	1
$N^{95\%}_{\mathrm{BSM,max}}$ (exp)	101	24	7.3	88	26	5.5
$N^{95\%}_{\mathrm{BSM,max}}$ (obs)	122	29	5.4	91	25	4
$\sigma^{95\%}_{\mathrm{BSM,max}} \times A \times \epsilon$ (exp) [fb]	17.5	4.1	1.3	15.2	4.5	0.9
$\sigma^{95\%}_{\mathrm{BSM,max}} \times A \times \epsilon$ (obs) [fb]	21	5	0.9	15.7	4.3	0.7

Table 7.5: Results for each of the six signal regions for an integrated luminosity of 5.8 fb^{-1}. The expected numbers of Standard Model events are given for each of the following sources: multi-jet (including fully-hadronic $t\bar{t}$), semi- and fully-leptonic $t\bar{t}$ decays combined with W bosons in association with jets, Z bosons in association with jets, as well as the total Standard Model expectation. The uncertainties on the predictions are the combination of the statistical and systematic components. The numbers of observed events are also shown. The final four rows show the statistical quantities described in the text. Both the expected (exp) and the observed (obs) values are shown for $N^{95\%}_{\mathrm{BSM,max}}$ and $\sigma^{95\%}_{\mathrm{BSM,max}} \times A \times \epsilon$. *(These upper limits were computed by another member of the analysis team.)*

for the final limit. For large values of mass splitting between the gluino and LSP the signal region requiring ≥ 9 jets with $p_{\mathrm{T}} > 55\,\mathrm{GeV}$ provides the most stringent limit, while when the mass splitting of the gluino and LSP approaches the kinematic limit of the decay the signal region requiring ≥ 8 jets with $p_{\mathrm{T}} > 55\,\mathrm{GeV}$ becomes the most sensitive.

An additional interpretation is provided in a plane of the MSUGRA/CMSSM parameter space. The values of $\tan\beta$ and A_0 are set to 10 and 0 respectively, while μ is defined to be positive. In Figure 7.13 limits are then displayed in the m_0 and m_{12} plane. These are compared to the limits set in the same plane with the same analysis using the 7 TeV dataset recorded in 2011 and an analysis requiring $\geq 2-6$ jets with the same dataset as this analysis. In the region of high m_0 where gluino production is dominant this high multiplicity analysis provides the most stringent limits of all the ATLAS analyses providing a lower limit on the gluino mass in this plane of 1 TeV.

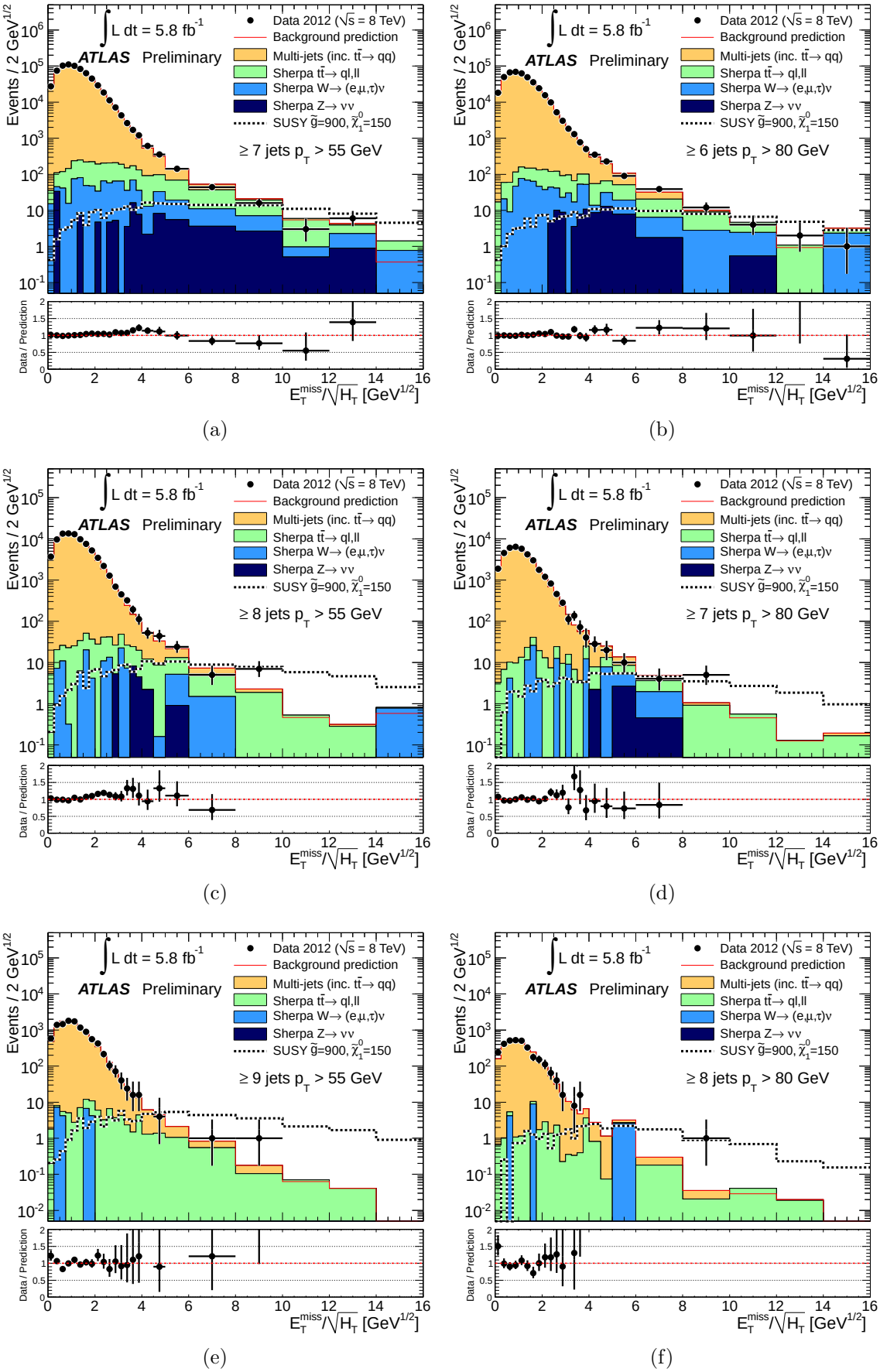

Figure 7.11: The $E_{\mathrm{T}}^{\mathrm{miss}}/\sqrt{H_{\mathrm{T}}}$ distributions for the six signal regions before the final cut of $E_{\mathrm{T}}^{\mathrm{miss}}/\sqrt{H_{\mathrm{T}}}$> 4 GeV$^{1/2}$.

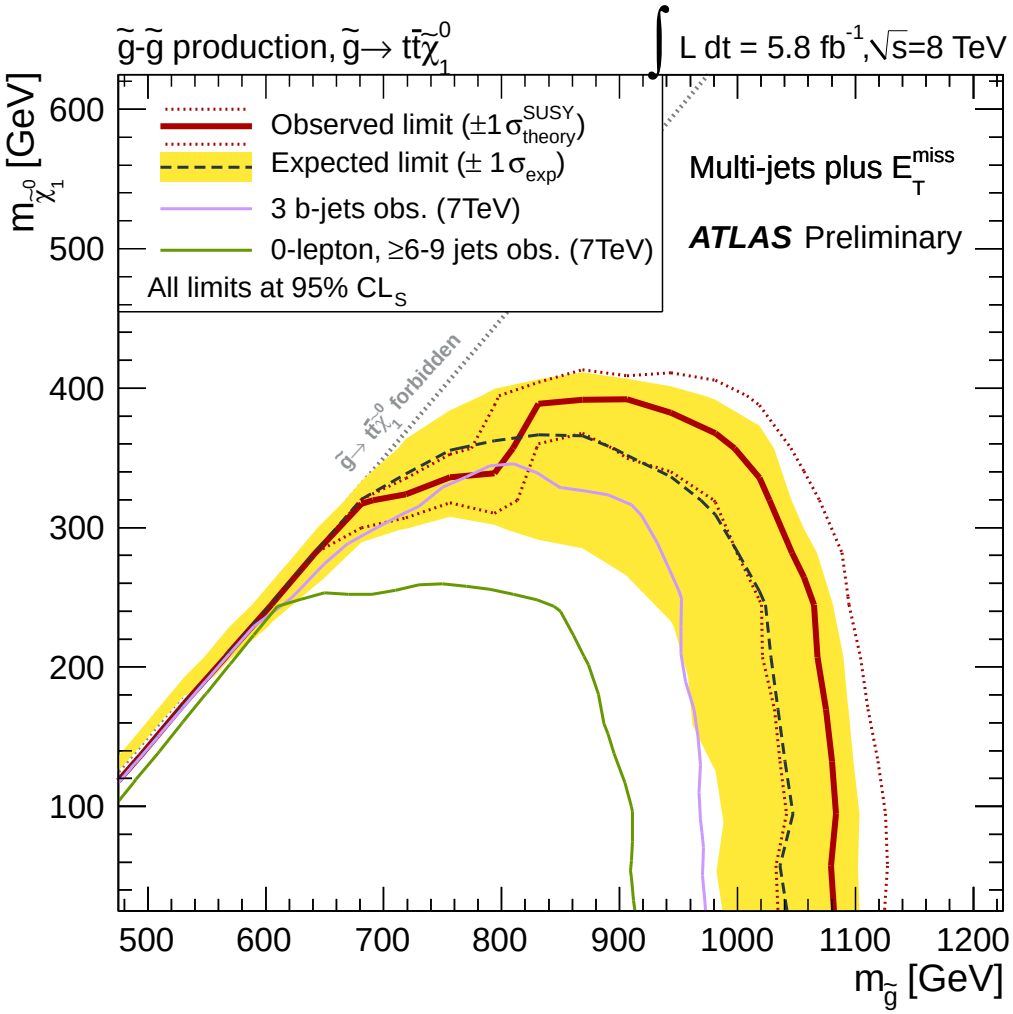

Figure 7.12: The limit from the most sensitive signal region in the plane of gluino mass against LSP mass with the assumed decay; $\tilde{g} \rightarrow t+\bar{t}+\tilde{\chi}_1^0$. The black dashed line gives the expected limit with the nominal theoretical cross-section for the signal model, with the yellow band giving the experimental uncertainty on this limit. The dark red curve shows the observed limit with the nominal theoretical cross-section and the dotted red curves gives the uncertainty range on the theoretical cross-section. The green curve is the observed limit from the previous version of this analysis using 4.7 fb^{-1} of 7 TeV data taken in 2011 [3]. The purple curve gives the observed limit from an analysis requiring ≥ 3 b-tagged jets using the same 2011 dataset [136].

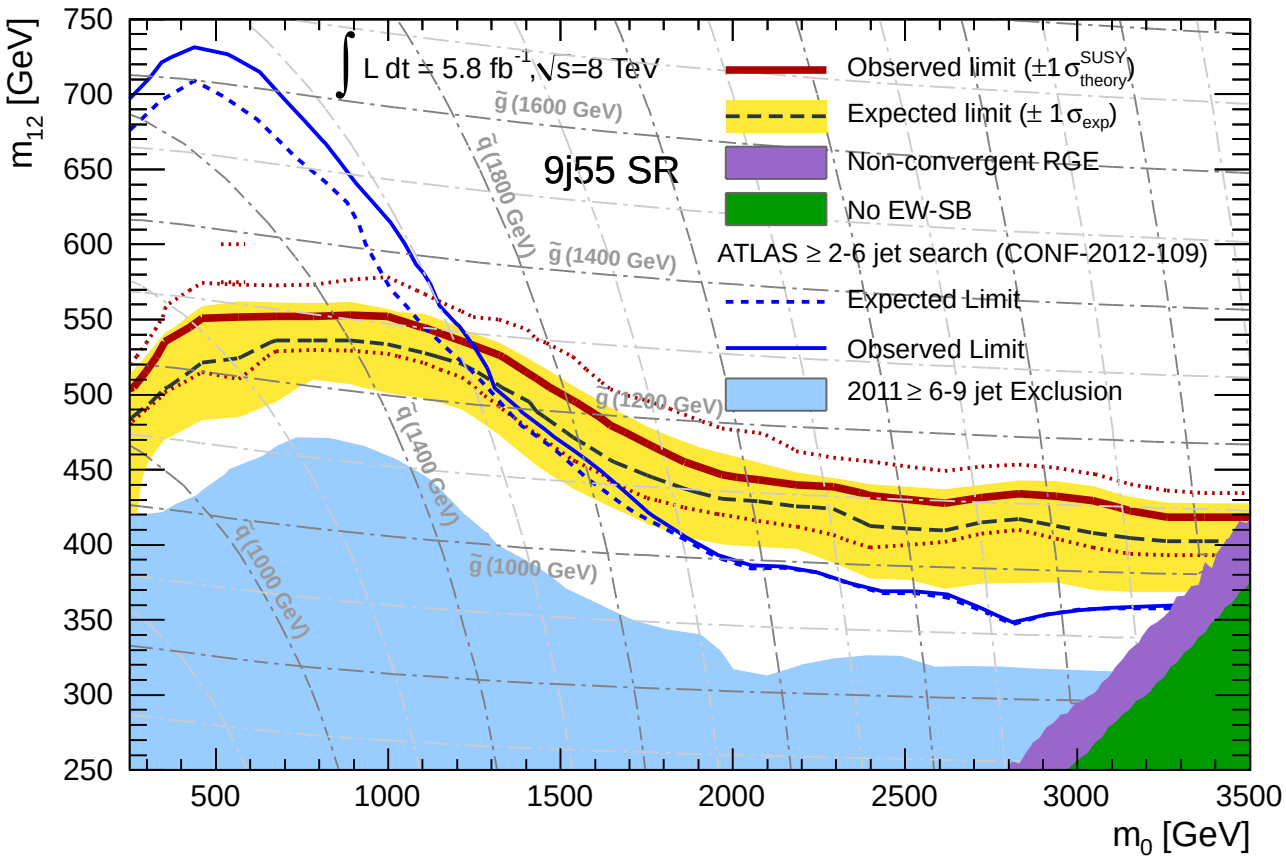

Figure 7.13: The limit in the MSUGRA/CMSSM plane with the same colour scheme as Figure 7.12. The blue shaded area shows the points excluded by the ATLAS multi-jets and missing transverse momentum analysis using 4.7 fb^{-1} of 7 TeV data recorded in 2011 [3]. The blue solid and dashed lines give the observed and expected limit from a search requiring $\geq 2-6$ jets using the same dataset as the search presented here [88].

Chapter 8

Summary of Constraints, Conclusion and Outlook

Since the switching on of the LHC in March 2010, the operation of both the accelerator and the ATLAS detector have been very successful. The collaboration rapidly re-discovered the Standard Model particles and these "standard candles" were then used to evaluate the performance of the detector. This has allowed the rapid production of analyses planned in advance of operations. Due to the LHC having a higher centre of mass operating energy than previous colliders the sensitivity after very little time exceeded the limits on coloured supersymmetric particles set by the Tevatron collider at Fermilab which were reviewed in §3. In §6 it was seen that the primary strategy of the initial searches followed that which was outlined prior to operations; requiring very large amounts of $E_{\mathrm{T}}^{\mathrm{miss}}$, some number of jets, a large ratio of the quantity $E_{\mathrm{T}}^{\mathrm{miss}}/m_{\mathrm{eff}}^{n}$, and a final cut on the variable m_{eff}^{n}, which is defined by the scalar sum of jets and missing energy in the event. With the non-discovery of Supersymmetry using this search strategy in the early data, it was desirable to look to see what signals could be missed by such searches. One such category of signals is the case when the decay chain is longer and/or through more massive Standard Model particles. In such cases more of the energy in the event is in the visible sector in the form of multiple jets such that the $E_{\mathrm{T}}^{\mathrm{miss}}$ is reduced and the previous strategy becomes non-optimal.

The primary subject of this thesis is the approach proposed and implemented by the author,

within the ATLAS Collaboration, to tackle these final states. Supersymmetry was introduced as a framework within which to motivate this search in §2 and the limits from previous searches prior to the operation of the LHC were presented in §3. The main features of the ATLAS detector were given in §4. Final states with many hard jets and $E_{\mathrm{T}}^{\mathrm{miss}}$ have Standard Model backgrounds of $t\bar{t}$ and W+jets where the lepton is either a hadronically decaying tau or the lepton is not identified, as well as Z+jets where the Z boson decays to neutrinos. The estimation of these backgrounds is aided by data but has to use Monte-Carlo simulations as well. The details of these simulated samples are given in §5. With the ingredients for LHC searches described, in §6 the other searches in the fully-hadronic channel were covered before the main analysis was approached in §7. Only the 2012, $5.8\,\mathrm{fb}^{-1}$ version of the analysis is described as it employed the same techniques as the early versions, with some improvements.

The analysis selection of high jet multiplcity and missing transerse momentum had two major types of background: those which are dominated by jet mis-measurement and those where prompt neutrinos from vector boson decays provide the majority of the $E_{\mathrm{T}}^{\mathrm{miss}}$. The evaluation of the latter sources of background employed the same technique as the majority of other ATLAS searches for Supersymmetry. Monte-Carlo simulations are found to describe the data well and are then used to determine the ratio between the number of expected events in control regions and the signal region, or just the expected number of events in the signal region. When the ratio is used then both theoretical and experimental uncertainties are reduced. This approach is used everywhere but the tightest signal regions where too few events are expected in the corresponding control regions. For the backgrounds dominated by jet mis-measurement a novel approach is developed using the distribution of the variable $E_{\mathrm{T}}^{\mathrm{miss}}/\sqrt{H_{\mathrm{T}}}$ in data for the determination of this background. This method allowed this background to be determined accurately for very high multiplicity such that this search could cut softer on the effective $E_{\mathrm{T}}^{\mathrm{miss}}$.

The search yielded no significant excess over the Standard Model expectation. It therefore was possible to constrain the models of Supersymmetry that could be physically realised. Two different example planes of supersymmetric phase space were used to display the strength of the search. In a simplified model of pair produced gluinos which decayed through off-shell stop quarks to the $t + \bar{t} + \tilde{\chi}_1^0$ final state models were excluded with gluinos lighter than 1 TeV

provided the bino is lighter than 300 GeV. Secondly, the results were interpreted in a plane of MSUGRA/CMSSM which has been used by several other previous searches. In the particular plane chosen with $\tan\beta = 10$, $A_0 = 0$, $\mu > 0$ gluinos are excluded for masses below 1 TeV. With the dataset considered here these are the strongest limits in much of the simplified model space and the strongest at high m_0 in the plane of MSUGRA/CMSSM.

Prior to the operation of the LHC the theoretical prejudice lay with the expectation that Supersymmetric particles would be lighter than 1 TeV. This is becoming increasingly unlikely in constrained models such as MSUGRA/CMSSM as more and more of the parameter space is covered by searches like this one. From the limits set by these searches general fits in these constrained models are developing some tension with the experimental data [54, 55]. However, in more general frameworks such as the pMSSM there still exist regions of parameter space that have low fine tuning and that are not excluded by LHC searches or other constraints [137]. It is therefore the case that while searches like that presented here have reduced the possible parameter space, Supersymmetry is still a viable, natural theory that would be able to solve the hierarchy problem.

In 2012 ATLAS has recorded 21.7 fb^{-1} of 8 TeV data and this search will be updated with this larger dataset which will extend the sensitivity. Furthermore, knowledge and understanding of both the ATLAS detector and methods used to reduce the Standard Model backgrounds are constantly improving such that it can be expected that sensitivity to new physics models that lie beyond the Standard Model will improve with time. Finally, in 2015 the LHC will start to deliver luminosity at the much higher centre of mass energy of 13 TeV such that the reach of searches for Supersymmetric particles will be much increased. For example, the cross-section for pair production of gluinos of mass 1.2 TeV is almost a factor of twenty higher for a centre of mass collision energy of 13 TeV compared to 8 TeV [129, 130]. Therefore, while this search (and other LHC searches) have introduced tension in some constrained models, in more general frameworks Supersymmetry remains alive and the search prospects for such models in the near future are also bright.

Bibliography

[1] The ATLAS Collaboration, *Search for new phenomena using large jet multiplicities and missing transverse momentum with ATLAS in 5.8 fb^{-1} of $\sqrt{s} = 8$ TeV proton-proton collisions*, . ATLAS-CONF-2012-103.

[2] The ATLAS Collaboration, *Search for new phenomena in final states with large jet multiplicities and missing transverse momentum using $\sqrt{s} = 7$ TeV pp collisions with the ATLAS detector*, JHEP **1111** (2011) 099, arXiv:1110.2299 [hep-ex].

[3] The ATLAS Collaboration, *Hunt for new phenomena using large jet multiplicities and missing transverse momentum with ATLAS in 4.7 fb^{-1} of $\sqrt{s} = 7$ TeV proton-proton collisions*, JHEP **1207** (2012) 167, arXiv:1206.1760 [hep-ex].

[4] The Atlas Collaboration, *Search for squarks and gluinos using final states with jets and missing transverse momentum with the ATLAS detector in $\sqrt{s} = 7$ TeV proton-proton collisions*, Phys.Lett. **B701** (2011) 186–203, arXiv:1102.5290 [hep-ex].

[5] The ATLAS Collaboration, *Search for squarks and gluinos using final states with jets and missing transverse momentum with the ATLAS detector in $\sqrt{(s)} = 7$ TeV proton-proton collisions*, . ATLAS-CONF-2011-086.

[6] The ATLAS Collaboration, *Search for squarks and gluinos using final states with jets and missing transverse momentum with the ATLAS detector in $\sqrt{s} = 7$ TeV proton-proton collisions*, Phys.Lett. **B710** (2012) 67–85, arXiv:1109.6572 [hep-ex].

[7] A. Barr, C. Gwenlan, C. Lester, and C. Young, *A comment on 'Amplification of endpoint structure for new particle mass measurement at the LHC'*, Phys.Rev. **D83** (2011) 118701, `arXiv:1006.2568 [hep-ex]`.

[8] The ATLAS Collaboration, *The ATLAS experiment at the CERN Large Hadron Collider*, JINST **3** (2008) S08003.

[9] The CMS Collaboration, *The CMS experiment at the CERN LHC*, JINST **3** (2008) S08004.

[10] H. Miyazawa, *Baryon number changing currents*, Prog. Theor. Phys. **36 (6)** (1966) 1266–1276.

P. Ramond, *Dual theory for free fermions*, Phys.Rev. **D3** (1971) 2415–2418.

Y. Golfand and E. Likhtman, *Extension of the algebra of Poincaré group generators and violation of p invariance*, JETP Lett. **13** (1971) 323–326.

A. Neveu and J. Schwarz, *Factorizable dual model of pions*, Nucl.Phys. **B31** (1971) 86–112.

A. Neveu and J. Schwarz, *Quark model of dual pions*, Phys.Rev. **D4** (1971) 1109–1111.

J.-L. Gervais and B. Sakita, *Field theory interpretation of supergauges in dual models*, Nucl.Phys. **B34** (1971) 632–639.

D. Volkov and V. Akulov, *Is the neutrino a Goldstone particle?*, Phys.Lett. **B46** (1973) 109–110.

J. Wess and B. Zumino, *A Lagrangian model invariant under supergauge transformations*, Phys.Lett. **B49** (1974) 52.

J. Wess and B. Zumino, *Supergauge transformations in four dimensions*, Nucl.Phys. **B70** (1974) 39–50.

P. Fayet, *Supersymmetry and weak, electromagnetic and strong interactions*, Phys.Lett. **B64** (1976) 159.

P. Fayet, *Spontaneously broken supersymmetric theories of weak, electromagnetic and strong interactions*, Phys.Lett. **B69** (1977) 489.

G. R. Farrar and P. Fayet, *Phenomenology of the production, decay, and detection of new hadronic states associated with supersymmetry*, Phys.Lett. **B76** (1978) 575–579.

P. Fayet, *Relations between the masses of the superpartners of leptons and quarks, the Goldstino couplings and the neutral currents*, Phys.Lett. **B84** (1979) 416.

S. Dimopoulos and H. Georgi, *Softly broken supersymmetry and SU(5)*, Nucl.Phys. **B193** (1981) 150.

[11] The Super-Kamiokande Collaboration, *Search for Proton Decay via $p \to e^+\pi^0$ and $p \to \mu^+\pi^0$ in a Large Water Cherenkov Detector*, Phys.Rev.Lett. **102** (2009) 141801, arXiv:0903.0676 [hep-ex].

[12] The Super-Kamiokande Collaboration, *Search for Nucleon Decay into Charged Anti-lepton plus Meson in Super-Kamiokande I and II*, Phys.Rev. **D85** (2012) 112001, arXiv:1203.4030 [hep-ex].

[13] T. Yamagata, Y. Takamori, and H. Utsunomiya, *Search for anomalously heavy hydrogen in deep sea water at 4000-m*, Phys.Rev. **D47** (1993) 1231–1234.

[14] P. Smith, J. Bennett, G. Homer, J. Lewin, H. Walford, et al., *A Search for Anomalous Hydrogen in Enriched D_2 O, using a time-of-flight Spectrometer*, Nucl.Phys. **B206** (1982) 333–348.

[15] T. Hemmick, D. Elmore, T. Gentile, P. Kubik, S. Olsen, et al., *A Search for Anomalously Heavy Isotopes of low Z nuclei*, Phys.Rev. **D41** (1990) 2074–2080.

[16] P. Verkerk, G. Grynberg, B. Pichard, M. Spiro, S. Zylberajch, et al., *Search for superheavy hydrogen in sea water*, Phys.Rev.Lett. **68** (1992) 1116–1119.

[17] E. Norman, R. Chadwick, K. Lesko, R. Larimer, and D. Hoffman, *Search for supermassive Cahn-Glashow particles in lead*, Phys.Rev. **D39** (1989) 2499.

[18] F. Zwicky, *Spectral displacement of extra galactic nebulae*, Helv.Phys.Acta **6** (1933) 110–127.

[19] V. C. Rubin and J. Ford, W. Kent, *Rotation of the Andromeda Nebula from a Spectroscopic Survey of Emission Regions*, Astrophys.J. **159** (1970) 379–403.

[20] V. Rubin, N. Thonnard, and J. Ford, W.K., *Rotational properties of 21 SC galaxies with a large range of luminosities and radii, from NGC 4605 /R = 4kpc/ to UGC 2885 /R = 122 kpc/*, Astrophys.J. **238** (1980) 471.

[21] A. Bosma, *21-cm line studies of spiral galaxies. 2. The distribution and kinematics of neutral hydrogen in spiral galaxies of various morphological types.*, Astron.J. **86** (1981) 1825.

[22] A. Refregier, *Weak gravitational lensing by large scale structure*, Ann.Rev.Astron.Astrophys. **41** (2003) 645–668, arXiv:astro-ph/0307212 [astro-ph].

[23] J. A. Tyson, G. P. Kochanski, and I. P. Dell'Antonio, *Detailed mass map of CL0024+1654 from strong lensing*, Astrophys.J. **498** (1998) L107, arXiv:astro-ph/9801193 [astro-ph].

[24] A. D. Lewis, D. A. Buote, and J. T. Stocke, *Chandra observations of Abell 2029: The Dark matter profile down to $<0.01R_{VIR}$ in an unusually relaxed cluster*, Astrophys.J. **586** (2003) 135–142, arXiv:astro-ph/0209205 [astro-ph].

[25] D. Clowe, M. Bradac, A. H. Gonzalez, M. Markevitch, S. W. Randall, et al., *A direct empirical proof of the existence of dark matter*, Astrophys.J. **648** (2006) L109–L113, arXiv:astro-ph/0608407 [astro-ph].

[26] B. Fields and S. Sarkar, *Big-Bang nucleosynthesis (2006 Particle Data Group mini-review)*, arXiv:astro-ph/0601514 [astro-ph].

[27] S. Allen, A. Fabian, R. Schmidt, and H. Ebeling, *Cosmological constraints from the local x-ray luminosity function of the most x-ray luminous galaxy clusters*, Mon.Not.Roy.Astron.Soc. **342** (2003) 287, arXiv:astro-ph/0208394 [astro-ph].

[28] Supernova Search Team, A. G. Riess et al., *Observational evidence from supernovae for an accelerating universe and a cosmological constant*, Astron.J. **116** (1998) 1009–1038, arXiv:astro-ph/9805201 [astro-ph].

[29] Supernova Cosmology Project, S. Perlmutter et al., *Measurements of Omega and Lambda from 42 high redshift supernovae*, Astrophys.J. **517** (1999) 565–586, arXiv:astro-ph/9812133 [astro-ph].

[30] The WMAP Collaboration, *Seven-Year Wilkinson Microwave Anisotropy Probe (WMAP) Observations: Cosmological Interpretation*, Astrophys.J.Suppl. **192** (2011) 18, arXiv:1001.4538 [astro-ph.CO].

[31] T. Falk, K. A. Olive, and M. Srednicki, *Heavy sneutrinos as dark matter*, Phys.Lett. **B339** (1994) 248–251, arXiv:hep-ph/9409270 [hep-ph].

[32] C. Arina and N. Fornengo, *Sneutrino cold dark matter, a new analysis: Relic abundance and detection rates*, JHEP **0711** (2007) 029, arXiv:0709.4477 [hep-ph].

[33] M. E. Peskin and D. V. Schroeder, *An Introduction to quantum field theory*, .

[34] The ATLAS Collaboration, *Observation of a new particle in the search for the Standard Model Higgs boson with the ATLAS detector at the LHC*, Phys.Lett. **B716** (2012) 1–29, arXiv:1207.7214 [hep-ex].

[35] The CMS Collaboration, *Observation of a new boson at a mass of 125 GeV with the CMS experiment at the LHC*, Phys.Lett. **B716** (2012) 30–61, arXiv:1207.7235 [hep-ex].

[36] The MuLan Collaboration, *Improved measurement of the positive muon lifetime and determination of the Fermi constant*, Phys.Rev.Lett. **99** (2007) 032001, arXiv:0704.1981 [hep-ex].

[37] ALEPH Collaboration, DELPHI Collaboration, L3 Collaboration, OPAL Collaboration, SLD Collaboration, LEP Electroweak Working Group, SLD Electroweak Group, SLD

Heavy Flavour Group, *Precision electroweak measurements on the Z resonance*, Phys.Rept. **427** (2006) 257–454, arXiv:hep-ex/0509008 [hep-ex].

[38] Tevatron Electroweak Working Group, *Combination of CDF and D0 Results on the Width of the W boson*, arXiv:1003.2826 [hep-ex].

[39] M. Davier, A. Hoecker, B. Malaescu, and Z. Zhang, *Reevaluation of the Hadronic Contributions to the Muon g-2 and to alpha(MZ)*, Eur.Phys.J. **C71** (2011) 1515, arXiv:1010.4180 [hep-ph].

[40] M. Baak, M. Goebel, J. Haller, A. Hoecker, D. Kennedy, et al., *The Electroweak Fit of the Standard Model after the Discovery of a New Boson at the LHC*, arXiv:1209.2716 [hep-ph].

[41] CDF Collaboration, D0 Collaboration, *Combination of the top-quark mass measurements from the Tevatron collider*, arXiv:1207.1069 [hep-ex].

[42] CDF Collaboration, D0 Collaboration, Tevatron Electroweak Working Group, *2012 Update of the Combination of CDF and D0 Results for the Mass of the W Boson*, arXiv:1204.0042 [hep-ex].

[43] ATLAS Collaboration, G. Aad et al., *ATLAS search for new phenomena in dijet mass and angular distributions using pp collisions at* $\sqrt{s} = 7\ TeV$, JHEP **1301** (2013) 029, arXiv:1210.1718 [hep-ex].

[44] S. R. Coleman and J. Mandula, *ALL POSSIBLE SYMMETRIES OF THE S MATRIX*, Phys.Rev. **159** (1967) 1251–1256.

[45] R. Haag, J. T. Lopuszanski, and M. Sohnius, *All Possible Generators of Supersymmetries of the s Matrix*, Nucl.Phys. **B88** (1975) 257.

[46] S. P. Martin, *A Supersymmetry primer*, arXiv:hep-ph/9709356 [hep-ph].

[47] Y. Kao and T. Takeuchi, *Single-Coupling Bounds on R-parity violating Supersymmetry, an update*, arXiv:0910.4980 [hep-ph].

[48] H. E. Haber, R. Hempfling, and A. H. Hoang, *Approximating the radiatively corrected Higgs mass in the minimal supersymmetric model*, Z.Phys. **C75** (1997) 539–554, arXiv:hep-ph/9609331 [hep-ph].

[49] M. Papucci, J. T. Ruderman, and A. Weiler, *Natural SUSY Endures*, JHEP **1209** (2012) 035, arXiv:1110.6926 [hep-ph].

[50] M. W. Cahill-Rowley, J. L. Hewett, A. Ismail, and T. G. Rizzo, *The Higgs Sector and Fine-Tuning in the pMSSM*, Phys.Rev. **D86** (2012) 075015, arXiv:1206.5800 [hep-ph].

[51] U. Ellwanger, C. Hugonie, and A. M. Teixeira, *The Next-to-Minimal Supersymmetric Standard Model*, Phys.Rept. **496** (2010) 1–77, arXiv:0910.1785 [hep-ph].

[52] A. H. Chamseddine, R. L. Arnowitt, and P. Nath, *Locally Supersymmetric Grand Unification*, Phys.Rev.Lett. **49** (1982) 970.

R. Barbieri, S. Ferrara, and C. A. Savoy, *Gauge Models with Spontaneously Broken Local Supersymmetry*, Phys. Lett. **B119** (1982) 343.

L. E. Ibanez, *Locally supersymmetric SU(5) Grand Unification*, Phys.Lett. **B118** (1982) 73.

L. J. Hall, J. D. Lykken, and S. Weinberg, *Supergravity as the messenger of supersymmetry breaking*, Phys.Rev. **D27** (1983) 2359–2378.

N. Ohta, *Grand Unified Theories based on local supersymmetry*, Prog.Theor.Phys. **70** (1983) 542.

[53] G. L. Kane, C. F. Kolda, L. Roszkowski, and J. D. Wells, *Study of constrained minimal supersymmetry*, Phys.Rev. **D49** (1994) 6173–6210, arXiv:hep-ph/9312272.

[54] O. Buchmueller, R. Cavanaugh, M. Citron, A. De Roeck, M. Dolan, et al., *The CMSSM and NUHM1 in Light of 7 TeV LHC, Bs to mu+mu- and XENON100 Data*, arXiv:1207.7315 [hep-ph].

[55] P. Bechtle, T. Bringmann, K. Desch, H. Dreiner, M. Hamer, et al., *Constrained Supersymmetry after two years of LHC data: a global view with Fittino*, JHEP **1206** (2012) 098, arXiv:1204.4199 [hep-ph].

[56] MSSM Working Group, A. Djouadi et al., *The Minimal supersymmetric standard model: Group summary report*, arXiv:hep-ph/9901246 [hep-ph].

[57] The OPAL Collaboration, *The OPAL detector at LEP*, Nucl.Instrum.Meth. **A305** (1991) 275–319.

[58] The ALEPH Collaboration, *ALEPH: A detector for electron-positron annnihilations at LEP*, Nucl.Instrum.Meth. **A294** (1990) 121–178.

[59] The DELPHI Collaboration, *The DELPHI detector at LEP*, Nucl.Instrum.Meth. **A303** (1991) 233–276.

[60] The L3 Collaboration, *The Construction of the L3 Experiment*, Nucl.Instrum.Meth. **A289** (1990) 35–102.

[61] LEPSUSYWG, ALEPH, DELPHI, L3 and OPAL experiments, *Combined LEP Chargino Results, up to 208 GeV for large m0*, LEPSUSYWG/01-03.1. (http://lepsusy.web.cern.ch/lepsusy/Welcome.html).

[62] LEPSUSYWG, ALEPH, DELPHI, L3 and OPAL experiments, *Combined LEP Chargino Results, up to 208 GeV for low DM*, LEPSUSYWG/02-04.1. (http://lepsusy.web.cern.ch/lepsusy/Welcome.html).

[63] LEPSUSYWG, ALEPH, DELPHI, L3 and OPAL experiments, *Combined LEP Selectron/Smuon/Stau Results, 183-208 GeV*, LEPSUSYWG/04-01.1. (http://lepsusy.web.cern.ch/lepsusy/Welcome.html).

[64] LEPSUSYWG, ALEPH, DELPHI, L3 and OPAL experiments, *Combined LEP stop and sbottom Results 183-208 GeV*, LEPSUSYWG/04-02.1. (http://lepsusy.web.cern.ch/lepsusy/Welcome.html).

[65] The CDF Collaboration, *The CDF Detector: An Overview*, Nucl.Instrum.Meth. **A271** (1988) 387–403.

[66] The D0 Collaboration, *The D0 Detector*, Nucl.Instrum.Meth. **A338** (1994) 185–253.

[67] The CDF Collaboration, *Inclusive Search for Squark and Gluino Production in $p\bar{p}$ Collisions at $\sqrt{s}$ = 1.96-TeV*, Phys.Rev.Lett. **102** (2009) 121801, arXiv:0811.2512 [hep-ex].

[68] The D0 Collaboration, *Search for squarks and gluinos in events with jets and missing transverse energy using 2.1 fb^{-1} of $p\bar{p}$ collision data at $\sqrt{s}$ = 1.96- TeV*, Phys.Lett. **B660** (2008) 449–457, arXiv:0712.3805 [hep-ex].

[69] The D0 Collaboration, *Search for scalar top quarks in the acoplanar charm jets and missing transverse energy final state in $p\bar{p}$ collisions at $\sqrt{s}$ = 1.96-TeV*, Phys.Lett. **B665** (2008) 1–8, arXiv:0803.2263 [hep-ex].

[70] The CDF Collaboration, *Search for Scalar Top Quark Production in $p\bar{p}$ Collisions at $\sqrt{s} = 1.96$ TeV*, JHEP **1210** (2012) 158, arXiv:1203.4171 [hep-ex].

[71] The CDF Collaboration, *Search for Pair Production of Supersymmetric Top Quarks in Dilepton Events from p anti-p Collisions at S**(1/2) = 1.96 TeV*, Phys.Rev.Lett. **104** (2010) 251801, arXiv:0912.1308 [hep-ex].

[72] The CDF Collaboration, *Search for the Production of Scalar Bottom Quarks in $p\bar{p}$ collisions at $\sqrt{s}$ = 1.96 TeV*, Phys.Rev.Lett. **105** (2010) 081802, arXiv:1005.3600 [hep-ex].

[73] The D0 Collaboration, *Search for scalar bottom quarks and third-generation leptoquarks in pp^- bar collisions at $\sqrt{s} = 1.96$ TeV*, Phys.Lett. **B693** (2010) 95–101, arXiv:1005.2222 [hep-ex].

[74] Heavy Flavor Averaging Group, Y. Amhis et al., *Averages of b-hadron, c-hadron, and tau-lepton properties as of early 2012*, arXiv:1207.1158 [hep-ex].

[75] The LHCb collaboration, *First evidence for the decay Bs $\to \mu^+\mu^-$*, arXiv:1211.2674 [hep-ex].

[76] E. De Rafael, *Present Status of the Muon Anomalous Magnetic Moment*, Nucl.Phys.Proc.Suppl. **186** (2009) 211–217, arXiv:0809.3085 [hep-ph].

[77] B. Allanach, *SOFTSUSY: a program for calculating supersymmetric spectra*, Comput.Phys.Commun. **143** (2002) 305–331, arXiv:hep-ph/0104145 [hep-ph].

[78] A. Djouadi, M. Muhlleitner, and M. Spira, *Decays of supersymmetric particles: The Program SUSY-HIT (SUspect-SdecaY-Hdecay-InTerface)*, Acta Phys.Polon. **B38** (2007) 635–644, arXiv:hep-ph/0609292 [hep-ph].

[79] G. Belanger, F. Boudjema, P. Brun, A. Pukhov, S. Rosier-Lees, et al., *Indirect search for dark matter with micrOMEGAs2.4* , Comput.Phys.Commun. **182** (2011) 842–856, arXiv:1004.1092 [hep-ph].

[80] The ATLAS Collaboration, *ATLAS: Detector and physics performance technical design report. Volume 1* , .

The ATLAS Collaboration, *ATLAS: Detector and physics performance technical design report. Volume 2* , .

[81] *https://twiki.cern.ch/twiki/bin/view/AtlasPublic*, June, 2013.

[82] *ATLAS tile calorimeter: Technical Design Report*. Technical Design Report ATLAS. CERN, Geneva, 1996.

[83] W. Lampl, S. Laplace, D. Lelas, P. Loch, H. Ma, S. Menke, S. Rajagopalan, D. Rousseau, S. Snyder, and G. Unal, *Calorimeter Clustering Algorithms: Description and Performance*, Tech. Rep. ATL-LARG-PUB-2008-002. ATL-COM-LARG-2008-003, CERN, Geneva, Apr, 2008.

[84] The ATLAS Collaboration, *Probing the measurement of jet energies with the ATLAS detector using Z+jet events from proton-proton collisions at $\sqrt{s} = 7\ TeV$* , . ATLAS-CONF-2012-053.

The ATLAS Collaboration, *Probing the measurement of jet energies with the ATLAS detector using photon+jet events in proton-proton collisions at* $\sqrt{s} = 7$ *TeV*, . ATLAS-CONF-2012-063.

The ATLAS Collaboration, *In situ jet pseudorapidity intercalibration of the ATLAS detector using dijet events in* $\sqrt{s} = 7$ *TeV proton-proton 2011 data*, . ATLAS-CONF-2012-124.

[85] The ATLAS Collaboration, *Pile-up corrections for jets from proton-proton collisions at* $\sqrt{s} = 7$ *TeV in ATLAS in 2011*, . ATLAS-CONF-2012-064.

[86] The ATLAS Collaboration, *Jet energy measurement with the ATLAS detector in proton-proton collisions at* $\sqrt{s} = 7$ *TeV*, arXiv:1112.6426 [hep-ex].

[87] C. Issever, K. Borras, and D. Wegener, *An Improved weighting algorithm to achieve software compensation in a fine grained LAr calorimeter*, Nucl.Instrum.Meth. **A545** (2005) 803–812, arXiv:physics/0408129 [physics].

[88] The ATLAS Collaboration, *Search for squarks and gluinos with the ATLAS detector using final states with jets and missing transverse momentum and 5.8* fb^{-1} *of* $\sqrt{(s)} = 8$ *TeV proton-proton collision data*, . ATLAS-CONF-2012-109.

[89] P. Nason, *A New method for combining NLO QCD with shower Monte Carlo algorithms*, JHEP **0411** (2004) 040, arXiv:hep-ph/0409146 [hep-ph].

S. Frixione, P. Nason, and C. Oleari, *Matching NLO QCD computations with Parton Shower simulations: the POWHEG method*, JHEP **0711** (2007) 070, arXiv:0709.2092 [hep-ph].

[90] S. Frixione and B. R. Webber, *Matching NLO QCD computations and parton shower simulations*, JHEP **0206** (2002) 029, arXiv:hep-ph/0204244 [hep-ph].

S. Frixione, P. Nason, and B. R. Webber, *Matching NLO QCD and parton showers in heavy flavor production*, JHEP **0308** (2003) 007, arXiv:hep-ph/0305252 [hep-ph].

[91] C. Berger, Z. Bern, L. Dixon, F. Febres Cordero, D. Forde, et al., *An Automated Implementation of On-Shell Methods for One-Loop Amplitudes*, Phys.Rev. **D78** (2008) 036003, arXiv:0803.4180 [hep-ph].

[92] G. Cullen, N. Greiner, G. Heinrich, G. Luisoni, P. Mastrolia, et al., *Automated One-Loop Calculations with GoSam*, Eur.Phys.J. **C72** (2012) 1889, arXiv:1111.2034 [hep-ph].

[93] F. Cascioli, P. Maierhofer, and S. Pozzorini, *Scattering Amplitudes with Open Loops*, Phys.Rev.Lett. **108** (2012) 111601, arXiv:1111.5206 [hep-ph].

[94] S. Hoeche, F. Krauss, M. Schonherr, and F. Siegert, *QCD matrix elements + parton showers: The NLO case*, arXiv:1207.5030 [hep-ph].

[95] T. Gehrmann, S. Hoche, F. Krauss, M. Schonherr, and F. Siegert, *NLO QCD matrix elements + parton showers in $e^+e^- \to$ hadrons*, arXiv:1207.5031 [hep-ph].

[96] K. Hamilton and P. Nason, *Improving NLO-parton shower matched simulations with higher order matrix elements*, JHEP **1006** (2010) 039, arXiv:1004.1764 [hep-ph].

[97] S. Hoche, F. Krauss, M. Schonherr, and F. Siegert, *NLO matrix elements and truncated showers*, JHEP **1108** (2011) 123, arXiv:1009.1127 [hep-ph].

[98] M. L. Mangano, M. Moretti, and R. Pittau, *Multijet matrix elements and shower evolution in hadronic collisions: $Wb\bar{b}$ + n jets as a case study*, Nucl.Phys. **B632** (2002) 343–362, arXiv:hep-ph/0108069 [hep-ph].

[99] M. L. Mangano, M. Moretti, F. Piccinini, and M. Treccani, *Matching matrix elements and shower evolution for top-quark production in hadronic collisions*, JHEP **0701** (2007) 013, arXiv:hep-ph/0611129 [hep-ph].

[100] S. Catani, F. Krauss, R. Kuhn, and B. Webber, *QCD matrix elements + parton showers*, JHEP **0111** (2001) 063, arXiv:hep-ph/0109231 [hep-ph].

[101] F. Krauss, *Matrix elements and parton showers in hadronic interactions*, JHEP **0208** (2002) 015, arXiv:hep-ph/0205283 [hep-ph].

[102] T. Gleisberg et al., *Event generation with SHERPA 1.1*, JHEP **02** (2009) 007, arXiv:0811.4622.

[103] S. Hoeche, F. Krauss, S. Schumann, and F. Siegert, *QCD matrix elements and truncated showers*, JHEP **0905** (2009) 053, arXiv:0903.1219 [hep-ph].

[104] S. Schumann and F. Krauss, *A Parton shower algorithm based on Catani-Seymour dipole factorisation*, JHEP **0803** (2008) 038, arXiv:0709.1027 [hep-ph].

[105] S. Catani and M. Seymour, *A General algorithm for calculating jet cross-sections in NLO QCD*, Nucl.Phys. **B485** (1997) 291–419, arXiv:hep-ph/9605323 [hep-ph].

Z. Nagy and D. E. Soper, *Matching parton showers to NLO computations*, JHEP **0510** (2005) 024, arXiv:hep-ph/0503053 [hep-ph].

Z. Nagy and D. E. Soper, *A New parton shower algorithm: Shower evolution, matching at leading and next-to-leading order level*, arXiv:hep-ph/0601021 [hep-ph].

[106] M. Bahr et al., *Herwig++ physics and manual*, Eur. Phys. J. **C58** (2008) 639–707, arXiv:0803.0883.

[107] The ATLAS Collaboration, *The ATLAS simulation infrastructure*, Eur. Phys. J. **C70** (2010) 823–874, arXiv:1005.4568 [physics.ins-det].

[108] GEANT4, S. Agostinelli et al., *GEANT4: A simulation toolkit*, Nucl. Instrum. Meth. **A506** (2003) 250–303.

[109] The ATLAS Collaboration, *Expected Performance of the ATLAS Experiment - Detector, Trigger and Physics*, arXiv:0901.0512 [hep-ex].

[110] The ATLAS Collaboration, *Search for squarks and gluinos with the ATLAS detector in final states with jets and missing transverse momentum using 4.7 fb^{-1} of $\sqrt{s} = 7$ TeV proton-proton collision data*, arXiv:1208.0949 [hep-ex].

[111] P. Svantesson, A. Belyaev, J. P. Hall, and S. F. King, *E6SSM vs MSSM Gluino Phenomenology*, EPJ Web Conf. **28** (2012) 12014, arXiv:1201.5141 [hep-ph].

[112] S. Akula, N. Chen, D. Feldman, M. Liu, Z. Liu, et al., *Interpreting the First CMS and ATLAS SUSY Results*, Phys.Lett. **B699** (2011) 377–382, arXiv:1103.1197 [hep-ph].

S. Akula, D. Feldman, Z. Liu, P. Nath, and G. Peim, *New Constraints on Dark Matter from CMS and ATLAS Data*, Mod.Phys.Lett. **A26** (2011) 1521–1535, arXiv:1103.5061 [hep-ph].

T. Li, J. A. Maxin, D. V. Nanopoulos, and J. W. Walker, *The Ultra-High Jet Multiplicity Signal of Stringy No-Scale F-SU(5) at the $\sqrt{s}$ = 7 TeV LHC*, Phys.Rev. **D84** (2011) 076003, arXiv:1103.4160 [hep-ph].

D. Feldman, G. Kane, E. Kuflik, and R. Lu, *A new (string motivated) approach to the little hierarchy problem*, Phys.Lett. **B704** (2011) 56–61, arXiv:1105.3765 [hep-ph].

[113] The ATLAS Collaboration, *Further search for supersymmetry at $\sqrt{s} = 7$ TeV in final states with jets, missing transverse momentum and isolated leptons with the ATLAS detector*, Phys.Rev. **D86** (2012) 092002, arXiv:1208.4688 [hep-ex].

[114] The ATLAS Collaboration, *Search for supersymmetry at $\sqrt{(s)} = 7$ TeV in final states with large jet multiplicity, missing transverse momentum and one isolated lepton with the ATLAS detector*, . ATLAS-CONF-2012-140.

[115] M. Cacciari, G. P. Salam, and G. Soyez, *The Anti-k(t) jet clustering algorithm*, JHEP **0804** (2008) 063, arXiv:0802.1189 [hep-ph].

M. Cacciari and G. P. Salam, *Dispelling the N^3 myth for the k_t jet-finder*, Phys.Lett. **B641** (2006) 57–61, arXiv:hep-ph/0512210 [hep-ph].

[116] *Commissioning of the ATLAS high-performance b-tagging algorithms in the 7 TeV collision data*, Tech. Rep. ATLAS-CONF-2011-102, CERN, Geneva, Jul, 2011.

[117] The ATLAS Collaboration, *Search for supersymmetry in final states with jets, missing transverse momentum and one isolated lepton in $\sqrt{s} = 7$ TeV pp collisions using 1 fb^{-1} of ATLAS data*, Phys.Rev. **D85** (2012) 012006, arXiv:1109.6606 [hep-ex].

[118] The ATLAS Collaboration, *Determination of the muon reconstruction efficiency in ATLAS at the Z resonance in proton-proton collisons at* $\sqrt{s} = 7\ TeV$, . ATLAS-CONF-2011-008.

[119] The ATLAS Collaboration, *Reconstruction and Calibration of Missing Transverse Energy and Performance in Z and W events in ATLAS Proton-Proton Collisions at* $\sqrt{s} = 7\ TeV$, . ATLAS-CONF-2012-101.

[120] The ATLAS Collaboration, *Performance of Missing Transverse Momentum Reconstruction in Proton-Proton Collisions at 7 TeV with ATLAS*, Eur.Phys.J. **C72** (2012) 1844, arXiv:1108.5602 [hep-ex].

[121] F. Krauss, R. Kuhn, and G. Soff, *AMEGIC++ 1.0: A Matrix element generator in C++*, JHEP **0202** (2002) 044, arXiv:hep-ph/0109036 [hep-ph].

T. Gleisberg and S. Hoeche, *Comix, a new matrix element generator*, JHEP **12** (2008) 039, arXiv:0808.3674.

[122] H.-L. Lai, M. Guzzi, J. Huston, Z. Li, P. M. Nadolsky, et al., *New parton distributions for collider physics*, Phys.Rev. **D82** (2010) 074024, arXiv:1007.2241 [hep-ph].

[123] M. Aliev, H. Lacker, U. Langenfeld, S. Moch, P. Uwer, et al., *HATHOR: HAdronic Top and Heavy quarks crOss section calculatoR*, Comput. Phys. Commun. **182** (2011) 1034–1046, arXiv:1007.1327 [hep-ph].

K. Melnikov and F. Petriello, *Electroweak gauge boson production at hadron colliders through* $\mathcal{O}(\alpha_s^2)$, Phys. Rev. **D74** (2006) 114017, arXiv:hep-ph/0609070.

[124] S. Frixione, F. Stoeckli, P. Torrielli, B. R. Webber, and C. D. White, *The MCaNLO 4.0 Event Generator*, arXiv:1010.0819 [hep-ph].

[125] G. Corcella, I. Knowles, G. Marchesini, S. Moretti, K. Odagiri, et al., *HERWIG 6: An Event generator for hadron emission reactions with interfering gluons (including supersymmetric processes)*, JHEP **0101** (2001) 010, arXiv:hep-ph/0011363 [hep-ph].

G. Corcella, I. Knowles, G. Marchesini, S. Moretti, K. Odagiri, et al., *HERWIG 6.5 release note*, arXiv:hep-ph/0210213 [hep-ph].

[126] The ATLAS, *New ATLAS event generator tunes to 2010 data*, Tech. Rep. ATL-PHYS-PUB-2011-008, CERN, Geneva, Apr, 2011.

[127] J. Butterworth, J. R. Forshaw, and M. Seymour, *Multiparton interactions in photoproduction at HERA*, Z.Phys. **C72** (1996) 637–646, arXiv:hep-ph/9601371 [hep-ph].

[128] M. Muhlleitner, A. Djouadi, and Y. Mambrini, *SDECAY: A Fortran code for the decays of the supersymmetric particles in the MSSM*, Comput.Phys.Commun. **168** (2005) 46–70, arXiv:hep-ph/0311167 [hep-ph].

[129] W. Beenakker, R. Hopker, M. Spira, and P. M. Zerwas, *Squark and gluino production at hadron colliders*, Nucl. Phys. **B492** (1997) 51–103, arXiv:hep-ph/9610490.

[130] A. Kulesza and L. Motyka, *Threshold resummation for squark-antisquark and gluino-pair production at the LHC*, Phys.Rev.Lett. **102** (2009) 111802, arXiv:0807.2405 [hep-ph].

A. Kulesza and L. Motyka, *Soft gluon resummation for the production of gluino-gluino and squark-antisquark pairs at the LHC*, Phys.Rev. **D80** (2009) 095004, arXiv:0905.4749 [hep-ph].

W. Beenakker, S. Brensing, M. Kramer, A. Kulesza, E. Laenen, et al., *Soft-gluon resummation for squark and gluino hadroproduction*, JHEP **0912** (2009) 041, arXiv:0909.4418 [hep-ph].

W. Beenakker, S. Brensing, M. Kramer, A. Kulesza, E. Laenen, et al., *Squark and gluino hadroproduction*, Int.J.Mod.Phys. **A26** (2011) 2637–2664, arXiv:1105.1110 [hep-ph].

[131] P. M. Nadolsky et al., *Implications of CTEQ global analysis for collider observables*, Phys. Rev. **D78** (2008) 013004, arXiv:0802.0007.

[132] A. Martin, W. Stirling, R. Thorne, and G. Watt, *Parton distributions for the LHC*, Eur.Phys.J. **C63** (2009) 189–285, arXiv:0901.0002 [hep-ph].

[133] M. Botje, J. Butterworth, A. Cooper-Sarkar, A. de Roeck, J. Feltesse, et al., *The PDF4LHC Working Group Interim Recommendations*, arXiv:1101.0538 [hep-ph].

[134] The ATLAS Collaboration, *Selection of jets produced in proton-proton collisions with the ATLAS detector using 2011 data*, . ATLAS-CONF-2012-020.

[135] A. Read, *Presentation of search results: the CL_s technique*, Journal of Physics G: Nucl. Part. Phys. **28** (2002) 2693–2704.

[136] ATLAS Collaboration, G. Aad et al., *Search for top and bottom squarks from gluino pair production in final states with missing transverse energy and at least three b-jets with the ATLAS detector*, Eur.Phys.J. **C72** (2012) 2174, arXiv:1207.4686 [hep-ex].

[137] M. W. Cahill-Rowley, J. L. Hewett, A. Ismail, and T. G. Rizzo, *More Energy, More Searches, but the pMSSM Lives On*, arXiv:1211.1981 [hep-ph].